Title
Implementation of ion exchange processes on industrial waste streams for carbon dioxide mineralization

Author
Bustillos, Steven Juan

Publication Date
2023

Peer reviewed|Thesis/dissertation

UNIVERSITY OF CALIFORNIA

Los Angeles

Implementation of ion exchange processes on industrial waste streams for carbon dioxide mineralization

A dissertation submitted in partial satisfaction of the requirements for the degree

Doctor of Philosophy in Chemical Engineering

by

Steven Juan Bustillos

2023

ABSTRACT OF THE DISSERTATION

Implementation of ion exchange processes on industrial waste streams for CO_2 mineralization

by

Steven Juan Bustillos

Doctor of Philosophy in Chemical Engineering

University of California, Los Angeles, 2023

Professor Dante A. Simonetti, Chair

Sequestration of CO_2 within stable mineral carbonates (e.g., $CaCO_3$) represents an attractive emission reduction strategy as it offers a leakage-free alternative to geological storage of CO_2 in an environmentally benign form. However, the pH of aqueous streams equilibrated with gaseous streams containing CO_2 (pH < 4) are typically lower than that which is required for carbonate precipitation (pH > 8). Traditionally, alkalinity is provided by a stoichiometric reagent (e.g., NaOH) which renders these processes environmentally hazardous and economically unfeasible. This work investigates the use of regenerable ion-exchange materials to induce alkalinity in CO_2-saturated aqueous solutions such that the pH shift required for mineralization occurs without the need for stoichiometric reagents. Na^+-H^+ exchange isotherms (at $[H^+] = 10^{-8}$-10^{-1} M) and rates were measured for 13X and 4A zeolites and TP-207 and TP-260 organic exchange resins in batch equilibrium and fixed-bed exchange experiments, respectively. At solutions equilibrated with CO_2 at 1.0 atm (pH = 3.9), H^+ exchange capacities for the materials were similar (1.7-2.4 mmol H^+/g

material) and resulted in pH increases from 3.9 to greater than 8.0. Multi-component mixtures using Ca^{2+} and Mg^{2+} cations (at 10^{-3}-10^{-1} M) in CO_2-saturated water were used to probe competitive ion exchange. The presence of divalent cations in solution inhibited H^+ exchange, reducing capacities to as low as 0.2 mmol H^+/g for both resins and zeolites. Dynamic H^+ exchange capacities in fixed-bed ion exchange columns were similar-to equilibrium values for resins (~1.5 mmol/g) and zeolites (~0.8 mmol/g) using inlet solutions that were equilibrated with gaseous streams of CO_2 at 1.0 atm. For the four ion exchange materials studied (e.g., ion exchange resins and synthetic zeolites), quasi-chemical linear driving-force approximations that are in first order in solid-phase capacity, effectively model contaminant breakthrough curves. Experimentally determined rate parameters reflect those determined from pore diffusion with pellets: 0.091 s^{-1} for R-1, 0.06 s^{-1} for R-2, 0.04 s^{-1} for Z-1, and 0.025 s^{-1} for Z-2, particles larger than 500 µm. Predictive H^+ titration capacities for these ion exchange materials were within 5% difference of experimentally determined H^+ titration capacities: 0.81 mmol H^+ g^{-1} of R-1, 0.68 mmol H^+ g^{-1} of R-2, 0.26 mmol H^+ g^{-1} of Z-1, and 0.18 mmol H^+ g^{-1} of Z-2 for pCO_2 = 0.12 atm equilibrated inlet streams. These studies demonstrate that linear driving-force approximations can model experimentally determined H^+ removal parameters. Additionally, experimental calcite precipitation from mixing the alkaline CO_3^{2-}-rich water solution obtained from the ion-exchange column with a synthetic liquid waste stream solution achieved thermodynamic maximum yields.

Geochemical and process modeling software was used to identify thermodynamically optimum conditions and to quantify the energy intensity and CO_2 reduction potential of a process that sequesters CO_2 (dissolved in wastewater) as solid calcium carbonate ($CaCO_3$). $CaCO_3$ yields are maximized when initial calcium to CO_2 ratios in the aqueous phase are 1:1. The energy intensity

for the ion exchange process (0.22 – 2.10 Megawatt-hour per tonne of CO_2 removed (MWh/t-CO_2)) is dependent upon the concentration of CO_2 in the gas phase (i.e., 5-50 vol%) and the produced water composition, with nanofiltration and reverse osmosis steps used to recover magnesium and sodium ions contributing the largest energy requirements (0.07 – 0.80 MWh per t-CO_2 removed). Energy consumption was minimized under conditions where $CaCO_3$ yields were maximized for all produced water compositions and CO_2 concentrations. The ratio of net CO_2 to gross CO_2 removal for the process ranged from 0.05 to 0.90, indicating a net CO_2 reduction across all conditions studied.

Furthermore, this ion exchange process was scaled up to treat 300 L of produced water brine (oil- and gas-associated wastewater) per day for CO_2 mineralization. Produced water brines are optimal for this process because these brines are (Mg^{2+}, Ca^{2+})-rich, suitable for CO_2 mineralization, and Na^+-rich, optimal for regeneration of the spent ion exchange solids used to induce a pH swing. Proton titration capacities were quantified for aqueous streams in equilibrium with gas streams at various concentrations of CO_2 (pCO_2 = 0.03 – 0.20 atm; 0.10 – 0.81 mmol H^+ per g ion exchange solid) and at various flow rates (0.5 – 2.0 L min^{-1}; in equilibrium with 0.12 atm gas phase CO_2; 0.65 mmol H^+ per g ion exchange solid). Utilizing inlet CO_2 concentration at 0.12 atm, 0.5 – 3.5 g $CaCO_3$ per L produced water was precipitated, resulting in energy intensities between 30 – 65 kWh per tonne of CO_2 sequestered from pumping and effluent mixing. The energy intensity of the process was dependent on volume ratios of the higher alkaline, ion-exchanged CO_2 stream and alkaline cation-rich produced water used to precipitate $CaCO_3$. Thermodynamic simulations for precipitated $CaCO_3$ formation were validated through this system, with calcite as the primary precipitated $CaCO_3$ phase (>97%) and 3% FeO solids from produced water. A life cycle

assessment was performed to analyze the net carbon emissions of the technology for two produced water compositions in equilibrium with gas streams at various CO_2 partial pressures (pCO_2 = 0.03 – 0.20 atm) which indicated a net CO_2 reduction for $pCO_2 \geq 0.12$ atm (-0.06 to -0.39 kg CO_2e per kg precipitated $CaCO_3$) utilizing calcium-rich brines. The results from this study indicate the ion exchange process can be used to provide alkalinity for the precipitation of carbonate solids for most of the CO_2 concentrations, thereby opening a pathway toward sustainable and economic mineralization processes.

The dissertation of Steven Juan Bustillos is approved.

Panagiotis D. Christofides

Philippe Sautet

Gaurav Sant

Dante A. Simonetti, Committee Chair

University of California, Los Angeles

2023

TABLE OF CONTENTS

LIST OF FIGURES

LIST OF TABLES

ACKNOWLEDGEMENTS

I would like to express my deepest gratitude to my family for their immense support and encouragement throughout my entire academic journey. My parents' love and belief in my abilities gave me great motivation to succeed in achieving my higher academic achievements and made me the person I am today. I am immensely thankful to my brother for his invaluable academic guidance stemming back from my high school days. Their continuous support greatly helped me through my Ph.D. journey and would not have been possible without them.

A special thanks to my advisors, Professor Simonetti and Professor Sant, for their guidance, wisdom, and continuous support on all projects I worked on. Both of your expertise and insights were invaluable in shaping the direction of my Ph.D. research, which all helped me grow into a better researcher and logical thinker. I would additionally like to thank my committee members, Professor Sautet and Professor Christofides, for taking the time to provide constructive feedback on my work.

I am extremely grateful for all the lab mates I have met and worked with during my Ph.D. journey, from both Simonetti and Sant lab groups. I have met many great researchers during my time here, my deepest apologies if I forget to mention you here. I would like to thank former Simonetti group member graduates: Luke, Sara, Aziz, Anas, Eric, and Byron – you all made my transition into UCLA my first year very enjoyable and provided great intellectual knowledge throughout my time here. I would like to give big thanks to Marios for contributing immensely to portions of this work that led to its publication. A big thank you to Tom for all of the insightful lunches we had at the tail-end of my Ph.D. journey. I would like to thank former Sant group member graduates: Sara, Sharon, Shiqi, Tandre, Gabe and Jason – you all gave me great advice to succeed at the beginning

of my Ph.D. journey and were always willing to help when I had questions. Another big thank you to all the post-doctoral scholars and project scientists I got to work with: Erika, Dale, Arnaud, Marie, Ross and Xin – you all provided great constructive feedback in our weekly group meetings that helped me grow and become the researcher I am today. I would also like to thank my lab mates Jenny, Adriano, and Swarali for making lab life much more fun and always willing to collaborate. I would like to thank all of my collaborators that contributed immensely during my Ph.D. journey: Stephanie for your great help in my first publication here at UCLA, Professor Bu Wang of the University of Washington for providing valuable insight to my research work, and former UCLA students Mark, Mitchell, and Jack for helping and contributing to the success of this research work.

My final thanks are to Professor McFarland at UC Santa Barbara and Professor Nilsson at UC Irvine: you both provided me with the necessary training and early mentorship I needed to succeed as an undergraduate researcher. Those valuable experiences helped me grow as a researcher and helped me progress early on during my Ph.D. journey.

VITA

2013 – 2016	Associates of Arts in Science, Technology, Engineering & Math Los Angeles Pierce College Woodland Hills, California
2016 – 2018	Bachelor of Science in Chemistry University of California, Santa Barbara Santa Barbara, California
2018 – 2023	Graduate Student Researcher Department of Civil Engineering University of California, Los Angeles
2020 – 2023	Teaching Assistant Department of Civil Engineering University of California, Los Angeles
2022	Alicat Scientific University Grant Program Award Winner

CONFERENCE PRESENTATIONS

1. Bustillos, S., Ragipani R., Prentice, D., Wang, B., Sant, G., Simonetti, D., *Process Optimization of Ion Exchange Processes for CO_2 Mineralization Utilizing Industrial Waste Streams*. American Institute of Chemical Engineers Annual Meeting. 2021. Novel Approaches to CO_2 Utilization I.

2. Bustillos, S., Alturki, A., Prentice, D., La Plante, E. C., Sant G., Simonetti, D. *Implementation of Ion Exchange Processes for CO_2 Mineralization Using Produced Water Streams*. American Institute of Chemical Engineers Annual Meeting. 2020. Novel Approaches to CO_2 Utilization I.

PUBLICATIONS

1. S. J. Bustillos, M. Christofides, B. McDevitt, M. Blondes, R. McAleer, A. Jubb, B. Wang, G. Sant, D. Simonetti. “Pilot plant demonstration and life cycle assessment of ion exchange processes for CO_2 mineralization using industrial waste streams.” *ChemPlusChem*, **2023**, Review pending.

2. G. Sant, X. Chen, D. Simonetti, D. Jassby, E. C. La Plante, S. J. Bustillos, T. Traynor, A. Bouissonnie. **2023**. “Oxygen-Selective Anodes.” **63/442,298**. filed January 31, 2023. Patent pending.

3. G. Sant, D. Simonetti, X. Chen, D. Jassby, E. C. La Plante, S. J. Bustillos, T. Traynor, A. Bouissonnie. **2023**. "Aqueous electrochemical processes for carbon immobilization and sequestration." **63/442,292**. filed January 31, 2023. Patent pending.

4. G. Sant, X. Chen, D. Simonetti, D. Jassby, E. C. La Plante, S. J. Bustillos, T. Traynor, A. Bouissonnie. **2023**. "Mitigating chloride ion oxidation during saline water electrolysis for hydrogen production and carbon dioxide mineralization." **63/442,295**. filed January 31, 2023. Patent pending.

5. G. Sant, X. Chen, D. Simonetti, S. J. Bustillos, D. Jassby. **2022**. "Co-deacidification and dichlorination of aqueous/gaseous streams by mineral dissolution." **63/427,027**. filed November 21, 2022. Patent pending.

6. E. C. La Plante, X. Chen, S. J. Bustillos, A. Bouissonnie, T. Traynor, D. Jassby, L. Corsini, D. Simonetti, G. Sant. "Electrolytic seawater mineralization and how it ensures (net) carbon dioxide removal." *ACS Environmental Science & Technology*, **2023**

7. S. J. Bustillos, D. Prentice, E. C. La Plante, B. Wang, G. Sant, D. Simonetti. "Process Simulations Reveal the Carbon Dioxide Removal Potential of a Process that Mineralizes Industrial Waste Streams via an Ion Exchange-Based Regenerable pH Swing." *ACS Sustainable Chemical Engineering*, **2022**, 10, 19.

8. S. Dong, R. Arnold, K. Yang, E. C. La Plante, S. J. Bustillos, A. Kumar, B. Wang, M. Balonis, N. Neithalath, K. Ellison, M. Bauchy, D. Simonetti, G. Sant. "Rapid Elemental Extraction from Ordered and Disordered Solutes by Acoustically-Stimulated Dissolution." *ACS Engineering Au*, **2021**, 1, 2.

9. S. J. Bustillos, A. Alturki, D. Prentice, E. C. La Plante, M. Rogers, M. Keller, R. Ragipani, B. Wang, G. Sant, D. Simonetti. "Implementation of Ion Exchange Processes for Carbon Dioxide Mineralization Using Industrial Waste Streams." *Frontiers in Energy Research*, **2020**, 8, 1-17

10. S. Aguilar, S. J. Bustillos, S. Xue, W. H. Mak, C. Ji, E. Rao, B. T. McVerry, E. C. La Plante, D. Simonetti, G. Sant, R. Kaner. "Enhancing Polyvalent Cation Rejection Using Perflourophenylazide-Grafted-Copolymer Membrane Coatins." *ACS Applied Materials & Interfaces*, **2020**, 12, 37, 42030-42040

Chapter 1 Introduction and background

1.1. Motivation

1.1.1. Introduction to CO_2 capture technologies

Carbon dioxide (CO_2) is the primary greenhouse gas emitted by human activities[1]. According to the International Energy Agency, global CO_2 emissions from energy combustion and industrial processes reached a new maximum at 36.8 Gt CO_2 in 2022[2], in which approximately 50% of these emissions (18.5 Gt CO_2) have been generated during the primary energy consumption of oil and gas in the transportation and industrial sectors[3]. The United States contributed approximately 17% (6.3 Gt CO_2) to total global CO_2 emissions, where approximately 1.4 Gt CO_2 and 1.8 Gt CO_2 were from industrial and transportation sectors[4]. High oil and gas demands consequentially result in the generation of large volumes of produced water (brine co-produced during the extraction of oil and gas), approximately 24 billion barrels of produced water[5] yearly in the United States leading to increased levels of brine waste and CO_2 emissions (0.5 – 13.5 kg CO_2 equivalent per m^3 produced water processed)[6].

Post-combustion capture of CO_2 (e.g., from power plants using amine-based processes[7–9]) and storage in geological formations (CCS) is the current state-of-the-art for CO_2 emissions mitigation. Decades of process optimization[10–12] and large theoretical storage capacities in the U.S.[13–15] make amine-based CCS processes particularly effective for large point source emitters (e.g., fossil fuel fired power plants[16,17,18]). However, large energy demands (>0.36 MWh per ton CO_2 captured for streams with less than 12% CO_2[17,19]), high capital costs of large amine plants[17,20,21], and high

operating expenses (e.g., for pipeline transportation and for storage site monitoring) are barriers for the use of amine-based processes in the oil and gas sector where emissions are more dilute and/or distributed (e.g., less than 3% CO_2 in flare gases from refineries, petrochemical plants, and natural gas wells[22–24]). Thus, the low carbon future envisioned to combat climate change will require new technologies for CO_2 emissions mitigation from primary energy users and during oil and gas recovery.

Sequestration of CO_2 as a solid carbonate (i.e., mineralization) is an alternative emission mitigation strategy opposed to post-combustion capture of CO_2. CO_2 is captured as a stable carbonate solid (usually in the form of calcium or magnesium carbonates) via chemical reaction with Ca/Mg ions in alkaline aqueous solutions.[25,26] Mineralization-based CO_2 capture and storage involve inherently lower energy processes because the CO_2 capture and storage occur without requiring a separate removal/concentration step (i.e., absorption from a vapor phase). These processes also exploit the favorable thermodynamics of carbonate precipitation reactions (ΔG = -1129.1 kJ/mol for calcite precipitation). By avoiding the CO_2 capture steps, mineralization-based approaches can be applied across a wide range of CO_2 concentrations (i.e., atmospheric concentrations to 100 vol. % CO_2) and temperatures (i.e., ambient to ~90°C) without increasing energy requirements (i.e., associated with large heat duties for thermal swing amine-based processes[15]). These processes are also insensitive to the impurities in CO_2-containing streams (e.g., hydrocarbons and H_2S). Thus, mineralization approaches represent an attractive alternative to CCS for CO_2 emission mitigation in the oil and gas sector because reduced process complexity and broad operating conditions enable modularity with few unit operations (i.e., process intensification) and flexibility in fulfilling carbon management goals across diverse locations and settings without the need for transport infrastructure (e.g., pipelines, compression stations, etc.).

CO_2 mineralization (e.g., as calcium carbonate) occurs via the following reaction:

$$Ca^{2+}(aq) + CO_3^{2-}(aq) \rightarrow CaCO_3(s) \quad (1)$$

The speciation reactions that describe the CO_2–H_2O system are written as:

$$CO_2(g) + H_2O \rightleftharpoons CO_2(aq) + H_2O \rightleftharpoons H_2CO_3(aq) \quad (2)$$

$$H_2CO_3(aq) \rightleftharpoons H^+(aq) + HCO_3^-(aq) \quad (3)$$

$$HCO_3^-(aq) \rightleftharpoons H^+(aq) + CO_3^{2-}(aq) \quad (4)$$

In general, the concentration of CO_3^{2-} anions (and thus, the extent of carbonate precipitation) depends on pH (e.g., in water, CO_3^{2-} is the dominant carbon species at pH > 10.33[27,28]), so the mineralization strategy described above requires sources of Ca/Mg ions and alkalinity. Approximately 22 billion barrels of liquid-waste water, known as produced water (PW), is produced during oil and gas extraction yearly.[29–32] The vast majority of PW is injected for disposal, resulting in only 0.6% of PW utilized for beneficial reuse.[29,31,32] After separation of organic components, PW is rich in primarily Na^+, Ca^{2+}, Mg^{2+} and Cl^- ions (0.050 M – 3.0 M).[33] These high cation concentrations make PW viable sources of cations for mineralization processes. However, these streams are typically produced at 4 < pH < 7 (with bicarbonate, HCO_3^-, as the predominant species)[33]. The addition of caustic soda (NaOH) to increase the pH of these streams would render mineralization processes uneconomical because of the costs and hazards of using NaOH. Previous studies have explored the use of alkaline solid wastes (i.e., combustion fly ashes and slags)[34–37], however, this still involves the use of a stoichiometric reagent whose production occurs in much lower abundance (130 million tons per year)[37,38] compared to CO_2 emissions from oil and gas processes (2.9 billion tons per year).

1.2. Scope and Organization

1.2.1. CO_2 mineralization via ion exchange processes

In this work, the use of ion exchange (IEX) processes as an alternative method to induce alkalinity for the precipitation of $CaCO_3$ using wastewater streams is investigated. Exposing CO_2-saturated solutions (pH = 3.9) to regenerable IEX materials can produce solutions with pH > 10.0, thereby creating favorable conditions for CO_2-mineralization reactions. Ion exchange occurs between an electrolyte solution and similarly charged ions immobilized in an IEX material through a stoichiometric, reversible IEX reaction. Previous research has shown the reversible exchange of H^+ and Na^+ ions in a solution using clay minerals.[39–41]

This work aims to identify commercially available IEX materials capable of shifting the pH of CO_2-saturated solutions for subsequent precipitation as carbonates. Commercially available WAC resins (TP-207, TP-260) and synthetic zeolites (Type 4A, Type 13X) were selected to quantify exchange capacities and kinetic exchange parameters. These resins and synthetic zeolites were selected because of their weakly acidic functional groups and low Si/Al ratios (1.0 for Type 4A and 1.24 for Type 13X), respectively. IEX was studied across a range of H^+ concentrations from HCl and CO_2 batch solutions to determine the effect of proton and anion concentrations on the exchange capacities of these materials. Equilibrium IEX isotherms were developed for materials and compared with competitive ions to determine the process design and configuration. IEX kinetic constants and capacities are quantified using simple linear driving force (LDF) models for dynamic IEX experiments performed by column exchange. Materials were regenerated to quantify

working capacities and kinetics. Furthermore, CO_2 mineralization was performed using simulated PW streams as the source for calcium ions[29,30,33,42] and the effluent solution compositions from the IEX columns. Geochemical modelling to rapidly estimate the propensity of formation of minerals in solution (e.g, $CaCO_3$) was performed using Gibbs Energy Minimization (GEM) software.[43,44] Furthermore, this work seeks to quantify the emissions mitigation impact of our process by using thermodynamic and process simulations to determine energy consumptions and calcium carbonate yields for various produced water and CO_2 waste streams. Herein, we demonstrate that implementing this process for CO_2 mineralization results in net negative carbon emissions for the various produced water compositions studied. Energy requirements and costs of the process significantly decrease when utilizing higher CO_2 flue gas concentrations. To better understand how this process operates using real-world brines of variable chemistries, two produced water sources from the United States are tested: the Niobrara mixed-shale and chalk play in the Denver-Julesburg Basin and the Utica-Point Pleasant mixed shale and limestone play in the Appalachian Basin. A life cycle assessment (LCA) methodology is employed to analyze the life cycle or net carbon emissions of the technology. The work presented herein demonstrates these processes by identifying suitable materials and process parameters and by presenting possible strategies for integration with various processes related to the oil and gas sector.

Chapter 2 Experimental Materials and Methods

2.1.1. Solutions preparation and solids characterization

Sodium chloride (NaCl, >99.0%), calcium chloride dihydrate ($CaCl_2 \cdot 2\ H_2O$, >99.0%), calcium sulfate dihydrate ($CaSO_4 \cdot 2\ H_2O$, >99.0%), ferric chloride hexahydrate ($FeCl_3 \cdot 6\ H_2O$, >99.0%), potassium chloride (KCl, >99.0%) and magnesium chloride hexahydrate ($MgCl_2 \cdot 6\ H_2O$, >99.0%) were all purchased from Fisher Chemicals. 70% (w/w) nitric acid (HNO_3) and 12.5% (w/w) hydrochloric acid (HCl) solutions were purchased from Sigma Aldrich. High purity carbon dioxide (CO_2, 99.99%, Airgas) cylinders were used as the source for the preparation of CO_2-saturated solutions. All chemicals were used as received unless otherwise stated. Commercially available synthetic zeolites (4A and 13X; 8–12 mesh; Fisher Chemicals) and sodium-form chelating cation exchange resins (Lewatit TP 207 (iminodiacetate functional groups) and Lewatit TP 260 (aminomethyl phosphonate functional groups); Sigma Aldrich) were used for IEX experiments. Cation exchange resins were preconditioned using 2 N HCl (Sigma Aldrich), 1 N NaOH (Sigma Aldrich), and washed with ultra-pure water (Milli-Q, resistance of 18.2 $M\Omega\ cm^{-1}$) to remove any contaminants and ensure resins are Na^+-form at saturation.[45]

Chemical analysis of ion-exchange materials (Table 1) was performed by electron dispersion spectroscopy (EDS; Nova 230 model) with a 10 kV accelerating voltage and a working distance of 5 mm.

Table 1. Chemical composition of ion exchange materials obtained by EDS (Nova 230 model with a 10 kV accelerating voltage and a working distance of 5 mm).

Sample	Material	Na (mol %)	C (mol %)	N (mol %)	O (mol %)	Si (mol %)	Al (mol %)
R-1	TP 207	12.3±1.00	63.0±1.52	2.93±0.69	21.9±1.2	N.D.	N.D.
R-2	TP 260	10.3±1.10	56.9±1.15	3.76±0.52	24.9±1.1	N.D.	N.D.
Z-1	4A	14.1±1.10	N.D.	N.D.	59.6±1.2	10.9±1.30	14.5±1.10
Z-2	13X	13.8±0.30	N.D.	N.D.	58.9±1.1	12.6±1.50	13.8±1.20

Brunauer-Emmett-Teller (BET) surface areas were calculated from N_2 adsorption-desorption isotherms, measured at 77 K with a Micrometrics ASAP 2020 Plus I system. Before measurements, samples were degassed at 1×10^{-3} Torr, and 573 K. Pore size distributions were calculated from the adsorption branches of the isotherms using the Barrett-Joyner-Halenda (BJH) model. Bulk porosities and densities were measured using helium pycnometry (AccuPyc II 1340, Micrometrics) after drying the materials at 65°C for three hours. Additionally, particle size distributions were measured using static light scattering (SLS; LS13-320, Beckman Coulter Static Light Scattering) with water and sonication being used to ensure particle dispersion. A summary of material properties is shown in Table 2.

Table 2. Textural Properties of the ion exchange materials used in this study

Sample number	**Ideal CEC[a] (mmol/g)**	**Bulk porosity[c] (%)**	**Density[c] (g/cm^3)**	**Particle size (mm)[d] d_{50}**	**Surface Area[e] (m^2/g)**	**Pore Size[f] (Å)**
Z-1	N/A	33	1.91 ± 0.01	1.60 ± 0.5	448 ±1.4	52.0 ±1.4
Z-2	N/A	39	1.85 ± 0.01	2.31 ± 0.18	244 ±1.8	128 ±1.3
R-1[b]	1.9	26	1.34 ± 0.01	0.59 ± 0.04	6.1 ±1.4	197 ±1.2
R-2[b]	1.6	31	1.45 ± 0.01	0.61± 0.05	13.9 ±1.7	284 ±1.1

[a]Manufacturer-specified cation exchange capacity (CEC), [b]Minimum H-form exchange capacity: based off industrial scale cation exchange using H-form resins, [c]Based on He-pycnometery, [d]Based on SLS method, [e]Based on BET, [f]Based on BJH method

2.2. Experimental design for CO_2 mineralization via ion exchange processes

2.2.1. Batch equilibrium ion- exchange experiments

Single component IEX experiments using HCl and CO_2-saturated solutions (pCO_2 = 1.0 atm, pH = 3.9) were performed to determine Na^+-H^+ exchange isotherms. Aqueous solutions with 0.001,

0.010, 0.1, 0.25 and 0.5 M of HCl were prepared by diluting 12.5% (w/w) HCl with ultra-pure water (18.2 MΩ cm^{-1}). CO_2-saturated solutions were prepared by bubbling CO_2 into ultra-pure water at 25°C, where $[CO_2]$ = 0.0334 M according to Henry's law (K_H = 30 L atm mol^{-1}), resulting in a saturation pH of 3.9.[46] CO_2 was bubbled until a stable pH of 3.9 was read using a pH electrode (Thermo Scientific Orion Versa Star). All experiments were performed using a solid/liquid ratio of 0.003 g/mL and at 25°C unless otherwise stated. All batch equilibrium experiments were performed using tightly sealed conical centrifuge tubes of equal dimensions and shaken continuously using a Corning LSE orbital shaker for four days. Solutions from all batch equilibrium experiments were sampled at 5, 10, 30, 60, 100, 180 and 240 minutes, and every 24 hours afterward for cation concentration analysis by inductively coupled plasma – optical emission spectroscopy (ICP-OES; Avio 200 ICP Optical Emission Spectrometer, Perkin Elmer) to ensure equilibrium was achieved. Samples were filtered through a 0.2-micron Corning filter and diluted in 5% (w/w) HNO_3 (prepared by diluting 70% HNO_3 in ultra-pure water).

Equilibrium was established when cation concentrations in solution were invariant with time. Equilibrium exchange capacities (EC; mmol/g) were calculated by

$$EC = \frac{(C_0 - C_f) \cdot V}{W} \qquad (6)$$

where C_f and C_o are final and initial cation concentrations in solution, respectively, V is the solution volume, and W is the mass of solid.

Competitive IEX was performed using solutions containing CO_2-$CaCl_2$ compositions. Saturated CO_2 in solution (pCO_2 = 1.0 atm) was fixed while $CaCl_2$ concentrations were varied from 0.001 to 1 M.

2.2.2. Fixed-bed ion exchange experiments

An IEX column apparatus was constructed to study the dynamic ion exchange performance for the IEX materials. A schematic of the apparatus is shown in Figure 1. Liquid feed was introduced into a glass tube (3.5 cm inner diameter) using a BioLogic LP peristaltic pump. Fixed beds of IEX material (performed using bed volumes of 134.7 cm^3 [14 cm height] unless otherwise stated) were held in place using quartz wool.

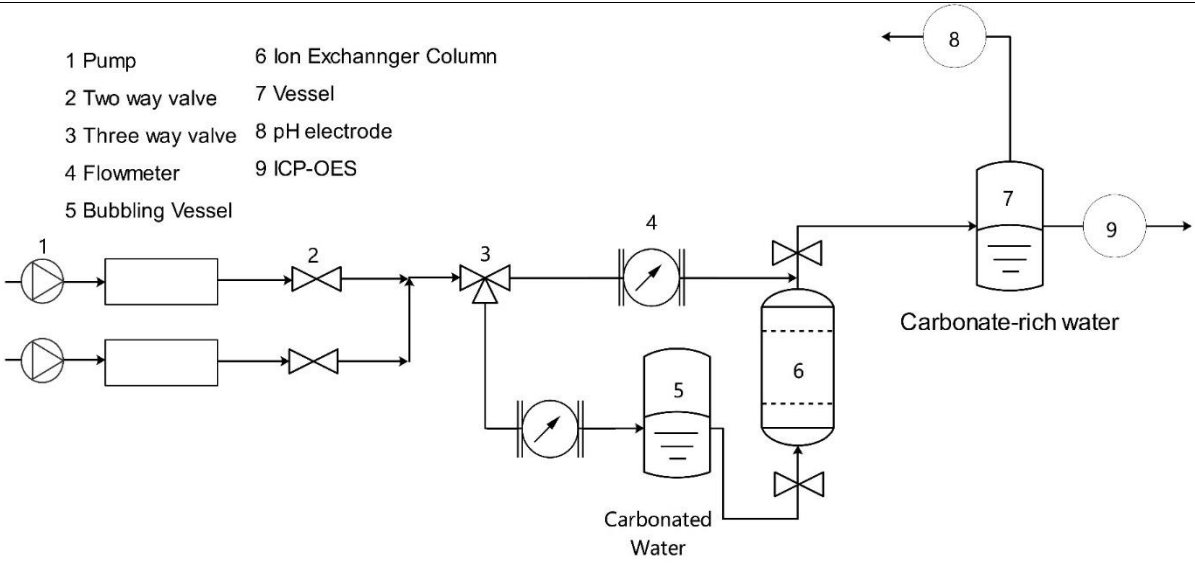

Figure 1. Experimental schematic of the ion-exchange column used in this study.

The effect of inlet CO_2 concentrations on the H^+ exchange was performed using TP-207 (134.7 cm^3; 14 cm height; 40 ccm) at the following CO_2 inlet concentrations: 1.0 atm/pH 3.9, 0.5 atm/pH 4.1, 0.25 atm/pH 4.2 and 0.1.0 atm/pH 4.4 until the effluent pH (or cation concentration) was equivalent to that of the inlet. Effluent samples were collected at intervals of 5 minutes during the

first hour and 30 minutes thereafter. Collected effluent samples were analyzed using a pH meter and ICP-OES. The breakthrough curves developed are presented as the normalized effluent H^+ concentration (eq. 7) as a function of the number of normalized bed volumes (NBV) processed (eq. 8). NBV is defined as liquid flowrate, Q (mL/min) divided by IEX material bed volume (BV; cm^3) multiplied by time, t (min).

$$\text{Normalized Effluent Concentration} = \frac{C_{effluent}}{C_{inlet}} \qquad (7)$$

$$NBV = \frac{Q \cdot t}{BV} \qquad (8)$$

Fixed-bed IEX regeneration experiments (12.4 cm^3; 1.5 cm inner diameter and 7 cm bed length; 40 ccm) were performed using an inlet CO_2-saturated solution (pCO_2 = 1.0 atm, pH 3.9) to exhaust the column to the saturation limit and subsequently regenerated using an inlet solution composed of 0.7 M NaCl at pH 9.9 (representative of the solution composition following mineralization in this process). Three cycles were performed for each IEX material used in this study.

2.2.3. Analytical models for dynamic ion exchange experiments

Mathematical models that relate the properties of the material and the experimental conditions to the concentration-time profiles in the effluent of a fixed bed (i.e., a breakthrough curve) were used to quantify the rate and maximum exchange capacity from dynamic IEX experiments. Combining the partial differential equation that arises from the mass balance on the cation in a fixed bed with an ordinary differential equation that represents a linear exchange rate leads to a simple, two parameter equation (the exchange rate parameter (kK) and the maximum exchange capacity (q_s))

that describes the breakthrough curve. These parameters can be regressed from breakthrough curve data using nonlinear least squares fitting.[47]

The rate parameter (*kK*) reflects resistance to exchange at three length scales: (1) diffusion of cations in the bulk liquid phase to the solid surface, (2) diffusion within solid phase pores, and (3) ion exchange at the anionic site. Diffusion resistances can be determined from known engineering correlations (see SI[1,2]), and these resistances can be summed in series (similar to electrical resistances) according to Equation (10)[48]:

$$\frac{1}{kK} = \frac{R_p}{3k_f} + \frac{R_p^2}{15\varepsilon_p D_p} + \frac{1}{k_{ex}} \quad (10)$$

where R_p is the radius of the ion exchanger particles, D_p is the effective diffusivity of the incoming cation inside the pores of the solids, k_f is the mass transfer coefficient for fluid film mass, k_{ex} rate of exchange at the anionic site, and ε_p is the porosity of the solid particles. The distribution parameter (*K*) is the ratio of the concentration of the cation in the solid phase to that in the fluid phase at equilibrium.

2.2.4. CO_2 mineralization using simulated produced water and ion exchange solutions

CO_2 mineralization experiments were performed using the effluents collected from dynamic IEX experiments described in *Section 2.2.2.2*. Simulated produced water samples (see Table 3 for compositions) were mixed with IEX effluents at varying volume ratios within a 1 L beaker, and solid precipitates were collected after 6 hours. Volume ratios, V_R, are defined as:

$$V_R = {V_{PW}}/{(V_{PW} + V_{IEX})} \quad (11)$$

where V_{IEX} represents the volume of IEX solution of the effluent stream from the IEX column and V_{PW} represents the volume of simulated PW.

Table 3. Simulated produced water composition from the United States Geological Survey database[46]

Salt concentration [mol/L]					
$CaCl_2$	**CaSO4**	**$FeCl_2$**	**KCl**	**$MgCl_2$**	**NaCl**
0.10	0.01	0.00044	0.0001	0.056	1.48

The IEX effluent and produced water solutions were continuously stirred for 4 hours to ensure the CO_2 mineralization reaction had occurred. After precipitation, two separate samples of the supernatant were analyzed via ICP-OES and pH measurements. Both samples were filtered through a 0.2-micron Corning filter and the ICP-OES sample was diluted in 5% (w/w) HNO_3 (prepared by diluting 70% HNO_3 in ultra-pure water). The solid was collected from the solution via vacuum filtration and dried at 60°C for 24 hours prior to analysis. Powder X-ray diffraction (XRD) patterns of the precipitated phases were obtained on an X-Ray diffractometer (Panalytical X'Pert Pro X-ray Powder Diffractometer) using Cu Kα radiation of 1.5410 Å to identify the phases in the precipitated solids. Scanning electron microscopy (SEM; Nova 230; 5 kV accelerating voltage and a working distance of 5 mm) and EDS was used to quantify elemental composition at the surface of the solids.

2.2.5. Thermodynamic Modeling of precipitated products

he activities and speciation of aqueous components were calculated using GEMSelektor, version 3.4, which includes a native GEM (Gibbs energy minimization) solver,[43,44] a built-in NAGRA-PSI 'Kernel', and the slop98.dat and Cemdata18 thermodynamic databases.[49–52] Thermodynamic data for nesquehonite ($MgCO_3.3H_2O$),[53] hydromagnesite ($Mg_5(CO_3)_4(OH)_2{\cdot}4H_2O$) [54], dolomite ($(Ca_{0.5}Mg_{0.5})CO_3$),[54] monohydrocalcite ($CaCO_3.H_2O$),[53] and an iron-calcium carbonate solid-solution model ($(Ca,Fe)CO_3$)[55] were included in the simulations. Thermodynamic data for metastable nesquehonite and hydromagnesite were included as potential magnesium carbonate phases, opposed to 'natural' mineral thermodynamic data to represent the short-term precipitation time. The dolomite phase was chosen to represent partial calcium replacement by magnesium within $CaCO_3$. The $(Ca,Fe)CO_3$ non-ideal solution model was developed in a CaO-MgO-FeOOH-CO_2 system to represent iron (II) replacement within the $CaCO_3$ structure in the presence of magnesium.[55]

The activity of any relevant ion species is described within GEMS using the Truesdell-Jones modification of the extended Debye-Hückel equation that is applicable for ionic strengths (I, mol/L) less than 2 mol/L (see Equation 12)[56]:

$$\log \gamma_i = \frac{-Az_i^2\sqrt{I}}{1 + \dot{a}B\sqrt{I}} + b_\gamma I + \log \frac{X_{jw}}{X_w} \qquad (12)$$

where, γ_i and z_i are the activity coefficient and charge of the i^{th} aqueous species respectively, A and B are temperature- and pressure-dependent coefficients, I is the molar ionic strength, X_{jw} is the molar quantity of water, and X_w is the total molar amount of the aqueous phase. A common ion size parameter, $\dot{a}$ (3.72 Å) and short-range interaction parameter, b_γ (0.064 kg·mol^{-1}), are used

as constants for the NaCl background electrolyte.[56] NaCl was selected as the dominant electrolyte throughout this study to simulate the IEX product solution compositions and pH shown in Table 3 because of constantly larger NaCl concentration in solution. Solution compositions in the simulations used the V_R ratios as described by Equation 11 using the solutions shown in Table 3.

2.3. Linear driving force approximations as predictive models for fixed-bed ion exchange reactors for CO_2mineralization

2.3.1. Fixed-bed ion exchange experiments for kinetic modeling of ion exchange rate parameters

High-purity carbon dioxide (CO_2, 99.99%, Airgas) and high purity nitrogen (N_2, 99.99%, Airgas) were used as a source for the preparation of solutions equilibrated at various partial pressures of CO_2. An ion exchange column apparatus was constructed to study the dynamic ion exchange performance for the ion exchange materials (schematic of the apparatus is shown in Figure 3). Liquid feed was introduced using a NE-9000 peristaltic dispensing pump, Fixed beds of ion exchange material were performed at bed volumes 134 – 604 cm^3 by varying bed inner diameters and bed heights to maintain a liquid residence time of 10 minutes. Ion exchange solids were held in place using quartz wool. Deionized water (temperature at 20°C) is bubbled using a gas mixture of N_2 and CO_2 (10 to 50 SLPM) to create an aqueous stream equilibrated with CO_2 at a partial pressure of 0.12 atm (pH 4.36 or $[CO_2]$ = 0.0042 M in accordance with Henry's Law; K_H = 30 L atm mol^{-1}). Equilibrium at the desired CO_2 concentration was determined when a stable pH

measurement was achieved at the expected pH with respect to Henry's Law. Flow-rate studies using an inlet CO_2-saturated solutions (pCO_2 = 0.12 atm; pH 4.36) were performed at 20, 40, and 60 cm^3 min^{-1} until the effluent pH (or cation concentration) was equivalent to that of the inlet. The breakthrough curves developed are presented as the normalized effluent H^+ concentration (Equation 7) as a function of the number of normalized bed volumes (NBV) processed (Equation 8). The fixed-bed H^+ exchange capacities (CEC_H) are quantified using the following equation:

$$CEC_H = \frac{[H]_{in} - [H]_{out}}{m} \quad (13)$$

Where $[H]_{in}$ is the total moles of H^+ fed into the reactor and $[H]_{out}$ is the total moles of H^+ out of the reactor, divided by the mass of ion exchange solid used (m). Simple linear driving force approximation models are applied to these breakthrough curves to quantify ion exchange rate parameters as discussed in *Section 2.2.3*.

2.4. Process Simulations for CO_2 mineralization via ion exchange processes

2.4.1. Thermodynamic simulations to identify conditions that maximize $CaCO_3$ yields

Produced water compositions for different regions in the United States were identified using the USGS database.[33,57] Statistical analyses were performed to quantify the mean concentrations of produced waters found in four different locations spanning the United States: Mid-continental rift, Pacific Coast, Appalachian region, and the Gulf Coast. Concentrations for each element ranged from 5.0 – 330 mmol/L Ca, 0.1 – 170 mmol/L Mg, 100 – 2600 mmol/L Na, 0.01 – 4.0 mmol/L Fe,

0.1 – 80 mmol/L K, and 0.1 – 30 mmol/L SO_4. Additionally, the pH of the mean compositions ranges from pH 6.0 – 6.8 calculated from the charge balance of the given compositions, representative of the typical pH found in produced water streams. Mean compositions of produced water found in those regions and used for thermodynamic and process simulations are shown in Table 4.

Table 4. Produced water compositions from United States Geological Survey (USGS) database.

Geological Location	**Composition I.D.**	**$CaCl_2$ (mM)**	**$MgCl_2$ (mM)**	**NaCl (mM)**	**$FeCl_2$ (mM)**	**KCl (mM)**	**$CaSO_4$ (mM)**	**pH**
Mid-continental	A	141	24.9	1206	0.63	6.5	0.81	6.2
Pacific Coast	B	70.3	20.0	1544	1.1	7.5	8.11	6.0
Appalachians	C	166	17.0	1069	0.22	8.2	1.0	6.4
Gulf Coast	D	148	23.0	1077	0.11	1.1	0.23	6.8

The mid-continental rift, which extends from Kansas to Michigan, is characterized by high Ca, high Mg, and ionic strengths ranging from 0.1 to 1.9 mol/L. The Pacific Coast, which extends from Washington to California, is characterized by low Ca, high Na, high Fe, and ionic strengths ranging from 0.1 to 2.2 mol/L. The Appalachians, which extends from Alabama to Maine, is characterized by high Ca, low Fe and ionic strengths ranging from 0.3 to 2.4 mol/L. The Gulf Coast, which extends from Texas to Florida, is characterized by high Ca, low Fe and ionic strengths ranging from 0.4 to 2.1 mol/L.

2.4.2. Aspen Plus® Process Modeling

Aspen Plus® was used as the main simulator to provide necessary chemical units from its library. eRNTL was selected as the thermodynamic property method.[58] The property method explicitly accounts for the solution chemistry, and considers dissociations of H_2O, NaOH, $CaCl_2$, $MgCl_2$, $FeCl_2$, KCl and speciation of CO_2 in water. The following APV732 property databanks were used: ASPENPCD, AQUEOUS, SOLIDS, INRGANIC, and PURGE26. Process model design to produce $CaCO_3$ via CO_2 mineralization through ion exchange processes is shown in Figure 2.

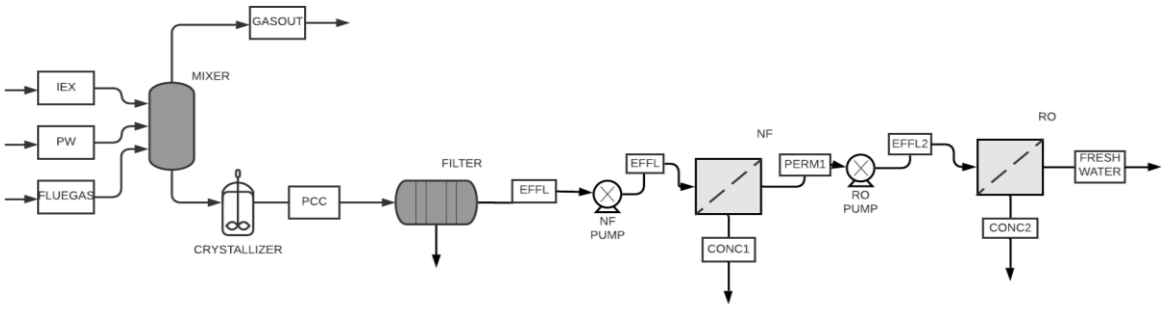

Figure 2. ASPEN Plus process flow diagram for CO_2 mineralization via ion exchange processes. CO_2-rich flue gas is fed into contact with streams of alkaline ion exchange solution (IEX) and calcium-rich produced water (PW) compositions. The stream is fed through a crystallizer for mineralization. Precipitated solids are separated via crossflow filtration (filter), where the effluent stream is treated via nanofiltration (NF) and reverse osmosis (RO).

A carbon capture plant that treats 24 metric tonnes of dry pre-treated flue gas (e.g., NO_x and SO_x depleted) containing 5 – 50% (v/v) CO_2 and 50 – 95% (v/v) N_2, per day is considered. These flue gas CO_2 concentrations are representative from various industries as previously discussed. A flue gas flow rate of 1.7 metric tonne/h was chosen to ensure carbon was available to precipitate products. The CO_2-rich flue gas is fed into contact with an alkaline ion exchange stream and calcium-rich produced water stream. NaOH is used to simulate the ion exchange stream (0.003 – 0.067 mol/L). Furthermore, NaOH was used in previous CO_2 mineralization experiments to adjust the pH of CO_2-rich solutions and in previous thermodynamic calculations to simulate expected solution compositions following ion exchange.[59] An alkaline stream containing NaOH (representative of the ion exchange effluent stream compositions) and a produced water stream using compositions according to Table 2 were used for CO_2 mineralization. Inlet flow rates for each stream were adjusted (1 – 60 m^3/h) to match the volume ratio requirement (equation 5) quantified for maximum $CaCO_3$ precipitation from GEMS thermodynamic simulations. The precipitated solid is separated via crossflow filtration, where the remaining effluent stream is treated via nanofiltration (150 – 350 kPa) and reverse osmosis (350 – 600 kPa) for complete cation removal. These operating pressures were selected to overcome the respective osmotic pressure of each stream following mineralization. nanofiltration rejection coefficients for divalent cations and reverse osmosis rejection coefficients for monovalent cations were assumed to be 0.95[60,61] and 0.99,[62,63] respectively, as they were representative of common rejection coefficients observed in these types of filtration membranes. The energy consumptions for each step of the process and total net CO_2 emissions for the process were quantified.

2.5. Pilot plant demonstration and life cycle assessment of ion exchange processes for CO_2 mineralization using industrial waste streams

2.5.1. Materials and sample characterization

Sodium chloride (NaCl, >99.0%) and sodium hydroxide pellets (NaOH, >97.0%), were purchased from Fisher Chemicals. 70% nitric acid (HNO_3) and 12.5% hydrochloric acid (HCl) solutions were purchased from Sigma Aldrich. High-purity carbon dioxide (CO_2, 99.99%, Airgas) and high purity nitrogen (N_2, 99.99%, Airgas) were used as a source for the preparation of solutions equilibrated at various partial pressures of CO_2. All chemicals were used as received unless otherwise stated. Commercially available sodium-form chelating cation exchange resin Lewatit TP-207 (iminodiacetate functional group) was used for the fixed-bed ion exchange experiments.

Two produced water samples were collected by the U.S. Geological Survey from the Niobrara Formation (Denver-Julesburg Basin) in CO, USA and Utica-Point Pleasant Formation (Appalachian Basin; herein referred to as Utica) in OH, USA. Samples were collected from separator tanks on well pads. Aliquots of each sample were neither filtered nor acidified to represent real-world produced water characteristics (e.g., high Fe, hydrocarbons, and total suspended solids content) that may complicate treatment.[64] Samples were used for CO_2 mineralization experiments, where compositions of these streams are shown in Table 5.

Table 5. Utica Point Pleasant and Niobrara produced water compositions used in this study for CO_2 mineralization.

Cation	Utica Point Pleasant (mmol/L)	Niobrara (mmol/L)
Ca	761	6.7
Mg	121	1.9
Fe	1.7	0.4
Na	2495	396
K	17.5	0.88
Sr	31.8	0.51
Ba	0.36	0.33

Cation concentrations for Utica Point Pleasant and Niobrara samples were analyzed via inductively coupled plasma – optical emission spectroscopy (ICP-OES; Avio 200 ICP Opitical Emission Spectrometer, Perkin Elmer). Samples were filtered through a 0.2 micron corning filter and diluted in 5% (w/w) HNO_3 (prepared by diluting 70% HNO_3 in ultra-pure water). Powder X-Ray diffraction (XRD) patterns of the precipitated solids were obtained on an X-Ray diffractometer (Panalytical X'Pert Pro X-Ray Powder Diffractometer) using Cu Kα radiation of 1.5410 Å and used to identify the mineral phases present in the of the precipitated solids. The morphology and microchemistry of the precipitated solids were also evaluated using Hitachi SU5000 field emission scanning electron microscope (FE-SEM) fitted with an Oxford Ultimax 100 mm^2 energy dispersive spectroscopy silicon drift detector. Samples were mounted on a carbon sticky tab, coated in 10 nm of carbon, and examined using a 15 KeV accelerating voltage, 5nA of beam current, and a working distance of ~11 mm.

Thermogravimetric analysis (TGA) was performed on a simultaneous thermal analyzer (STA 6000 Perkin Elmer) with a Pyris data acquisition interface to measure the mass carbonate precipitated of the precipitated solids. The powder samples were heated under ultrahigh purity N_2 purge at a heating rate of 10°C min^{-1} from 50°C – 975°C. Qualitative elemental characterization and scanning electron imaging (SEM) was performed with an electron dispersion spectrophotometer (EDS; Nova 230 model) with a 10 kV accelerating voltage and a working distance of 5 mm.

2.5.2. Pilot plant demonstration for CO_2 mineralization

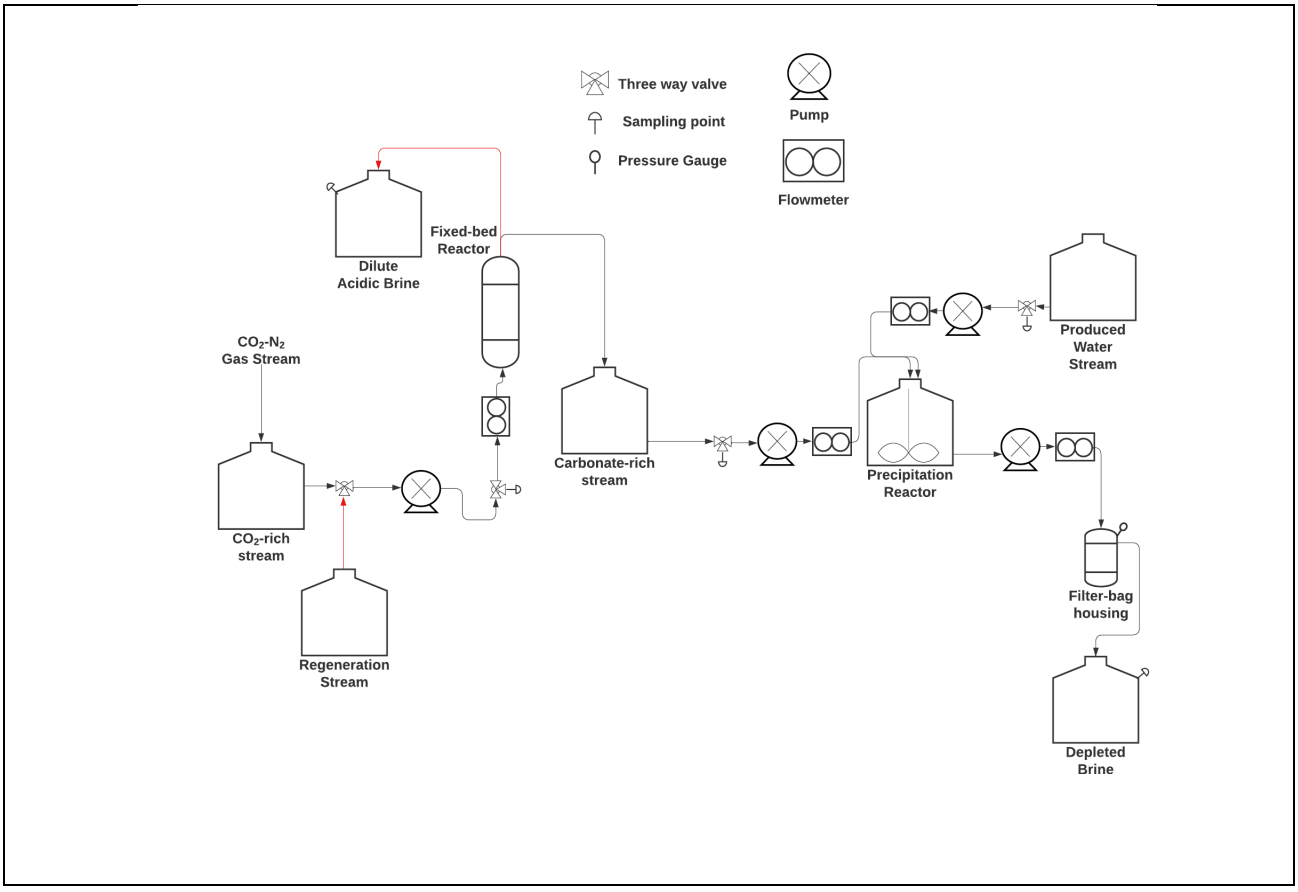

Figure 3. Process flow scheme for the ion exchange demonstration build to treat 300 L of produced water per day. Carbon dioxide rich water (pH 4.25 to 4.66) is directed into fixed-bed reactor and collected before being fed into the precipitation reactor where it is well mixed with a produced water stream. Precipitated solids are removed and collected in a filter bag housing unit and analyzed.

A 2 L PVC fixed-bed reactor (1.5 in internal diameter, 72 in height) containing TP-207 resin was constructed and held in place by installing mesh size 50 screens at both ends of the reactor to treat 300 L of produced water per day for CO_2 mineralization, as shown in Figure 3. Deionized water (temperature at 20°C) is bubbled using a gas mixture of N_2 and CO_2 (10 to 50 SLPM) to create an aqueous stream equilibrated with CO_2 at a partial pressure of 0.03 – 0.20 atm (pH 4.25 to pH 4.66 or $[CO_2]$ = 0.001 - 0.0068 M in accordance with Henry's Law; K_H = 30 L atm mol^{-1}). Equilibrium at the desired CO_2 concentration was determined when a stable pH measurement was achieved at the expected pH with respect to Henry's Law. The CO_2-rich stream is fed to a fixed-bed reactor containing ion exchange resin at varying inlet flow rates of 0.5 – 2.0 L min^{-1} using a gear pump. The carbonate-rich effluent stream is mixed with a fixed volume of Utica Point Pleasant Formation produced water. An overhead mixer is installed in the precipitation tank to ensure turbulent mixing for precipitation (e.g., 750 RPM resulting in Reynolds Number = 49,000). The slurry containing precipitated $CaCO_3$ is then fed through a filter bag housing (solid separator; 3 µm filter bags) where the precipitated $CaCO_3$ and any other precipitated solids are separated from the solution. A synthetic regenerate stream in accordance with effluent

compositions obtained from thermodynamic simulations (~0.5 M NaCl; pH 9 – 11 dependent on volume ratio used) was used to regenerate the fixed-bed reactor.

2.5.3. Fixed-bed ion exchange experiments cycling experiments for CO_2 mineralization

Cycling of the ion exchange process was performed using inlet pCO_2 = 0.12 atm (pH 4.34) at a fixed inlet flow rate = 1.0 L min^{-1} until a breakthrough pH 9.5 was attained. Regeneration of the ion exchange reactor was performed using background 0.5 M NaCl concentrations at pH 9, pH 10, pH 11 and pH 12. The ion exchange resin was regenerated 9 times to demonstrate the number of cycles required to successfully treat 300 L of produced water in 24 hours of operation. CO_2 mineralization experiments were performed using effluent collected from the breakthrough ion exchange cycling experiments using Utica Point Pleasant produced water. The carbonate-rich effluent from the fixed-bed reactor was mixed with the produced water at varying volume ratios in the precipitation tank according to the volume ratio (Equation 11). The IEX solution and produced water were stirred for one hour to maximize $CaCO_3$ precipitation. Filtered effluent solutions concentrations were analyzed via inductively coupled plasma – optical emission spectroscopy as previously described. The solids were further analyzed XRD and SEM/EDS as previously described.

2.5.4. Energy intensity of the pilot plant for CO_2 mineralization

Energy calculations were performed on the process, to account for mixing, pumping, and solid separation from the process and to show the impact this process can have on CO_2 sequestration and utilization.

The hydraulic power used by the pump was found from equation 14[65]

$$P_h = q * h * \frac{\rho}{367} \quad (14)$$

Where q is flow, g is the acceleration of gravity, h is the differential head, and ρ is the density of the liquid.

The shaft power used by the pump was found from equation 15[65]

$$P_s = P_h/\eta \quad (15)$$

Where P_s is shaft power, P_h is the hydraulic power and η is pump efficiency. The power associated with the mixer was calculated using the following equation.[66]

$$P_m = N_p * n^3 * d^5 * g * Re \quad (16)$$

Where $P_m$is the mixing power, $N_p$is the impeller power number, n is the impeller rotational speed, d is the impeller diameter, g is the specific gravity of the fluid and Re is the Reynolds number of the system.

2.5.5. Life cycle assessment

2.5.5.1.Goal and System Boundary

A life cycle assessment (LCA) was conducted in this study to exclusively detail greenhouse gas emissions based on ISO 14040[67] and ISO 14044[68(p140)]. The function of the product system was to produce precipitated $CaCO_3$ via an ion exchange process in the United States in different scenarios and the reference flow of the functional unit (FU) was 1.0 kg of precipitated $CaCO_3$, which is an established measurement basis in the scientific and technical literature[69,70]. The modeling approach adopted was the attributional LCA and the product system extended from cradle to precipitated $CaCO_3$ plant gate, because the use and end-of-use of processes for the product will not differ for the manufacturing technologies. The main goal of this study is to investigate the environmental life cycle impacts of $CaCO_3$ precipitation recovered from utilizing produced water streams. Yield data from treating 300 L of produced water per day is scaled up in the geographical context of the United States (e.g., different regions/sources of produced water from the Appalachian and Denver-Julesburg Basins, different grid-electricity sources for the process, and varying pCO_2) to determine the impacts of different produced water streams.

The system boundaries span from raw material procurement to the actual precipitated $CaCO_3$ manufacturing process as shown in Figure 4. For traditional precipitated $CaCO_3$ production, the boundary includes limestone mining, while in the case of the ion exchange system the solid raw materials are considered to be a waste stream that would be formed, whether or not utilized in precipitated calcium carbonate manufacturing. The system boundary for the precipitation of $CaCO_3$ in Figure 4 adopts a “cradle-to-gate” approach in which it only includes raw material acquisition and manufacturing processes and excludes transportation to distribution site, use and end-of-life (EOL) stages. Thus, the ion exchange system boundary is not extended to

steelmaking processes or to limestone mining, but instead it considers the avoided waste material streams (CO_2 and produced water/brine).

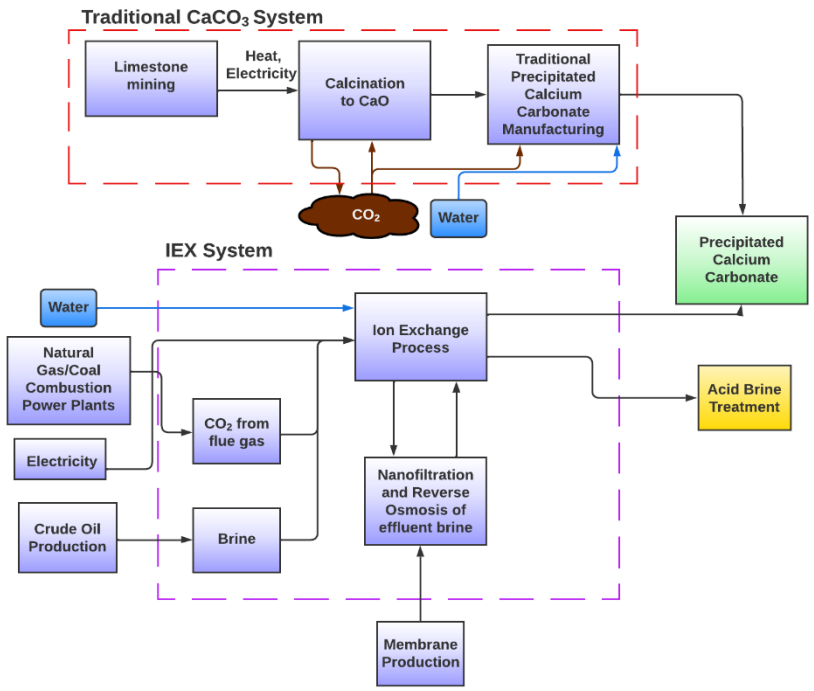

Figure 4. System boundaries (dashed lines) for traditional precipitated $CaCO_3$ production (red) and for precipitated $CaCO_3$ production via the ion exchange process (purple). The traditional precipitated $CaCO_3$ process involves the mining and calcination of limestone to CaO, where CO_2 gas emitted from this step is used as the source for carbonate precipitation (brown). The ion exchange process utilizes CO_2 from flue gas from power plants and brine generated from oil production as the primary sources for carbonate precipitation and a dilute acidic brine is generated from the ion exchange regeneration step (yellow).

Additionally, emissions from the manufacturing of the ion exchange solid used is not considered due to its extensive regeneration capacity (>99%) as discussed in this study. The system is

extended to include membrane filtration treatment steps of the process for the cycling of the ion exchange process at appropriate water recovery ratios. Make-up water is added back into the system to account for water losses from the effluent treatment steps.

2.5.5.2.Allocation and scenarios description

This study investigates the pilot-scale production of precipitated $CaCO_3$ using the best and worst-case scenarios of the process, defined by varying energy-intensive processes, such as the processing of deionized water and effluent brine for cycling the process for the two produced waters investigated in this study. The scenarios to produce 1 kg precipitated $CaCO_3$ are described in Table 6.

Table 6. Summary of the main parameters used in the assessed emissions(?) scenarios for the production of 1 kg precipitated calcium carbonate

Item	S1	S2	S3	S4	S5	S6	S7	S8	S9
Input									
Carbon Source	3%	12%	20%	12%	12%	12%	12%	12%	12%
Produced water	Utica			Niobrara	Utica				
Electricity (USA)	Average				Coal	Natural Gas	Renewable	Easter	Western

Output	Total Utilization (%)								
Dilute Acidic Brine	0	0	0	0	0	0	0	0	0

Nine scenarios for production of calcium carbonate via the ion exchange process were assessed as follows:

- S1 – S3 describe the utilization of CO_2 from flue gas at 3 – 20 vol% CO_2 utilizing the Utica produced water and the average electricity input for the United States accounting for all types of electricity sources.
- S4 describes the utilization of CO_2 from flue gas at 12 vol% CO_2 utilizing the Niobrara produced water and the average electricity input for the United States
- S5 – S9 describe the utilization of CO_2 from flue gas at 12 vol% CO_2 utilizing the Utica produced water and various sources of electricity inputs for the United States

For each scenario, calculated electricity inputs from the pilot plant were input for the precipitation of $CaCO_3$ (e.g., pumping, agitation). A deionized water recovery of 88% is calculated based on traditional nanofiltration and reverse osmosis water recovery rates for brines of similar compositions following mineralization[71,72]. Makeup deionized water is fed back into the system to account for water-reductions from generation of regeneration streams.

2.5.5.3.Life cycle inventory and impact assessment

The life cycle inventory (LCI) was collected using different sources of data provided in the following sections. LCI was mainly obtained from the ecoinvent v3.8 and the NETL CO2U openLCA LCI version 2 databases using the cut-off allocation library found in SimaPro 9.1 software. This LCA study uses the updated ReCiPe 2016 midpoint (H) method available in SimaPro 9.1 software to compare the ion exchange process to the traditional precipitated $CaCO_3$ process. The midpoint method consists of 18 environmental indicators, including global warming, fine particulate matter formation, human carcinogenic toxicity, water consumption, etc. The ReCiPe method is used in this study as it is based on the global average data. Contribution analysis is performed for the precipitated $CaCO_3$ to identify the hotspots only using the global warming indicator. The comparisons between precipitate $CaCO_3$ production processes is performed using the ReCiPe global warming indicator, which is calculated based on the Global Warming Potential (GWP) IPCC 2007 indicator for a time frame of 100 years.

Chapter 3 Ion exchange for CO_2 mineralization studies

3.1.1. Batch equilibrium ion-exchange experiments

3.1.1.1. Introduction

IEX technology is commonly used to purify solutions by removing the dissolved ions by electrostatic sorption into IEX materials of various physical forms.[73,74] All zeolites can serve as IEX materials because of their specific structural features. However, for practical applications, high-alumina zeolites, or zeolites with Si/Al ratios in the range of 1 - 5,[75] are preferred for IEX applications because of the large number of acid sites.[76] IEX and selectivity in zeolites are mainly affected by the properties of the exchangeable cations, the concentration of the solution, the presence of other cations and the characteristics of the zeolite such as channels and Si/Al ratios.[77] Type A and Type X zeolites have high affinities for proton exchange in solutions of pH 3.9 – 7 because of their small Si/Al ratios,[78] making them suitable materials for a pH swing process. IEX resins contain functionalized ionizable groups placed along their polymer-backbone chains and are classified depending on the functional group into weakly (WAC) and strongly (SAC) acidic materials. The high H^+ affinity of WAC resins makes it advantageous to use instead of SAC resins because they can be regenerated using weakly acidic feeds. The pKa of the functional groups on WAC resins are generally greater than 2, whereas SAC resins generally require concentrated acids (pH < 2) because of the functional group's smaller pKa values.[79–83]

Exposing CO_2-saturated solutions (pH = 3.9) to regenerable IEX materials can shift the pH to >10.0, thereby creating favorable conditions for CO_2-mineralization reactions. Ion exchange occurs between an electrolyte solution and similarly charged ions immobilized in an IEX material through a stoichiometric, reversible IEX reaction. Previous research has shown the reversible exchange of H^+ and Na^+ ions in a solution using clay minerals.[39–41] H^+-Na^+ ion exchange is described by equation (17):

$$H^+ + R^{Na} \leftrightarrow R^H + Na^+ \quad (17)$$

where $R^{Na/H}$ is the IEX material in either sodium or proton form and H^+ and Na^+ are ions in solution. Protons in solution are introduced by dissolving CO_2 (pCO_2 = 1.0 atm; pH 3.9) into water according to Equations (2-4). As protons are removed from the solution via ion exchange, the equilibria of reactions 2-4 shifts toward the formation of CO_3^{2-} ions.[84] The resulting solution after IEX is an alkaline, CO_3^{2-}-rich solution that can be used for $CaCO_3$ precipitation without the addition of caustic soda. The regeneration energy requirement for CO_2 capture using solid IEX materials is significantly lower than that of dry solid adsorbent and aqueous amine-based processes due to the absence of heat requirement since the process uses a concentrated sodium chloride waste stream to regenerate the materials (as described in this work).[18]

3.1.1.2. Non-competitive H^+ and Na^+ uptake from DI water

To demonstrate the feasibility of pH shift using TP-207 (R-1), TP-260 (R-2), 4A (Z-1), and 13X (Z-2), increasing amounts of these materials were added to 20 mL of CO_2-saturated DI water (pCO_2 = 1.0 atm; pH = 3.9). 13X and 4A exhibited maximum pH increases to 8.8 and 9.8,

respectively, at solid loading ratios of 0.15 g/g, while the two organic resins increased the solution pH to ~11 at ratios of 0.35 (Figure 5a) within 48 hours. To further quantify the maximum H^+ exchange (i.e., non-competitive) at equilibrium pH values similar to those for a CO_2-saturated solution (pH ~ 4), H^+-Na^+ exchange isotherms (Figure 5b) were collected for the resins and zeolites in DI water. Exchange isotherms were the same using HCl and CO_2-saturated solutions, indicating that there is negligible counter ion (i.e., Cl^-, HCO_3^- or CO_3^{2-}) effect. H^+ exchange capacities at solution equilibrium concentrations of 10^{-4} M H^+ (pH ~ 3.9, similar-to CO_2-saturated water) range from 1.7–2.4 mmol H^+ (g material)$^{-1}$ (circled in Figure 5b), with the organic resins exhibiting higher uptake capacities than the zeolites under more acidic solutions (pH < 4; $[H^+] > 10^{-4}$ M). These data demonstrate the ability of these ion exchange materials to sufficiently shift the pH of aqueous solutions to conditions that favor carbonate precipitation (i.e., pH from 3.9 to >10) via compact flow processes (i.e., 50 g of material required to increase the pH of 1 L of water from 4 to 10; described in more detail in Section 2.3.2).

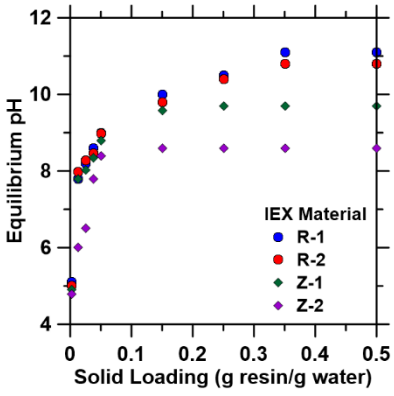

(a)

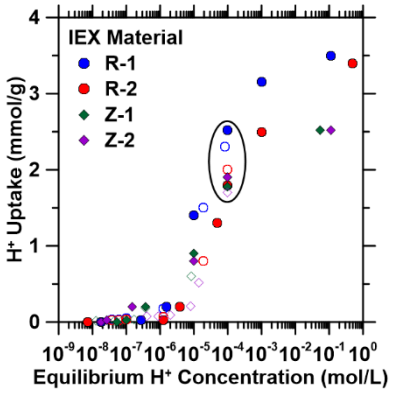

(b)

Figure 5. (a) Changes in the pH of saturated CO_2 solutions (pCO_2 = 1.0 atm; initial pH = 3.9) using various amounts of IEX materials (i.e., 0.010 – 10 grams of IEX material were added to 20 mL of the CO_2-saturated solution). **(b)** H^+ exchange isotherms for organic IEX resins and zeolites in DI water. Batch exchange experiments were conducted using HCl (closed symbols) and CO_2 (open symbols) as a source of H^+ ions. HCl isotherms were developed by varying HCl concentrations from 0.001 to 1 M. CO_2 isotherms were developed by varying mass load at fixed volume of carbonated water at initial pCO_2 = 1.0 atm. Circled area represents the equilibrium H^+ capacities at 10^{-4} M H^+ (pH ~ 3.9, similar to CO_2 saturated water).

3.1.1.3.Competitive exchange between H^+ and Ca^{2+}

Industrial produced water typically contains a variety of ions (in particular, Ca and Mg at 0.1 M and 0.05 M respectively[33]). The organic cation exchange resins used in this study have a high affinity for divalent cations because of the chelating-like functional groups, as they are commonly used for water hardness removal (i.e. removal of Ca and Mg ions from water).[85] Similarly, the zeolites used in this study readily exchange cationic species (e.g., exchange of Na^+ with Ca^{2+} leads to the formation of zeolite Type 5A from 4A).[86] Thus, these affinities for divalent cations may hinder Na^+ and H^+ uptake when using a produced water feed for the pH shift process, so binary component IEX isotherms were generated (Figure 6a-b) using 0.01 – 1 M $CaCl_2$ solutions with fixed initial HCl (1 M for resins, 0.1 M for zeolites to avoid dissolution) or CO_2 (equilibration with pCO_2 = 1.0 atm, pH = 3.9) concentrations to quantify the effect of Ca^{2+} exchange on H^+ uptake capacity. As shown in Figure 6a-b, H^+ uptake decreased (and final pH decreased) with increasing equilibrium calcium concentrations for all materials. These results indicate that a pH swing process

using the materials studied herein requires pH shift of a Ca/Mg depleted stream with subsequent mixing with PW in a separate precipitation reactor (as described subsequently in Section 2.2.4).

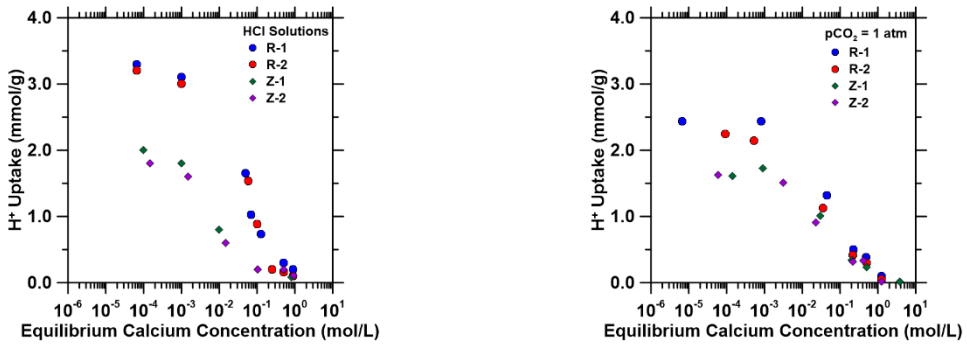

(a) **(b)**

Figure 6. H^+ capacity as a function of equilibrium calcium concentrations (0.001 M – 1.0 M $CaCl_2$) in solution in **(a)** 1 mol/L HCl for resins, 0.1 mol/L HCl for zeolites, and **(b)** aqueous solutions equilibrated with pCO_2 = 1.0 atm (initial pH = 3.9) using a solid/liquid ratio of 0.003 g/mL.

3.1.2. Fixed-bed ion-exchange experiments

3.1.2.1. Effect of inlet concentration on H^+ uptake capacities

CO_2 concentrations by volume from point sources are about 3% for natural gas-fired power plants, 12% for coal-fired power plants and iron and steel mills, 20% for cement plants, and >90% from ammonia, ethanol, and hydrogen plants[87]. An increase in inlet concentrations for IEX processes lead to higher uptake capacities and faster breakthrough time because of the large concentration gradient produced.[88] Therefore, breakthrough curves at varying inlet CO_2 concentrations (0.10,

0.25 , 0.50, and 1.0 atm CO_2) were collected for R-1 IEX resin (the IEX material with the highest H^+ uptake capacity) to probe this effect under flowing conditions.

Breakthrough curves were collected for R-1 at CO_2 concentrations from 0.10 to 1.0 atm (10% - 100%) to quantify its effect on saturation capacities and breakthrough time using an inlet flow rate of 40 ccm and a bed volume of 134.7 cm^3. The breakthrough time decreased as CO_2 influent concentration increased from 0.10 to 1.0 atm and H^+ uptake capacities decreased with decreasing inlet CO_2 concentrations, as shown in Figure 7a and 7b. The maximum uptake capacity was achieved using an initial CO_2 concentration of 1.0 atm at 1.33 mmol/g with minimal changes to the kinetic rate parameter *k*K (~0.050 s^{-1}). The driving force for ion exchange is the concentration difference between the solute on the sorbent and the solute in the solution.[89–91] A high concentration difference provides a high driving force for the ion exchange process, which may explain why higher H^+ uptake capacities were obtained using larger CO_2 inlet concentrations. Additionally, at larger inlet CO_2 concentrations, binding sites are rapidly filled with sorbate H^+ which results in a decrease in breakthrough time. Maximizing H^+ uptake capacities across all concentrations can be performed by increasing bed-depth.

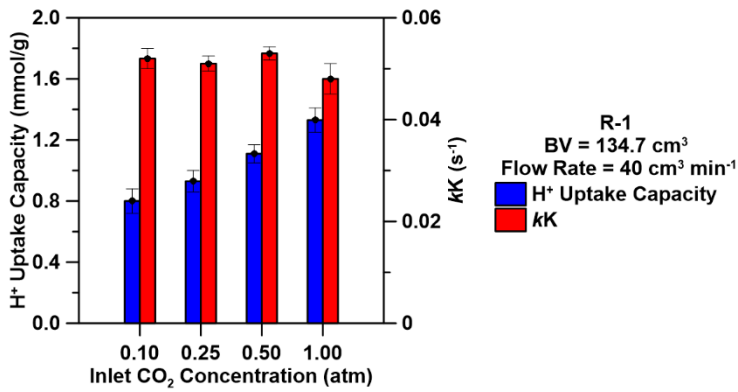

(a)

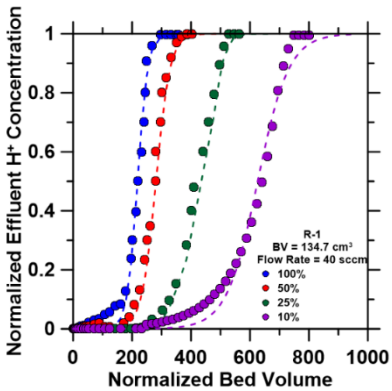

(b)

Figure 7. (a) H^+ uptake capacities (mmol/g) and regressed rate parameter, *k*K, (s^{-1}) and **(b)** effect of influent CO_2 concentration breakthrough curve for H^+ exchange reaction for R-1 at varying CO_2 inlet concentrations using a bed volume of 134.7 cm^3 and an inlet flow rate of 40 cm^3 min^{-1}.

3.1.2.2. Regeneration and cycling of IEX materials

Cycle-to-cycle stability of IEX materials were studied via successive H^+-Na^+ exchange cycles, as shown in Figure 8 (at BV of 12.4 cm^3, flow rate of 40 ccm, H+ exchange pH = 3.9, and Na+ exchange inlet concentrations of 0.7 M NaCl/pH 9.9). Regeneration for all IEX materials was achieved within 100 normalized bed volumes for each cycle, when the effluent pH was equivalent to the inlet pH. Breakthrough curves for all three cycles for each IEX material are shown in Figure 8. The breakthrough time for each material was almost constant for each of their respective cycles, resulting in identical H^+ uptake capacities and rate parameter *k*K values (Table 7).

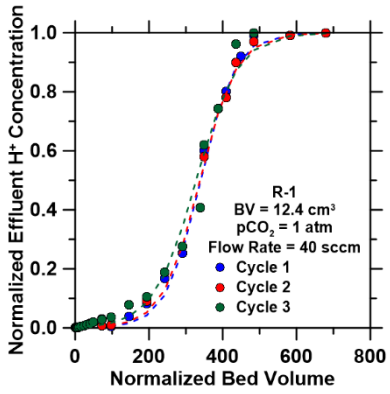

(a)

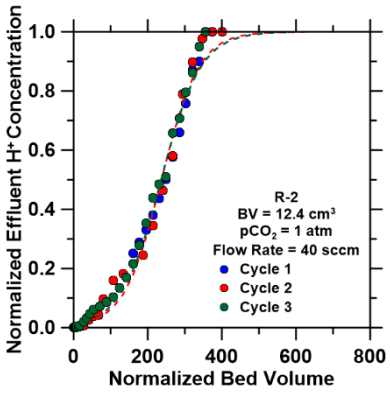

(b)

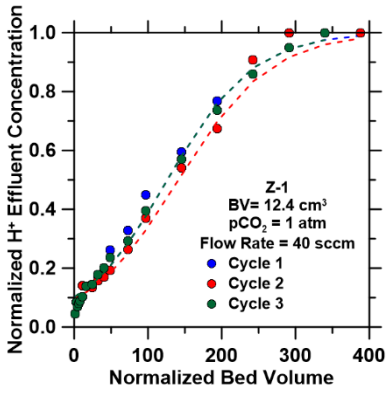

(c)

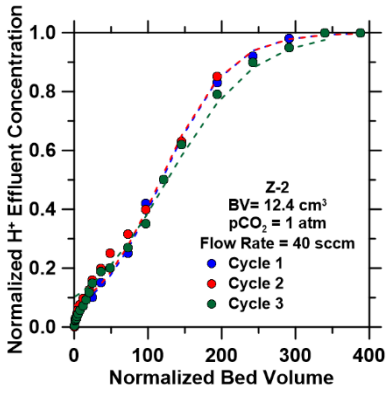

(d)

Figure 8. Breakthrough curves for the H^+ exchange reaction for three cycles after regenerating with an inlet composition of 0.7 M NaCl at a pH 9.9. Breakthrough curves developed using inlet flow rates of 40 ccm and pCO_2 = 1.0 atm for **(a)** R-1, **(b)** R-2, **(c)** Z-1 and **(d)** Z-2. Dashed lines represent Bohart-Adams model predictions for breakthrough curves.

Table 7. Regressed rate parameters using an pCO_2 = 1 atm inlet concentrations for cycled experiments

Material ID	Cycle	H^+ Uptake Capacities (mmol/g)	*k*K (s^{-1})
R-1	1	1.21	0.059±0.003
	2	1.20	0.060±0.005
	3	1.20	0.058±0.002

R-2	1	1.15	0.021±0.004
	2	1.14	0.021±0.002
	3	1.15	0.021±0.003
Z-1	1	0.72	0.035±0.005
	2	0.73	0.034±0.003
	3	0.72	0.035±0.001
Z-2	1	0.67	0.028±0.003
	2	0.67	0.028±0.003
	3	0.69	0.030±0.002

The four IEX materials studied displayed similar H^+ uptake capacities after 3 cycles using a regenerant feed composed of 0.7 M NaCl at a pH 9.9, which is representative of the solution following the mineralization step of this process (discussed in *section 2.3.4*). Regeneration time for the IEX resins can be reduced using higher pH solutions as is done industrially with caustic soda.[79,80,82] More cycles will be necessary to identify the point at which the IEX materials begin to reduce in H^+ uptake capacities.

3.1.3. CO_2 mineralization of simulated PW and IEX solutions

Simulated CO_3^{2-}-rich water with the same Na^+ and CO_3^{2-} concentrations as the IEX columns was mixed with simulated produced water solutions at varying volumetric ratios, V_R (equation 11). As previously shown R-1 displayed a larger pH swing, with a final solution pH 11.1, compared to the other IEX materials. Therefore, thermodynamic simulations were performed to predict phase formation and calcite yield using R-1 compositions as a function of different volume fractions (V_R), shown in Figure 9a.

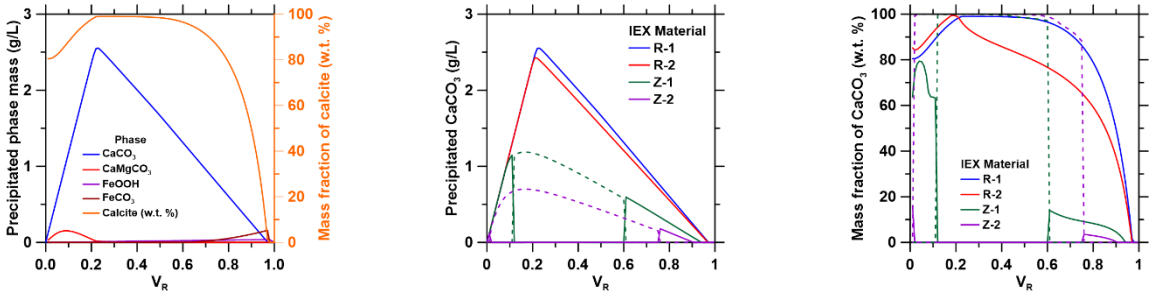

(a) **(b)** **(c)**

Figure 9. (**a)** Simulated phase formation and purity of calcite in alkaline conditions; **(b)** $CaCO_3$ formation and **(c)** purity of calcite formed as a function of varying volume fractions for the four ion exchange solutions studied. The dashed lines for zeolitic materials represent aragonite phase formation.

As shown in Figure 9a, $CaCO_3$ formation changes with varying volume ratio due to increasing [Ca]:[CO_2] ratio in solution. $CaCO_3$ formation is maximized when the [Ca]:[CO_2] ratio was 1:1, which occurs at a V_R of 0.23. R-1 solutions produce the largest quantities of $CaCO_3$ and highest purities of calcite as shown in Figures 9b and 9c, respectively, because of the higher initial pH.

For zeolitic solutions, aragonite formation is dominant between volume ratios of 0.2 to 0.6 because large [Ca]/[Fe] ratios are required to favor calcite formation[55], with goethite as the primary contaminant. The reduction of the initial pH reduces goethite formation which decreases the [Ca]/[Fe] in solution to a point where it enters the miscibility gap of the (Fe,Ca)CO_3 solid solution model used.[55] The $FeCO_3$ end-member forms preferentially but at low quantities which causes aragonite to form in place of calcite. $CaCO_3$ precipitation decreases at $V_R > 0.25$ for ion exchange materials because of the lower initial pH and reduction of aqueous CO_2, reducing the activity of CO_3^{2-} in solution.

To validate the thermodynamic simulations, experiments were performed using R-1 solutions because of the larger predicted mass and purity of $CaCO_3$ precipitated. The dominant phase formed from volume fractions 0.2-0.6 was calcite with goethite as the primary contaminant as shown in the XRD patterns (Figure 10a). At $V_R = 0.1$, monohydrocalcite (MHC) was the primary phase that formed during mineralization as it requires a solution containing [Mg]/[Ca] > 0.2 and [CO_2]/[Ca] > 1 to form.[92–94] When $V_R = 0.1$, the [Mg]/[Ca] and [CO_2]/[Ca] were 0.44 and 2.54, respectively, which are within the parameters required for MHC formation. At $V_R > 0.18$, the [CO_2]/[Ca] < 1.0 thus, MHC did not form after this point.

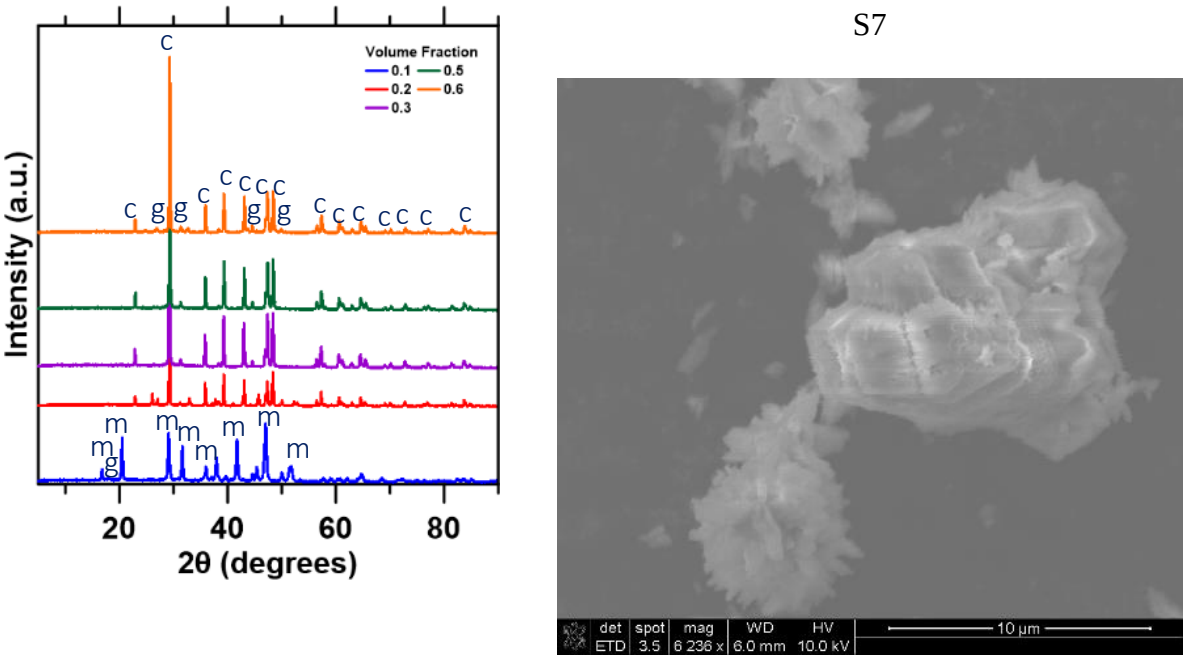

(a) **(b)**

Figure 10. (a) XRD diffraction patterns identifying present phases over varying volume ratios. c = calcite, g = goethite and m = monohydrocalcite; **(b)** SEM image of calcite synthesizes at a volume fraction of 0.7.

The SEM image (Figure 10(b)) of calcite precipitated at $V_R = 0.3$ displays the stable rhombohedral structure expected of calcite formation.[95] The rhombohedral structure was observed for V_R values of 0.2 - 0.6. EDS analysis at the surface was performed to quantify $CaCO_3$ purity. As shown in Table 8, experimental results are consistent with thermodynamic simulations performed for across the volume fractions studied.

Table 8. Mass fraction of calcite, goethite and magnesium within the mineralization samples as determined from SEM-EDS.

	$CaCO_3$ (calcite) (mass %)		Goethite (mass %)		Magnesium (mass %)	
V_R	**EDS**	**Simulated**	**EDS**	**Simulated**	**EDS**	**Simulated**
0.1	97.1	89.9	0.2	0.2	2.7	9.9
0.2	99.0	97.7	0.8	0.7	0.2	1.6
0.3	98.9	99.0	1.0	0.7	0.1	0.3
0.5	97.9	98.4	1.8	1.6	0.3	0.0
0.6	97.2	96.5	2.5	2.4	0.3	0.0

The experimental data and simulated mass balances showed good agreement. Simulated goethite was within 0.3 mass % of the experimental values throughout. Within the range $0.2 < V_R < 0.6$, simulated calcite was within 2 mass % of the experimental values. Significant $CaCO_3$ differences was observed for $V_R = 0.1$ because simulations predicted 9.9 mass % of potential $CaMgCO_3$ phase formation. $CaMgCO_3$ phases were not detected in XRD patterns across all volume ratios leading to differences in the mass of magnesium detected and simulated, implying either the small magnesium content is not detectable by XRD or the magnesium is adsorbed at the surface of the solid.

The precipitated mass of calcite increased and decreased, shown in Figure 11a, following the molar ratios of $[Ca]:[CO_3^{2-}]$, where < 5% difference between simulated and experimental values were observed. The pH was observed to decrease as the V_R increased as shown in Figure 11b, because

of the increasing dilution of the alkaline IEX solution by produced water. The pH buffering effect of carbonate ions is observed up to V_R = 0.43, where pH = 9.6. A significant drop in pH may be the result of increased goethite formation in the system, consuming additional [OH^-] provided by the IEX column. Additionally, simulated pH values were in good agreement with the experimental results as they were within 0.1 - 0.3 pH units. Concentrations of cations increased as the PW ratio increased, shown in Figure 11c. However, calcium concentrations observed a postponed rise due to calcite formation. Iron concentrations do not increase significantly until V_R = 0.46. The available iron at V_R < 0.46 was converted into goethite resulting in [Fe] < 2.3 x 10^{-6} mmol/L. When V_R > 0.46, the iron concentration rose rapidly due to decreasing [OH^-] as the alkalinity provided by the IEX solution decreased. The accurate thermodynamic predictions shown from the experimental results and simulations are significant as they can further be used to predict phase formations and $CaCO_3$ yields for the IEX process using different compositions of PW or of other brine compositions (e.g. desalination brine discharge). $CaCO_3$ yields will be significantly affected by total Ca^{2+} concentrations, whereas purities will significantly be affected by total Mg^{2+} and $Fe^{2+/3+}$ concentrations as the results have shown.

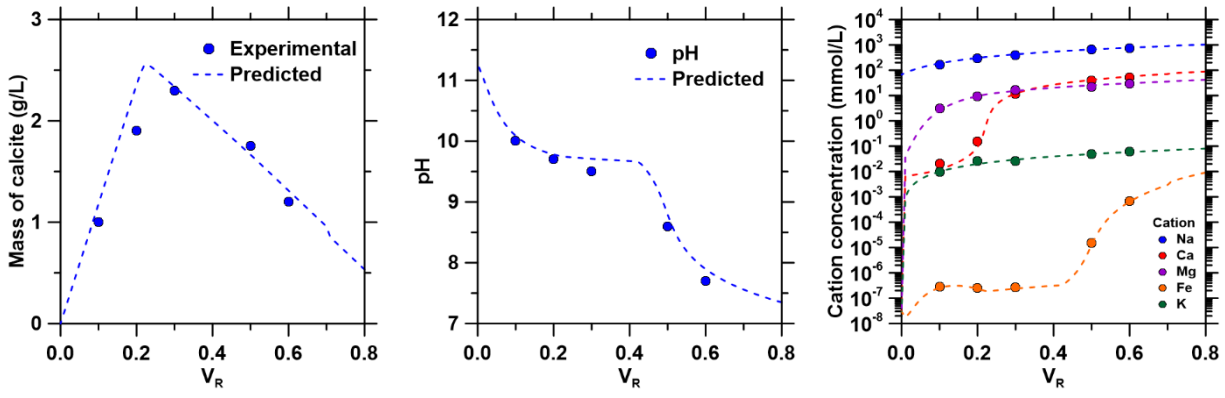

(a) **(b)** **(c)**

Figure 11. **(a)** Yield of precipitated calcite, **(b)** final pH of solution after precipitation and **(c)** cation concentrations in solution following precipitation as a function of volume ratios. The 'filled' circle represent experimental data and the dotted lines represent simulation results.

3.1.4. CO_2 mineralization process design

The results from these studies indicate that ion exchange processes can be used as an alternative to the addition of stoichiometric bases to induce alkalinity for the precipitation of $CaCO_3$. A process flow diagram for the industrial scale setup is shown in Figure 12. CO_2 from flue gas (pCO_2 = 0.12 atm) is combined with fresh water to provide H^+ in solution (pH 4.4) that is used as the inlet solution for the IEX columns. Minor acidic impurities in the flue gas (e.g., sulfur) are not expected to substantially impact the process performance (e.g., H^+ exchange capacities). The carbonate-rich effluent of the columns (pH > 10) is mixed with the calcium-rich produced water in a precipitation reaction to produce $CaCO_3$. Following separation of the solids, the remaining solution undergoes a nanofiltration step for the removal of the remaining divalent cations in solution that would inhibit regeneration of the IEX columns (e.g., Ca^{2+}, Mg^{2+} and $Fe^{2+/3+}$ cations preferably exchanging at the exchanging sites instead of Na^+ cations). Performance studies of nanofiltration membranes are required to quantify the compositions of these cations following this step as they may decrease IEX performance (e.g., regeneration capacities and cycles). A reverse osmosis step is implemented for the continuous production of fresh water that is used in the first step of the IEX process and for simultaneous concentration of sodium cations in solution used for regeneration of IEX columns. The pH in both retentate and permeate streams of the reverse-osmosis step would have to be monitored as this can effect regeneration time and CO_2 absorption. The retentate is transferred to the IEX columns for regeneration, where a larger pH would result in a faster regeneration time.

The permeate is utilized for the initial carbonation step, where a larger pH would result in larger CO_2 absorption, inducing a change in V_R where $CaCO_3$ yields are maximized. The cycling and regeneration efficiency of these IEX materials discussed earlier make this a viable alternative process for CO_2 mineralization at standard temperature and pressure.

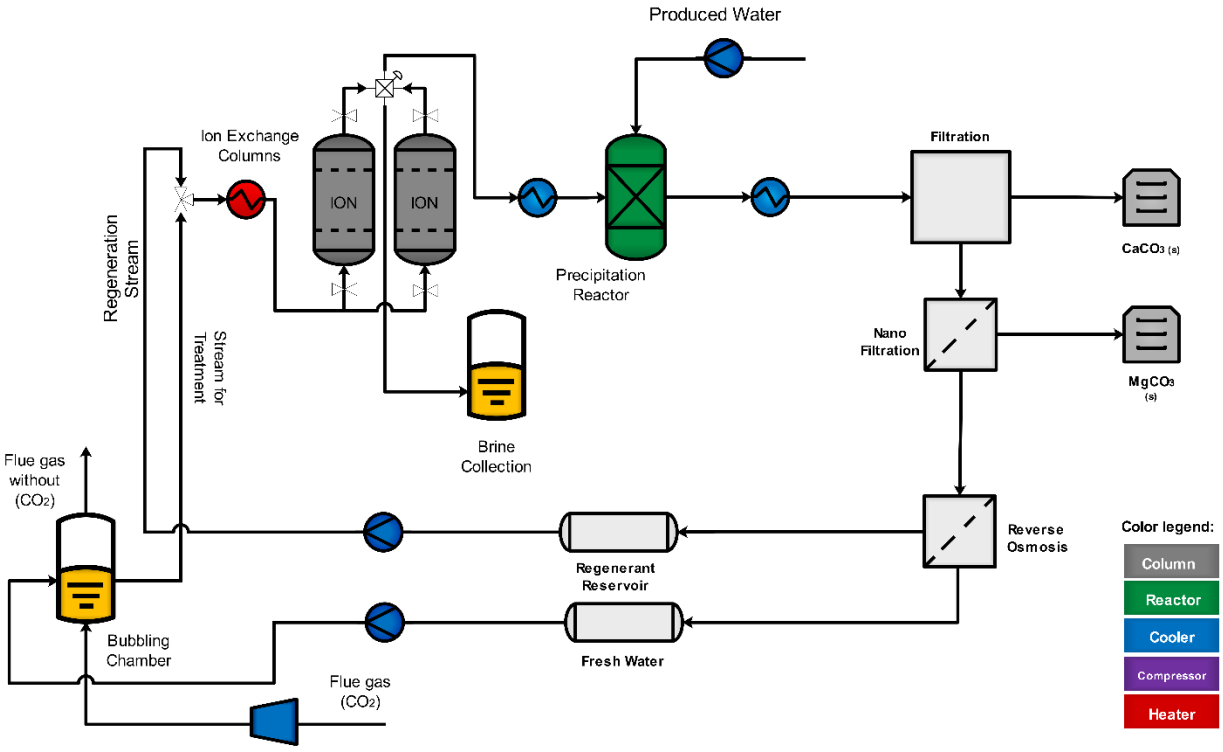

Figure 12. Process flow diagram for industrial scale setup of ion exchange for CO_2 mineralization.

Chapter 4 Linear driving force approximations as predictive models for fixed-bed ion exchange reactors for CO_2 mineralization

4.1. Introduction

Bustillos et. al., have previously demonstrated a regenerable pH swing process (Figure 12)[96,97] that relies on ion exchange to attain favorable conditions for CO_2 mineralization. This process shifts the pH of CO_2-containing aqueous streams from an initial pH 4 to pH > 10, without the need for caustic soda addition. CO_2 from flue gas (pCO_2 = 0.03 – 0.20 atm or pH 4.1 – 4.34) is equilibrated with water to produce an aqueous stream saturated with dissolved inorganic carbon species, as described in equations 2 – 4, where dissolved inorganic carbon concentrations are dictated by Henry's Law and the thermodynamics of CO_2 speciation in water.[98] Using commercially available ion exchange materials, the reversible exchange of Na^+ and H^+ in solution is described by Equation 17.[99,100] Bustillos e. al.[96,97] demonstrated the use of weakly acidic cation exchange resins (e.g., Na-form with iminodiacetic acid functional groups) and synthetic zeolites (e.g., Type 4A and Type 13X) for producing this pH swing: H^+ is removed from the solution while Na^+ is released into solution forming aqueous sodium bicarbonate streams in accordance with Equations 2-4, shifting the equilibrium pH from an initial pH 3.9 to a final pH 11.1. The ion exchange solids can be regenerated using Na-rich brines (e.g., brines containing 0.05 - 3.0 M Na^+)[101,102] following depletion of divalent cations that can inhibit Na-exchange capacities due to competitive behaviors.[96,99] The proposed process depicted in Figure 12: (1) introduces acidity by bubbling CO_2 in deionized water; (2) implementation of H^+ - Na^+ exchange reactions through fixed-bed reactors containing ion exchange solids to produce a carbonate-rich effluent stream for mineralization; (3) induce carbonate precipitation by mixing with a Ca^{2+}/Mg^{2+}-rich brine; (4) separation of

precipitated solids and treatment of the remaining effluent via nanofiltration and reverse osmosis. This final step simultaneously removes divalent cations that can limit regeneration of ion exchange solids (e.g., divalent cation concentrations less than 0.001 M), produces a Na-rich (e.g., concentrations greater than 0.1 M) regeneration stream and produces a fresh water stream and to be cycled within the process.[96,97]

To optimize the use of these ion exchange solids in an industrial setting, the modelling of the fixed-bed reactor in which the ion exchange reaction takes place becomes an important task. In this process, the contact between the H^+ in CO_2 saturated solutions and the solid ion exchange phase can be studied at three scales: the bed scale, the pellet scale, and the grain scale.[103] The H^+ in solution flows through the packed fixed-bed reactor of granular medium whose properties change in space and time upon progression of the process. The H^+ travels from the bulk of the flowing liquid to the surface of the ion exchange solid and diffuses through layers of product phase and pores of fresh materials to reach ion exchange sites available for reaction.[104] Mathematically simple linear driving force models to describe the system in terms of the ion exchange solid H^+ titration capacity (mmol H^+ g^{-1} solid) and the kinetic sorption rate parameter. These models provide quantitative approximation for ion exchange systems when the equilibrium constant is sufficiently large.[105] Linear driving force models are used to predict H^+ titration capacities and sorption rate parameters at varying operating conditions for four commercially available ion exchange solids: weakly acidic resins TP-207, TP-260 and synthetic zeolites Type 4A and Type 4X. The concentration-time profiles for H^+ exchange in the reactor effluent were analyzed using Bohart-Adams model, a quasi-chemical model derived by Bohart and Adams. A range of process conditions (e.g., ion exchange pellet size, contact time) were varied to probe their effects on the parameters of the models as well as to determine the apparent rates of reaction and diffusion

occurring at the molecular scale.

4.2. Effects of reactor parameters and ion exchange solid size on H^+ titration capacity and ion exchange rates

Fixed-bed H^+ exchange experiments were conducted to determine the impact of transport phenomena on exchange capacities and to quantify ion exchange rates so that ion exchange reactors can be sized for various process conditions (e.g., various inlet pH and liquid contact times). The performance of the fixed-bed columns was quantified using linear driving force models described in *Section 2.2.3*. Flow rate is a key parameter to evaluate the efficiency of ion exchange materials in a continuous process because contact time and column hydrodynamics (e.g., Reynolds number) can impact ion exchange capacities.[106–109] Breakthrough tests were performed at a fixed bed volume with increasing inlet flow rates (e.g., Re = 0.25 – 19.4) to quantify the effect on H^+ titration capacities (Figure 13) and ion exchange rate parameters (Figure 14b).

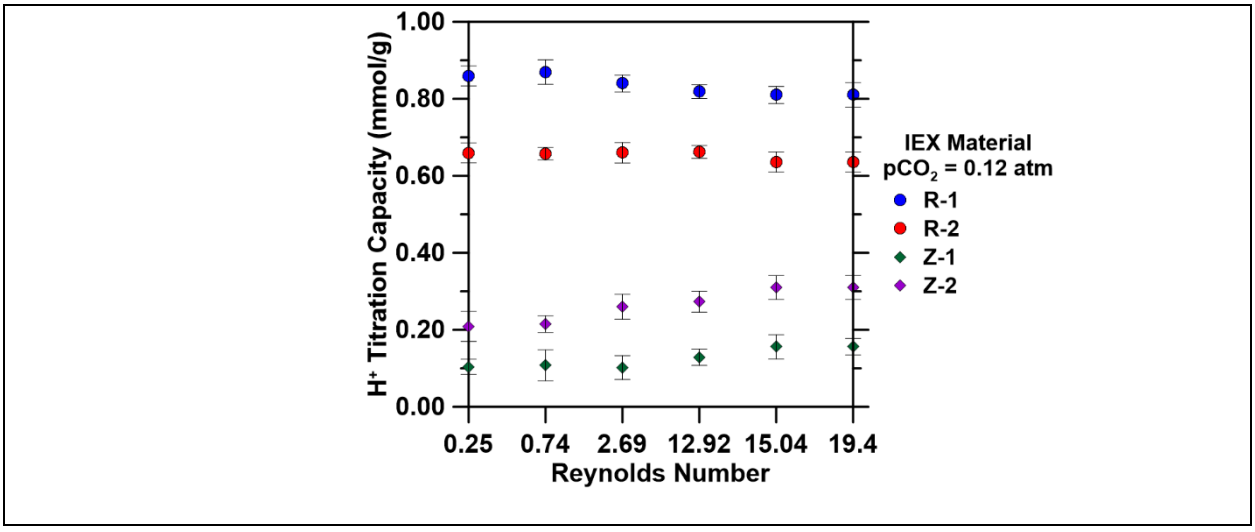

Figure 13. Effect of varying Reynolds number on fixed-bed H^+ titration capacities of the four ion exchange solids a fixed inlet pCO_2 = 0.12 atm. Column heights and diameters were varied to maintain equivalent 10 minute contact times at each Reynolds number.

Experimental H^+ titration capacities were quantified when the outlet H^+ concentration was equivalent to 95% of the inlet H^+ concentration. As shown in Figure 13, increasing the Reynolds number (e.g., larger flow rate and minimized effects of laminar flow) results in similar H^+ titration capacities, equivalent previously quantified equilibrium capacities in Bustillos, et. al.,[96,97] for the four ion exchange solids at 10-minute contact times. The equilibrium H^+ titration capacities achieved at pCO_2 = 0.12 atm are: 0.81 mmol H^+ g^{-1} of R-1, 0.68 mmol H^+ g^{-1} of R-2, 0.26 mmol H^+ g^{-1} of Z-1, and 0.18 mmol H^+ g^{-1} of Z-2. Additionally, the second order linear driving force model was used to quantify the rate parameter, kK. Breakthrough curves at Re = 19.4 are shown in Figure 14a, with Bohart-Adams model applied (dashed lines) and used to predict the H^+ titration capacity (Table 9) and quantify the ion exchange rate parameter at increasing Reynold numbers (Figure 14b).

Table 9. Experimental and predicted H^+ titration capacities of fixed-bed reactors operated at increasing Reynolds numbers and an inlet pCO_2 = 0.12 atm.

Ion Exchange Material	Reynolds Number	Experimental H^+ Titration Capacity (mmol/g)	Bohart-Adams Predicted H^+ Titration Capacity (mmol/g)
R-1	0.25	0.86	0.91
	0.74	0.88	0.90
	2.69	0.84	0.89
	12.92	0.82	0.90
	15.04	0.81	0.88
	19.4	0.81	0.87
R-2	0.25	0.66	0.71
	0.74	0.66	0.70
	2.69	0.67	0.72
	12.92	0.64	0.69
	15.04	0.64	0.68
	19.4	0.63	0.67
Z-1	0.25	0.21	0.20
	0.74	0.22	0.26
	2.69	0.26	0.33
	12.92	0.27	0.36
	15.04	0.31	0.34
	19.4	0.30	0.35

Z-2	0.25	0.10	0.18
	0.74	0.11	0.19
	2.69	0.10	0.18
	12.92	0.13	0.21
	15.04	0.16	0.19
	19.4	0.16	0.16

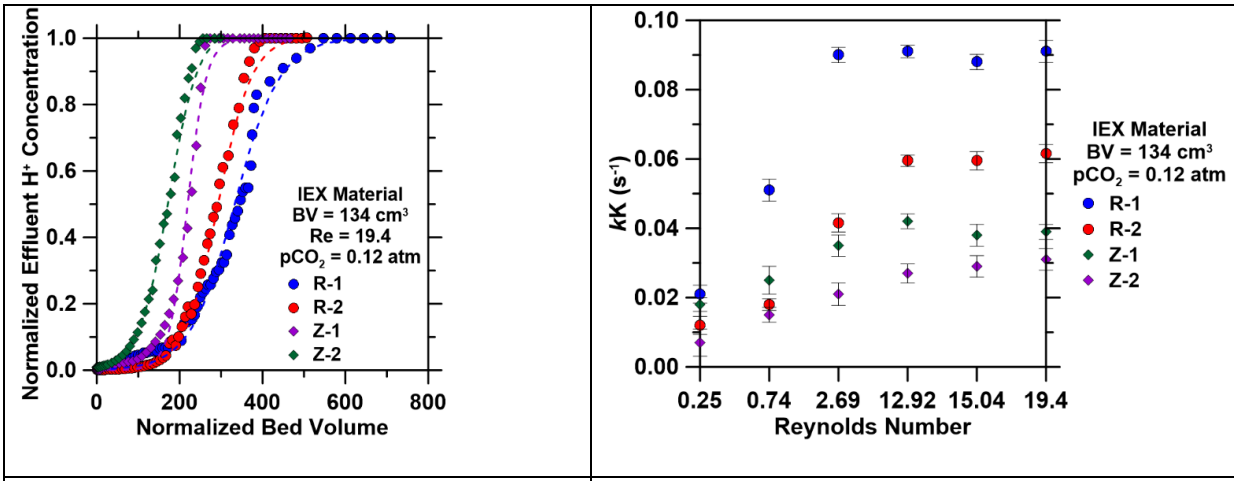

(a) **(b)**

Figure 14. (a) Breakthrough curves for H^+ exchange at a fixed bed volume of 134 cm^3, fixed inlet pCO_2 = 0.12 atm and fixed Re 19.4. Dashed lines represent Bohart-Adams model fitting with **(b)** regressed rate parameters shown as a function of increased Re number.

Increasing the Re at the inlet of the system and over the particle led to an increase in *k*K for all ion exchange materials. The regressed rate parameter increased from 0.02 – 0.091 s^{-1} for R-1, 0.018 –

0.06 s^{-1} for R-2, 0.015 – 0.04 s^{-1} for Z-1, and 0.012 – 0.025 s^{-1} for Z-2 at Reynolds numbers ranging from 0.25 – 19.4. Increase of these rate parameters for all ion exchange materials demonstrates that the overall system kinetics is dominated by external mass transfer in the column.[110–114] Under convective mixing, the ion-exchange rate increases as the mixing speed increases (e.g., inlet liquid flow rate in this case), and the resistance of the boundary layer that surrounds the ion exchange materials weakens.[115] When diffusion is the rate-limiting step, then the rate-limiting diffusion process may not be within the micropores themselves but, instead, limited by transport via a near static-boundary layer that is inserted between the external solution and the crystalline surface.[116] This process is described as film or boundary-layer diffusion. However, shown in Figure 14b, minimal changes to the rate parameter *k*K are observed at Re > 3 for all ion exchange materials: 0.091 s^{-1} for R-1, 0.06 s^{-1} for R-2, 0.04 s^{-1} for Z-1, and 0.025 s^{-1} for Z-2. These minimal changes in rate parameters indicate decreased influence of film diffusion limitations. At this point, *k* represents intraparticle diffusion rates that define the kinetics of the ion exchange process and can be used for scale-up design depending on the type of material used.

To describe the changes in saturation capacities and model fit with pellet size, the H^+ exchange process must be deconvoluted at the pellet and grain scale. The sorbent synthetic pellet or ion exchange bead is a porous agglomerate comprising packed nonporous grains. The effect of particle diameter size on the inverse ion exchange rate parameters, 1/*k*K (Equation 10), for each ion exchange solid at Re 19.4, where minimal changes to the rate parameter are observed for each material, to further demonstrate intraparticle diffusion rate limitation effects on the ion exchange process.

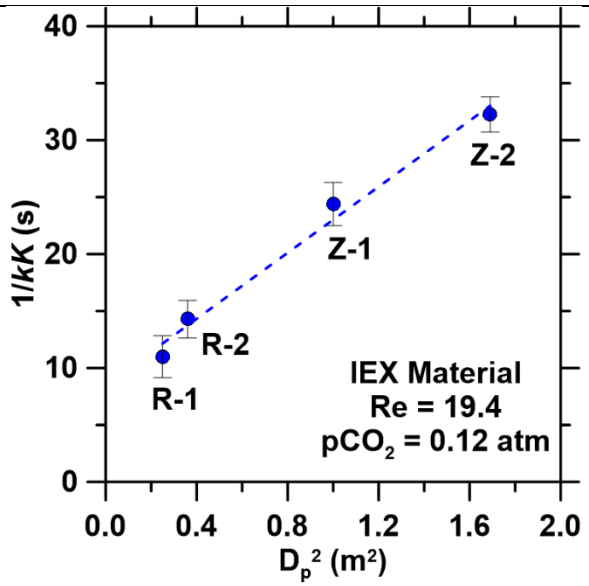

Figure 15. Overall rate resistance, 1/*k*K, from Bohart-Adams regressed rate parameter at various ion exchange particle sizes for fixed bed volume and Re 19.4 at an inlet pCO_2 = 0.12 atm.

As shown in Figure 15, the inverse rate parameter increases and is proportional to the square of the ion exchange pellet's diameter for an inlet pCO_2 = 0.12 atm stream at Re 19.4. For large pellets (e.g., >500 µm) the outer surface of the pellet reacts instantaneously with H^+ in solution but the propagation of the reactant front through the pellet is limited by high pore-diffusion resistance, R_p, which is proportional to the square of the pellet's diameter (Equation 10).[117] The propagation of the ion exchange reaction follows a nucleation process where the rate increases as nuclei connect (e.g., within 100 – 200 normalized bed volumes for each ion exchange material). After this regime, H^+ layer accumulates which results in restricted access to unreacted core grains due to the high solid-diffusion resistance (e.g., incomplete conversion of individual grains) and decrease in the porosity of the pellet due to pore clogging and collapsing (e.g., incomplete conversion through

pellet volume). This combined effect is captured by the Bohart-Adams model through the inflection point of the breakthrough curves (Figure 14a). These results show the ion exchange process is limited by intraparticle diffusion at Re > 3, in which scale up design should be operated at these increased convective mixing conditions.

Chapter 5 Process simulations reveal CO_2 removal potential of the proposed ion exchange process

5.1. Introduction

Generating energy and clean water inexpensively at abundant rates has been the primary driver for the technological advancement of humans. However, harvesting the necessary fossil fuel resources has produced (and continues to produce) billions of metric tonnes (t) of waste in the form of CO_2-containing gaseous effluents and saline wastewater. In 2019, >6 billion tonnes of CO_2 were being emitted from the combustion of fossil fuels for power generation (2.5 billion t CO_2), industrial processes (2.1 billion t CO_2), and transportation (1.9 billion t CO_2),[118] while 22 billion barrels of liquid-waste water (known as produced water) was produced during oil and gas extraction.[29–32] Furthermore, the production of freshwater via sea- and river-water desalination has begun to increase (e.g., current global reverse osmosis capacities of 99.9 million cubic meters per day[119]) to combat increasing global freshwater scarcity,[61,62,120,121] leading to increasing levels of saline brine waste and CO_2 emissions [0.4 – 6.7 kg CO_2 equivalent per m^3 of water processed].[122]

An attractive strategy to simultaneously limit brine discharge and CO_2 emissions involves reacting aqueous streams containing Ca and Mg cations with CO_2-containing gaseous streams to produce stable solids (usually in the form of calcium or magnesium carbonates) via mineralization reactions.[26,123] Mineralization-based CO_2 mitigation processes (1) avoid separation, concentration, and storage steps (e.g., steps in the post-combustion capture of CO_2 from power plants using amine-based processes[7,8,9]), (2) exploit favorable reaction thermodynamics (e.g., ΔG = -1129.1 kJ/mol for calcite precipitation) and (3) are insensitive to the impurities in CO_2-containing streams (e.g., hydrocarbons and H_2S). Therefore, these approaches involve reduced process complexity (compared to traditional thermal swing amine-based processes[15]) and can be applied across a wide

range of operating conditions without substantial increases in energy requirements and without the need for as-yet-developed CO_2 storage and monitoring infrastructure.

Produced water and reverse osmosis brines are rich in Na^+, Ca^{2+}, Mg^{2+} and Cl^- ions (0.050 M – 3.0 M).[33] These high cation concentrations make these streams viable sources of cations for mineralization processes. However, these streams are typically produced at 4 < pH < 7 (with bicarbonate, HCO_3^-, as the predominant dissolved carbon species)[33], and alkalinity (i.e., OH^- ions) needs to be supplied to drive the formation of carbonate ions (CO_3^{2-}) ions that facilitate spontaneous precipitation reactions according to Equations 18-20 (e.g., in water, CO_3^{2-} is the dominant carbon species at pH > 10.3[27,28]):

$$H_2CO_3\,(aq) \rightleftharpoons H^+(aq) + HCO_3^-\,(aq) \quad (18)$$

$$HCO_3^-\,(aq) \rightleftharpoons H^+(aq) + CO_3^{2-}\,(aq) \quad (19)$$

$$Ca^{2+}(aq) + CO_3^{2-}\,(aq) \rightarrow CaCO_3(s) \quad (20a)$$

$$Mg^{2+}(aq) + CO_3^{2-}\,(aq) \rightarrow MgCO_3(s) \quad (20b)$$

We have previously demonstrated a regenerable pH-swing process (Figure 1)[59] that utilizes commercially available ion exchange materials to shift the pH of CO_2-containing aqueous streams from 4 to ~11, thereby avoiding the need for expensive additives such as caustic soda (NaOH). In this process, protons in solution are introduced by dissolving CO_2 from flue gas (pCO_2 = 0.05 – 0.50 atm) according to Equations 18 – 19 in water. The pH of this aqueous stream is increased from pH 3.9 - 4.5 (depending on the concentration of CO_2 in the gaseous stream) to pH > 10 using an ion exchange material following the reversible exchange of H^+ and Na^+ in solution described by equation 21[39–41,59]:

$$H^+ + X^{Na} \leftrightarrow X^H + Na^+ \quad (21)$$

where $X^{Na/H}$ is the ion exchange material in either sodium or proton form and H^+ and Na^+ are ions in solution. As protons are removed from the solution via ion exchange, the equilibria of reaction 18 – 19 shift toward the formation of CO_3^{2-} anions, dictated by Henry's Law and the thermodynamics of CO_2 speciation in water[124]. The resulting solution is alkaline and CO_3^{2-}-rich, suitable for $CaCO_3$ precipitation. As described in Bustillos et. al.[59], weakly acidic resin TP-207 (Na-based, iminodiacetic acid functional groups) induced a pH shift from a CO_2 saturated solution (e.g., initial pH 3.9; pCO_2 = 1.0 atm) to a final pH 11.1 (0.034 mol/L CO_3^{2-}), resulting in $CaCO_3$ precipitation when mixed with simulated brine streams (0.025 mol/L $CaCO_3$). Bustillos et. al. additionally detailed varying capacities (e.g., varying effluent CO_3^{2-} concentrations following ion exchange from 0.01 – 0.025 mol/L CO_3^{2-}) using different types of ion exchange materials (e.g., zeolites Type A and Type X, weakly acidic resin containing phosphonic acid functional groups).[59] For this work, TP-207 resin is selected to simulate alkaline composition as it displayed the largest pH swing (e.g., larger H^+ capacities) compared to the different ion exchange materials studied.[59]

Furthermore, following ion exchange as shown in Figure 16, the CO_3^{2-}-rich effluent (0.0018 – 0.034 mol/L CO_3^{2-} depending on the initial dissolved CO_2 concentrations) is produced from the ion exchange beds and is mixed with the calcium-rich produced water in a precipitation reactor to produce $CaCO_3$. Following separation of the solids, the supernatant solution undergoes a nanofiltration step for the removal of the remaining divalent cations in solution (e.g., Ca^{2+}, Mg^{2+} and $Fe^{2+/3+}$) and a reverse osmosis step to separate Na^+ ions. These steps recycle water (e.g., roughly 8:2 ratio for reverse osmosis product streams: produced water input) for subsequent carbonation and Na-rich streams for regeneration of ion exchange columns.

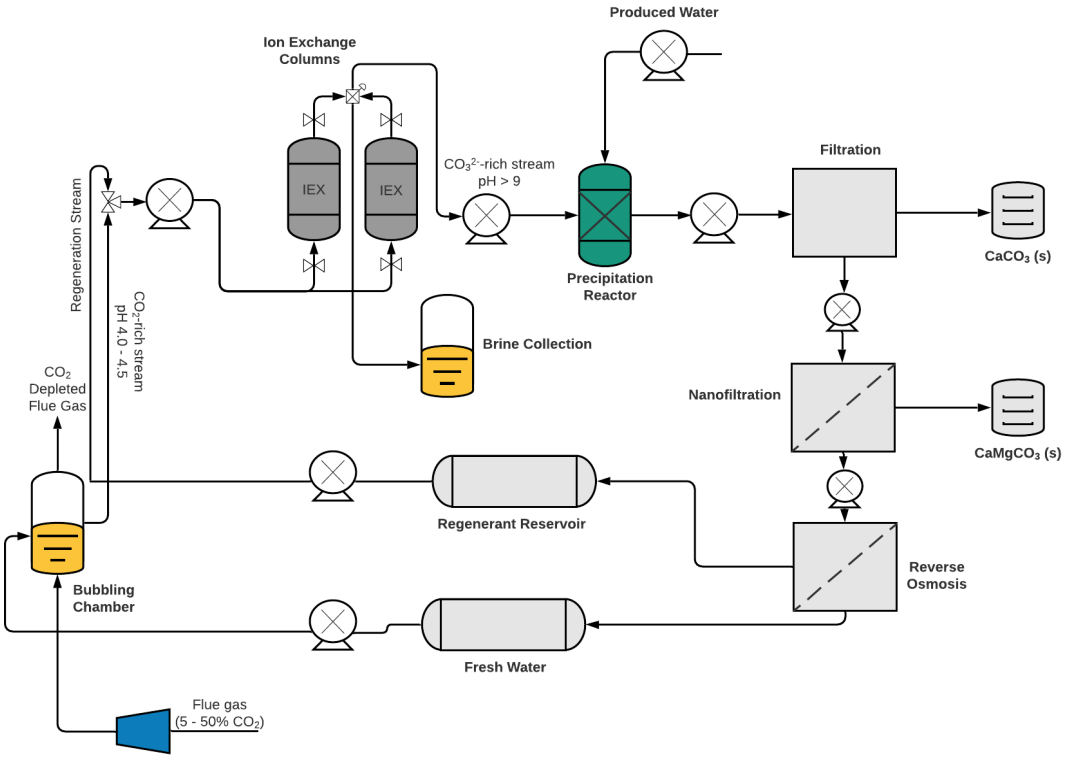

Figure 16. Process flow diagram for industrial scale setup for CO_2 mineralization via an ion-exchange based pH swing.[59]

Our previous studies generated design guidelines for the production of high purity (>97 wt.%) $CaCO_3$ at yields (2.3 t $CaCO_3$/day, equivalent to 1 t CO_2 captured/day) that utilize 3.5 m^3/h of brine from a total bed volume of 0.05 m^3 of regenerable ion exchange material.[59] This work seeks to quantify the emissions mitigation impact of our process by using thermodynamic and process simulations to determine energy consumptions and calcium carbonate yields for various produced water and CO_2 waste streams. Herein, we demonstrate that implementing this process for CO_2 mineralization results in net negative carbon emissions for the various produced water

compositions studied. Energy requirements and costs of the process significantly decrease when utilizing higher CO_2 flue gas concentrations.

5.2. Process simulations for maximum thermodynamic calcite yields utilizing a range of produced water compositions are realized at an initial [Ca]:[CO_2] ratio of 1:1

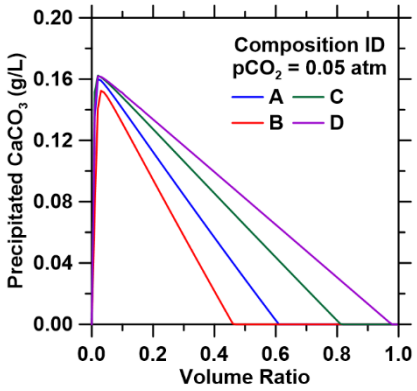

(a)

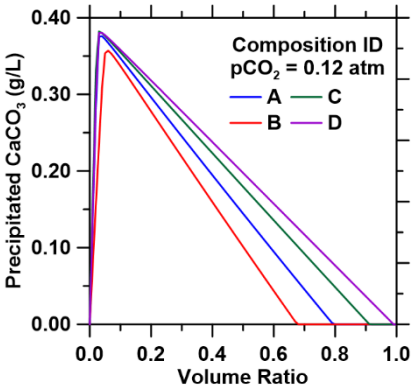

(b)

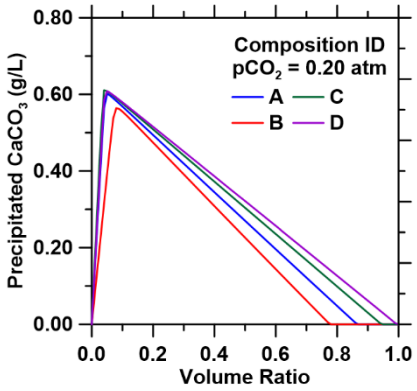

(c)

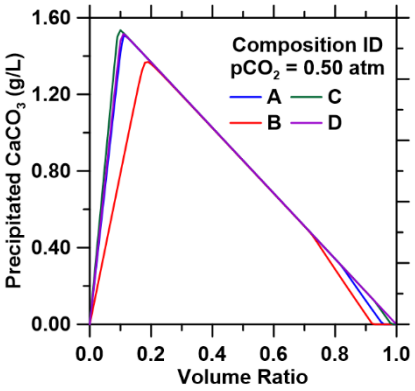

(d)

Figure 17. Simulated effect of various CO_2 concentrations on precipitated $CaCO_3$ mass as a function of volume ratio (the ratio of produced water volume to total volume) at (a) 0.05 atm, (b) 0.12 atm, (c) 0.20 atm and (d) 0.50 atm initial CO_2 partial pressure for different produced water compositions. Thermodynamic simulations were performed at 25 °C and at fixed total volume.

Similar-to the composition of produced water by source/location, the CO_2 concentrations by volume within gaseous emissions from point sources vary depending on the industry. Specifically, these values are 3% for natural gas-fired power plants, 12% for coal-fired power plants, up to 30% for iron and steel mills, 40% for cement plants, and >90% from ammonia, ethanol, and hydrogen plants[1]. To probe the impact of various gas phase CO_2 and aqueous phase ionic concentrations on calcite yield via the previously demonstrated process, thermodynamic calcite yields (Figure 17) were calculated (using GEMS as described in *Section 2.2.5*) at various conditions and V_R (see Equation 11). The produced water compositions for these calculations represent the four compositions listed in Table 4 (A, B, C, and D). The composition of the carbon-containing water in these simulations is derived from the results of our previous ion-exchange experiments (1.7 – 16.8 mmol/L CO_3^{2-} and pH 10.1 – 10.9)[59]. These streams reflect water that was initially equilibrated with gas phase CO_2 streams with various partial pressures (pCO_2 = 0.05-0.50 atm) and then exposed to an ion-exchange material to shift its pH from ~4 to 11.[59]

As shown in Figure 17, the mass of precipitated $CaCO_3$ varies for each composition (compositions A, B, C, D) and initial CO_2 concentration because of dissolved calcium concentrations and

contaminant phases formed. The maximum mass of precipitated $CaCO_3$ for the selected produced water compositions varies from 0.15 – 0.16 g/L, 0.35 – 0.38 g/L, 0.55 – 0.6 g/L and 1.30 – 1.55 g/L for 0.05 atm, 0.12 atm, 0.20 atm and 0.50 atm CO_2, respectively (Figure 17). The mass of precipitated $CaCO_3$ varies with the volume ratio because the mass precipitated is dictated by whichever reactant is in excess, as shown in Figure 18.

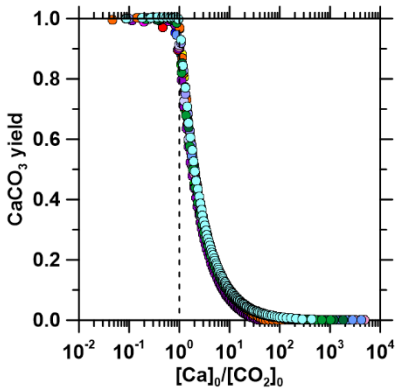

Figure 18. $CaCO_3$ yield for all produced water compositions (Table 1) at pCO_2 = 0.05 – 0.50 atm, as a function of initial calcium to initial CO_2 ratios. $CaCO_3$ yield is quantified as the ratio of mol $CaCO_3$ precipitated to mol initial calcium, where a value of 1 represents total conversion of initial available calcium in solution. The vertical dashed line represents the ratio of [Ca]:[CO_2] equivalent to 1.

Shown in Figure 18, when the initial [Ca]:[CO_2] ratio is less than 1 (e.g., when CO_2 is in excess), $CaCO_3$ yields are greater (0.9), indicating that almost all available calcium in solution precipitates to form $CaCO_3$. The increase in initial [Ca]:[CO_2] ratios corresponds to an increase in the mass of precipitated $CaCO_3$ produced at smaller volume ratios, as shown in Figure 11. $CaCO_3$ yields are maximized when the initial [Ca]:[CO_2] ratio is 1:1 (Figure 17), which occurs at smaller volume ratios for smaller CO_2 concentrations (Figure 17).

Similarly, the maximum mass of precipitated $CaCO_3$ increases with larger initial CO_2 concentrations (Figure 17) because of the increased concentration of carbonate ions speciated from CO_2. When the initial [Ca]:[CO_2] ratio is larger than 1, CO_2 becomes the limiting reagent of the mineralization reaction which results in significant reductions in the mass of precipitated $CaCO_3$ formed (Figure 17 at larger volume ratios) and significant reduction in $CaCO_3$ yields. Significant differences in yields are observed using produced water Composition B because of significantly smaller Ca^{2+} concentrations compared to the other compositions studied, resulting in a greater amount of contaminant phases precipitated, as highlighted in Figure 19 for pCO_2 = 0.50 atm.

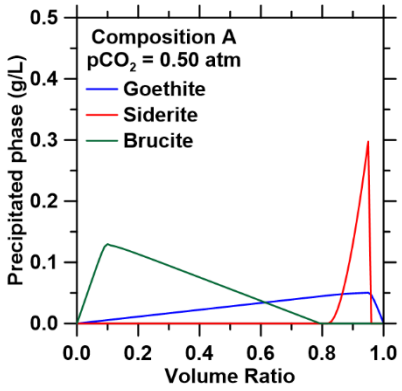

(a)

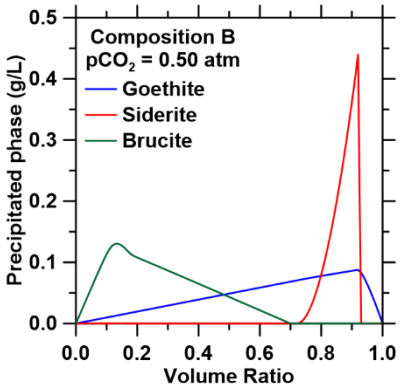

(b)

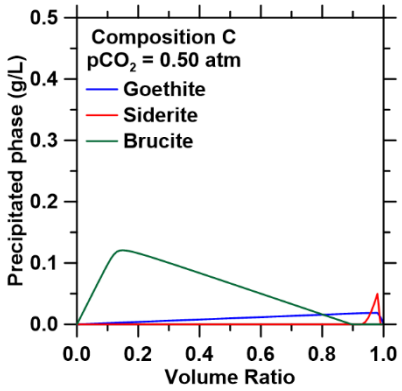

(c)

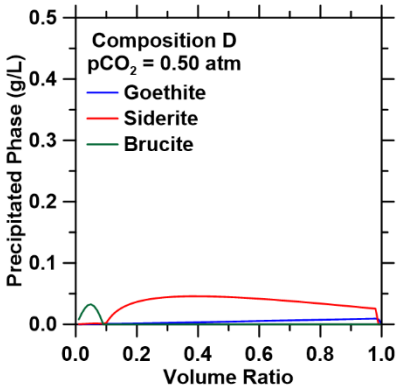

(d)

Figure 19. Effect of produced water compositions and varying CO_2 concentrations on simulated impurity phases precipitated as a function of volume ratio at (a) 0.05 atm, (b) 0.12 atm, (c) 0.20 atm and (d) 0.50 atm CO_2 concentrations.

Additionally, as shown in Figure 20, purities are maximized at optimal volume ratios (e.g., where maximum precipitated $CaCO_3$ is achieved) and achieve up to 99.8% $CaCO_3$ purity. Smaller initial calcium concentrations combined with the increase in contamination cations (e.g., Fe) results in larger contamination phase formation (e.g., brucite [$Mg(OH)_2$], goethite [FeOOH] and siderite [$FeCO_3$] respectively), decreasing purities of $CaCO_3$ precipitated.

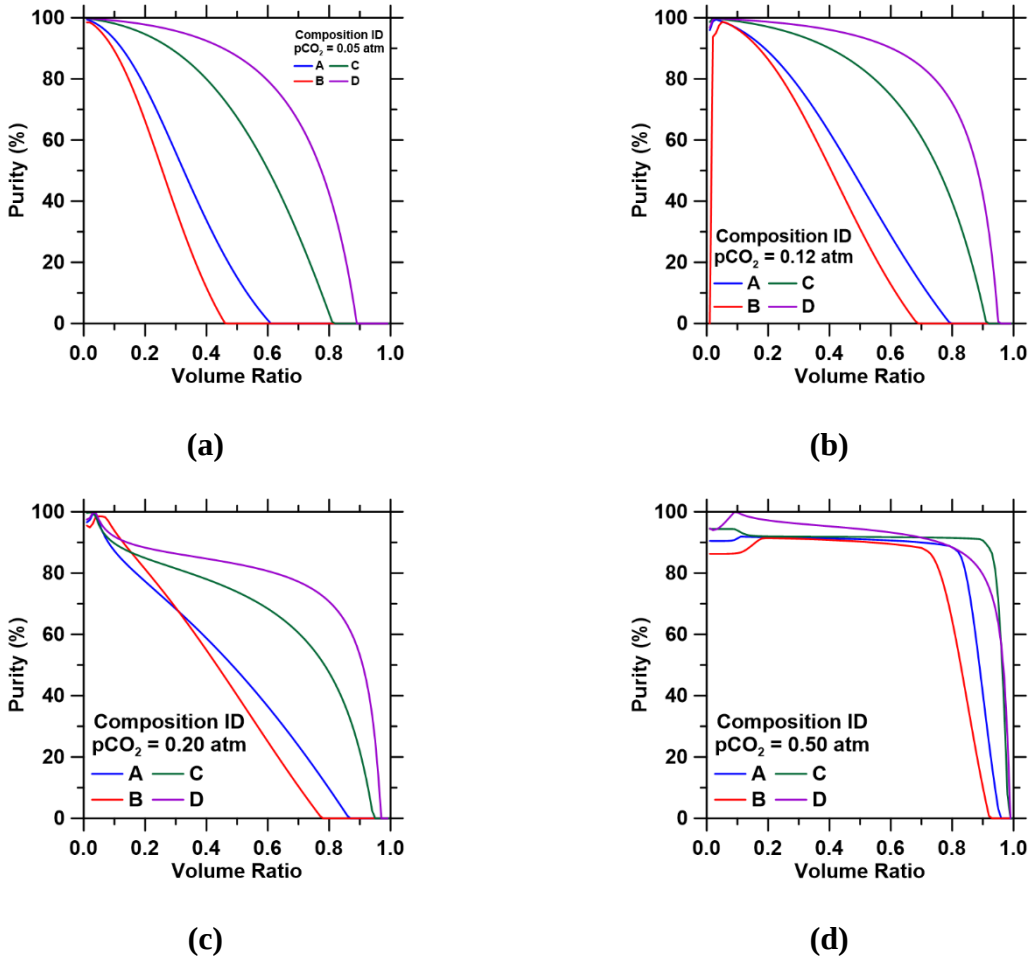

Figure 20. Effect of produced water compositions and varying CO_2 concentrations on $CaCO_3$ purities as function of volume ratio at (a) 0.05 atm, (b) 0.12 atm, (c) 0.20 atm and (d) 0.50 atm CO_2 concentrations.

Thermodynamic simulations were performed to predict the precipitated $CaCO_3$ yields (per L of water processed) using partial pressures of CO_2 representative of those found in industrial waste streams. Quantifying the influence of initial [Ca]:[CO_2] ratios on $CaCO_3$ yield provides insight for industries interested in either maximizing $CaCO_3$ production or CO_2 removal (e.g., operating under Ca or CO_2 limited regimes). The maximum $CaCO_3$ precipitated as a function of CO_2 concentration for an initial [Ca]:[CO_2] ratio of 1 for each produced water composition is shown in Figure 21.

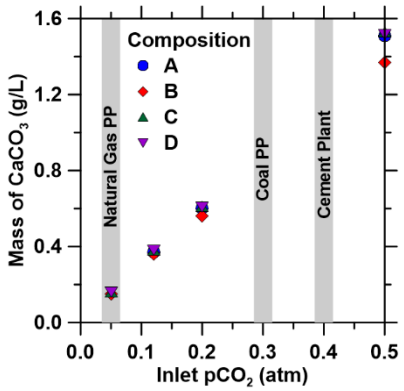

Figure 21. Mass of precipitated $CaCO_3$ per liter of water processed at the optimal volume ratio (where initial [Ca]:[CO_2] ratio is 1:1) as a function of increasing inlet partial pressures of CO_2 in equilibrium with the inlet solution for the ion exchange process.

These results can be used to predict $CaCO_3$ yields utilizing CO_2 waste streams from different industrial plants (e.g., natural gas power plants, coal power plants, cement plants). Critically, these

data provide guidance for industries that aim to either decrease their waste handling (e.g., remove calcium or CO_2) or maximize calcite production. However, the volume ratio selected (e.g., volume of brine required) affects downstream processes (and thus energy and CO_2 removal). The final concentrations of cations following mineralization will affect CO_2 emissions and energy requirements for the ion exchange process (e.g., divalent cation separation via nanofiltration processes), which are calculated below.

5.2.1. Process simulations quantify energy requirements for CO_2 mineralization

CO_2 mineralization for $CaCO_3$ production in the baseline case is modeled by analogy to water treatment processes. If CO_2 sources other than air are to be utilized, CO_2 equilibration with brine streams can be achieved using aeration tanks.[125] Following equilibration, caustic soda (e.g., consumable additive NaOH, considered for baseline scenario) could be mixed into the CO_2-rich produced water resulting in the precipitation of calcium carbonate. Solids are then separated from solution via sedimentation, and the discharge solids can be discharged into the ocean as seen with brine disposal of typical desalination plants. Composition D is selected for the baseline case because of larger $CaCO_3$ purities achieved in initial thermodynamic simulations. Shown in Figure 22a is the amount of NaOH required to achieve $CaCO_3$ yields similar-to those observed from utilizing ion exchange materials for composition D.

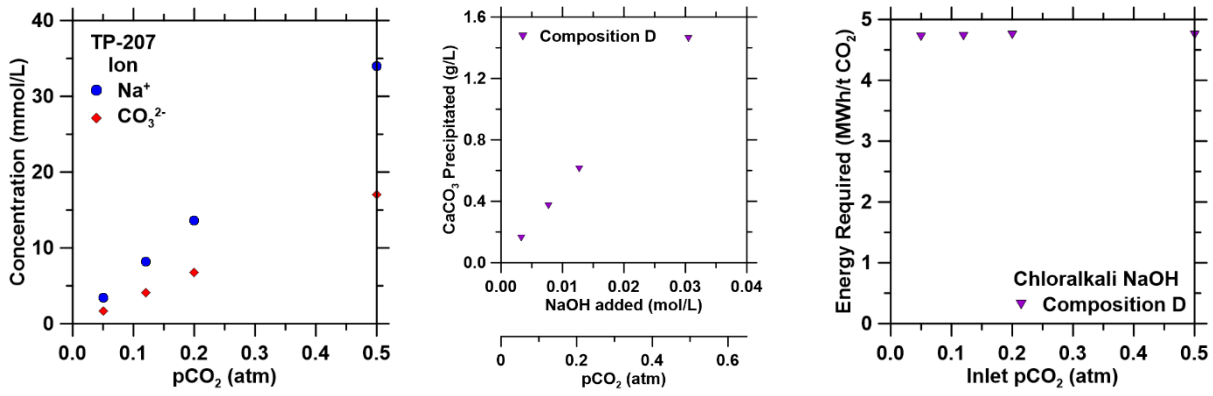

(a) **(b)** **(c)**

Figure 22. (a) ion concentrations present in TP-207 effluent streams following ion exchange as a function of CO_2 partial pressures. **(b)** Mass of precipitated calcium carbonate as a function of NaOH concentration, influenced by the initial CO_2 partial pressure. **(c)** Energy required for CO_2 mineralization using NaOH from chlor-alkali processes at varying CO_2 partial pressures.

The synthesis of NaOH by the conventional chlor-alkali process requires 2.5 MWh/t NaOH.[126] Therefore, the estimated energy demand for $CaCO_3$ precipitation using NaOH as an additive and produced water as the calcium and CO_2 source to be 4.8 MWh/t CO_2 processed, excluding water processing. Utilizing the price of electricity for industrial use estimated at $70 per MWh[127], the cost for CO_2 mineralization is $336/t CO_2 processed for state-of-the-art chlor-alkali-produced NaOH. Thus, ion exchange materials are proposed to induce alkalinity for CO_2 mineralization for $CaCO_3$ production.

Traditional methods for precipitated calcium carbonate production (e.g., calcination of limestone followed by carbonation) have shown to be energy intensive (0.65 MWh/t-CO_2) and as a result

emit CO_2 (0.21 t-CO_2e) because of the large temperature requirements of calcination.[2] To perform a complete simulation analysis of our process, an ASPEN Plus simulation model (Figure 2) was developed using eRNTL as the thermodynamic property method and sequential modular strategy as previously described. Energy requirements for each step of the ion exchange process (e.g., ion exchange, mineralization, nanofiltration and reverse osmosis pumping requirements) were quantified shown in Figure 23.

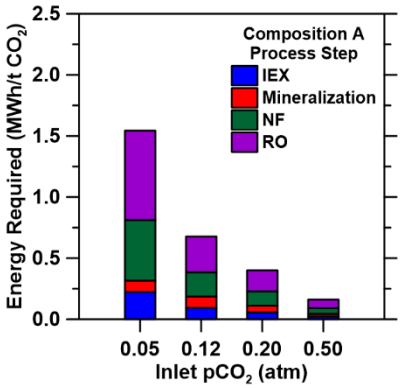

(a)

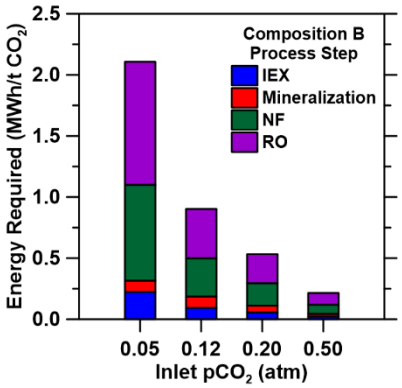

(b)

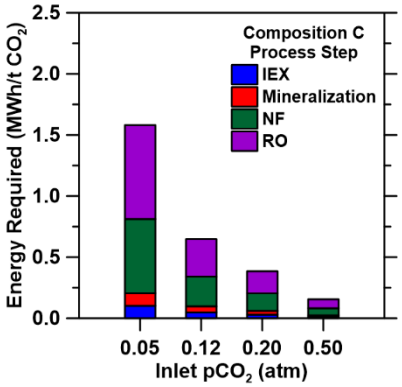

(c)

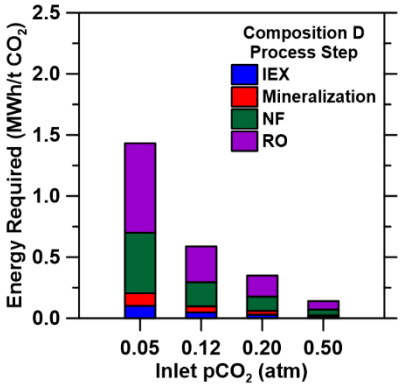

(d)

Figure 23. Energy requirements quantified using the developed ASPEN model for the ion exchange, mineralization, nanofiltration, and reverse osmosis steps of the process, at varying CO_2 concentrations for compositions (**a)** A, **(b)** B, **(c)** C and **(d)** D from Table 4. Inlet flow rates for the ion exchange and produced water streams were adjusted accordingly to match the volume ratio at which $CaCO_3$ was maximized.

As shown in Figure 23a-d, variations in the energy requirement of each step are associated with water pumping and changes in pressure gradients and volume requirements detailed in Table 10 and Table 11.

Table 10. Stream compositions and process parameters for each process step for the industrial scale up of ion exchange for CO_2 mineralization at 25°C and 101 kPa

Process step	**Mass Flow (ton/h)**	**Effluent Stream Composition (mmol/L)**	**Effluent pH**	**Operating Pressure (kPa)**
Bubbling chamber	41 – 81	2 – 34 CO_2 (aq)	4.1 – 4.5	----
Ion-exchange columns	27 - 55	2 – 34 CO_3^{2-}	10 - 11	15
Filtration	53 - 110	50 – 300 Na 1 – 10 Ca 0.5 – 6 Mg < 0.005 Fe	9 - 10.5	80

Nanofiltration[1]	53 - 110	50 – 300 Na	9 - 10.5	120 - 250
Reverse Osmosis[2]	53 - 110	< 1 Na	9 - 10.5	400 - 600
Regeneration	27 - 55	300 – 1000 Na	6 - 7	80

[1]0.95 rejection coefficient used for divalent cations, while 0.1 rejection coefficient was used for monovalent cations; 0.85 pumping efficiency [2]0.99 rejection coefficient used for divalent and monovalent cations; 0.85 pumping efficiency

Table 11. Ion exchange flow rate requirements (m^3/h) at varying CO_2 inlet concentrations per ton of CO_2 processed

Composition	**5% CO_2**	**12% CO_2**	**20% CO_2**	**50% CO_2**
A	260	113	69	27
B	297	116	71	30
C	255	110	66	25
D	250	107	63	22

Energy requirements with respect to the ion exchange and mineralization steps are largely dependent on pumping the volume of water required to mineralize equivalent amounts of $CaCO_3$ (e.g., 1 t-$CaCO_3$) at various inlet CO_2 concentrations, as their pressure requirements are relatively small compared to following steps (Table 10; 15 – 80 kPa). These changes in volume requirements result in approximately 0.08 – 0.20 MWh/t-CO_2 processed required individually for both the ion

exchange and mineralization step. Shown in Table 11, volume requirements per metric ton of CO_2 processed decrease as inlet CO_2 concentration increase because of the larger mass of $CaCO_3$ precipitated at these higher CO_2 concentrations, as discussed in *Section 5.2.1*.

In addition to increases in water requirements, the nanofiltration and reverse osmosis steps are both primarily impacted by the increased pressure gradient required to treat the effluent stream following CO_2 mineralization. Effluent streams following mineralization using the produced water compositions described earlier contain approximately 1 – 10 mmol/L Ca, 1 – 6 mmol/L Mg and 50 – 300 mmol/L Na (Table 10). Complete separation of divalent cations in the stream is required for regeneration of ion exchange materials.[59] Nanofiltration is implemented for the required removal these divalent cations at operating pressures 150 – 350 kPa, which is dependent on the osmotic pressure of the effluent stream following mineralization. Following this treatment, the remaining brine (50 – 300 mmol/L Na) is treated via reverse osmosis for freshwater production and Na concentration. Reverse osmosis operating pressures range from 400 – 600 kPa which are also dependent on the osmotic pressure of the stream to be treated, but capable of treating streams containing ionic strengths 0.5 – 1.0 mol/L.[63,128,129] These larger pressure requirements consequentially result in increased energy requirements as depicted in Figure 18. Nanofiltration energy requirements range from ~0.06 – 0.50 MWh/t-CO_2 processed, whereas reverse osmosis energy requirements range from ~0.08 – 0.81 MWh/t-CO_2 processed. Total energy requirements are additionally comparable to those quantified for alternative $CaCO_3$ precipitation methods (e.g., Ca-extraction from slag leaching ranging from 0.1 – 0.80 MWh/t CO_2).[130–132] Furthermore, the high operating pressures make the nanofiltration and reverse osmosis steps the largest energy contributors to the overall energy requirements of this CO_2 mineralization process. Significantly, total energy requirements using the ion exchange processes and utilizing industrial brines result in

significantly smaller energy requirements as opposed to the addition of NaOH produced from conventional chlor-alkali processes (4.8 MWh/t CO_2). Furthermore, utilizing the price of electricity for industrial use estimated at $70 per MWh[127], the cost for CO_2 mineralization ranges from $25 to $168/t CO_2 processed utilizing ion exchange processes, significantly lower than using consumable base from chlor-alkali processes ($336/t CO_2).

Additionally, energy costs associated with traditional reverse osmosis (e.g., desalination, brine treatment) are primarily affected by the feed conditions (e.g., osmotic pressures, temperatures)[133,134]. Energy requirements associated with these traditional processes range from 3 – 10 kWh per m^3 of water processed. [63,129] For potential integration of this process for brine treatment, energy requirements are quantified for the different produced water compositions and CO_2 partial pressures studied (Figure 24).

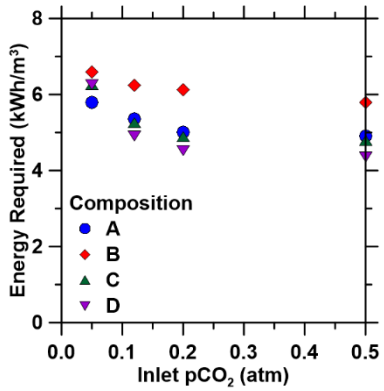

Figure 24. Energy requirements per m^3 of water treated quantified using the developed ASPEN model for the ion exchange process at varying CO_2 concentrations for compositions A, B, C and D from Table 1. Inlet flow rates for the ion exchange and produced water streams were adjusted accordingly to match the volume ratio at which $CaCO_3$ was maximized.

Energy costs for this process range from 4.3 – 6.5 kWh per m^3 of water processed, shown in Figure 22. The lowest energy requirements are observed at larger partial pressures of CO_2, where Ca removal is maximized via the formation of $CaCO_3$. Ca removal results in reduced ionic strengths and osmotic pressures of the streams following mineralization, leading to lower operating pressures for nanofiltration/reverse osmosis treatment. The reduction in feed ionic strength is critical for water treatment as reverse osmosis treatment of high ionic strength solutions is commonly energy intensive and can lead to increased salt permeability in membranes.[129,133,134] Furthermore, removal of Ca prior to reverse osmosis treatment can help mitigate inorganic scaling of compounds (e.g., calcium sulfate, calcium carbonate, calcium phosphate) onto reverse osmosis membranes, which decrease performance.[134] The energy costs associated with this process are within traditional reverse osmosis energy requirements, showing its potential for industrial treatment of various brine streams.

5.2.2. Ion exchange based CO_2 mineralization is a net CO_2 removal technology

As previously discussed, traditional methods for precipitated calcium carbonate production emit 0.21t-CO_2e because of the large temperature requirements during the calcination step of the process.[3] Thus, for industries interested in either maximizing their $CaCO_3$ production or reducing their waste streams, a reduction in emissions compared to their conventional method is critical. Using the combined energy intensities for each step quantified in Figure 18, net CO_2 emissions

can be quantified for the ion exchange process at various CO_2 concentrations. The net CO_2 removal potential for the process is shown in Figure 25 for each composition studied (A, B, C, D).

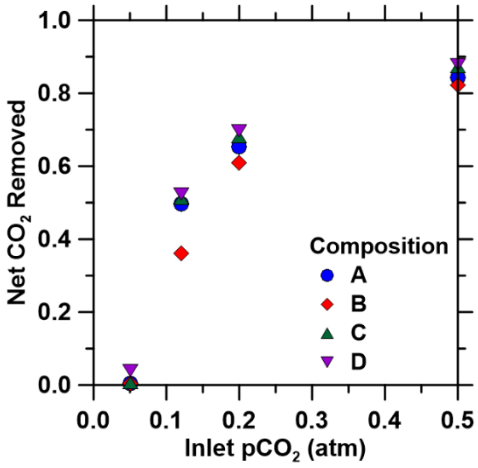

Figure 25. Net CO_2 removal potential (net divided by gross) of the proposed ion exchange process for CO_2 mineralization for each composition studied. Initial calcium concentration for A, B, C and D are: 141, 70.3, 166, and 148 mmol/L respectively.

As shown in Figure 25, the ratio of net CO_2 removal to gross CO_2 removal for the ion exchange process range from 0.05 to 0.90, indicative of a net CO_2 reduction. This ratio increases as the inlet pCO_2 increases because of the larger extent of CO_2 sequestration via mineralization (e.g., larger amount of precipitated $CaCO_3$ as discussed in *Section 5.1*). Concurrently, overall energy requirements (and CO_2 emissions) are reduced because of reductions in the volumes of water required during processing. As previously stated, CO_2 emissions associated with the ion-exchange process are solely dependent on energy requirements associated from pumping of water as opposed to heat requirements for traditional processes. This process is overall carbon-negative across most CO_2 concentrations and produced water compositions studied. Crucially, industries interested in

this process will primarily have to identify their appropriate volume ratio (i.e., volume of brine required for their target CO_2 utilization) after quantifying their initial [Ca]:[CO_2] ratios to examine how downstream processes will affect their respective energy intensities.

Our results indicate that ion exchange processes can be used as an alternative to the addition of stoichiometric inorganic bases (e.g., sodium hydroxide) to induce alkalinity for the consequent precipitation of $CaCO_3$. Various produced water compositions were identified to study the effect of composition on $CaCO_3$ mineralization using 5 – 50 vol% CO_2 concentrations (similar-to that of flue gas concentrations). Mass of precipitated $CaCO_3$ were maximized when [Ca]:[CO_2] ratios were equivalent to 1, and significantly decreased at ratios larger than 1 (where CO_2 was the limiting reagent) and less than 1 (where Ca was the limiting reagent). The mass of precipitated $CaCO_3$ increased with increases in CO_2 concentrations (0.16 – 1.55 g/L), reducing overall volume requirements of the process. Reductions in yields were associated with the formation of contamination phases (e.g., phase contamination from siderite precipitation) consequentially resulted in an increase in energy requirement and costs for the ion exchange process. Nanofiltration and reverse osmosis steps were the largest energy contributors of the ion exchange process (0.07 – 0.80 MWh/t-CO_2 processed). However, the ratio of net CO_2 removal to gross CO_2 removal for the ion exchange process range from 0.05 to 0.90, representing a net CO_2 reduction. Energy requirements and estimated cost for CO_2 mineralization were significantly lower than the studied base case, ranging from $25 – 168 per t CO_2 mineralized. The high calcium carbonate yields, purities (up to 99.8% $CaCO_3$), and low energy requirements obtained from the simulations performed show successful operation at standard temperature and pressure conditions support their potential for industrial implementation.

Chapter 6 Pilot plant demonstration and life cycle assessment of ion exchange processes for CO_2 mineralization using industrial waste streams

6.1. Introduction

In previous studies, we have demonstrated a regenerable pH swing process (Figure 16)[96,97] that relies on ion exchange. This method can shift the pH of CO_2-containing aqueous streams from an initial pH 4 to pH > 10, without the need for caustic soda addition. In this ion exchange process, CO_2 from flue gas (pCO_2 = 0.03 – 0.20 atm or pH 4.1 – 4.34) is equilibrated with water to produce an aqueous stream saturated with dissolved inorganic carbon species, as described in equation 2 – 4, where dissolved inorganic carbon concentrations are dictated by Henry's Law and the thermodynamics of CO_2 speciation in water.[98] Using weakly acidic cation exchange resin TP-207 (R-1 identifier; Na-form with iminodiacetic acid functional groups), H^+ is removed from the solution while Na^+ is released into solution forming aqueous sodium bicarbonate streams in accordance with Equations 2-5, shifting the equilibrium pH from an initial pH 3.9 to a final pH 11.1, resulting in favorable conditions for carbonate precipitation without the addition of caustic soda. The ion exchange solid can be regenerated using Na-rich brines (e.g., produced water containing 0.05 - 3.0 M Na^+)[102] following depletion of divalent cations that can inhibit Na-exchange capacities due to competitive behaviors.[96,99] The proposed process design is shown in Figure 26 where: (1) acidity is introduced via CO_2 bubbling in deionized water; (2) H^+ - Na^+ exchange using fixed-bed reactors containing ion exchange solids to produce a carbonate-rich effluent stream; (3) carbonate precipitation is induced by mixing with produced water or a Ca^{2+}/Mg^{2+}-rich brine; (4) precipitated solids are separated and the remaining effluent is treated via nanofiltration and reverse osmosis for the simultaneous removal of divalent cations and

production of a fresh water (e.g., divalent cation concentrations less than 0.001 M) and Na-rich (e.g., concentrations greater than 0.1 M) regeneration stream to be cycled within the process.[96,97]

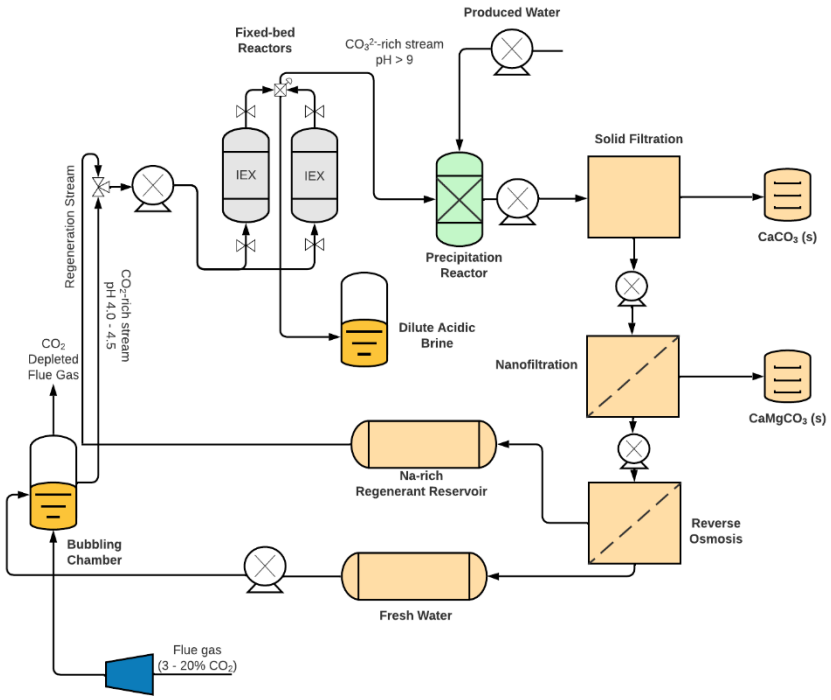

Figure 26. Process flow diagram for CO_2 mineralization via regenerable ion exchange processes.

Previous bench-scale experiments and process simulations generated high purity (>97 wt.%) $CaCO_3$ at yields that utilize 3.5 m^3/h of brine from a total bed volume of 0.05 m^3 of regenerable ion exchange material (equivalent to 1 t-CO_2 captured per day).[96,97] In this work, the ion exchange process is scaled up and developed to process 300 L of brine per day to sequester 100 – 500 g CO_2 per day at pCO_2 = 0.03 – 0.20 atm. To better understand how this process operates using real-world brines of variable chemistries, two produced water sources from the United States are tested:

the Niobrara mixed-shale and chalk play in the Denver-Julesburg Basin and the Utica-Point Pleasant mixed shale and limestone play in the Appalachian Basin. A life cycle assessment (LCA) methodology is employed to analyze the life cycle or net carbon emissions of the technology. From the results, we identify conditions that ensure a net-CO_2 negative process.

6.2. Fixed-bed ion exchange experiments for dynamic H^+ titration capacities

Flow rate is a key parameter to evaluate the efficiency of ion exchange materials in a continuous process because contact time and column hydrodynamics (e.g., Reynolds number) can impact ion exchange capacities[106–109]. Flow rate studies were conducted on a pilot plant to determine H^+ titration capacities using a 2 L bed volume and organic cation exchange resin TP-207 (R-1) at fixed inlet partial pressures of CO_2. The effect of inlet flow rates (0.5 L min^{-1}, 1.0 L min^{-1} and 2.0 L min^{-1}; Re 16.4, 32.8, 65.6 respectively) and inlet CO_2 concentrations at fixed flow rate on H^+ saturation capacity were found using CO_2 concentrations similar-to flue gas (e.g., pCO_2 = 0.03 – 0.20 atm) , shown in Figure 27.

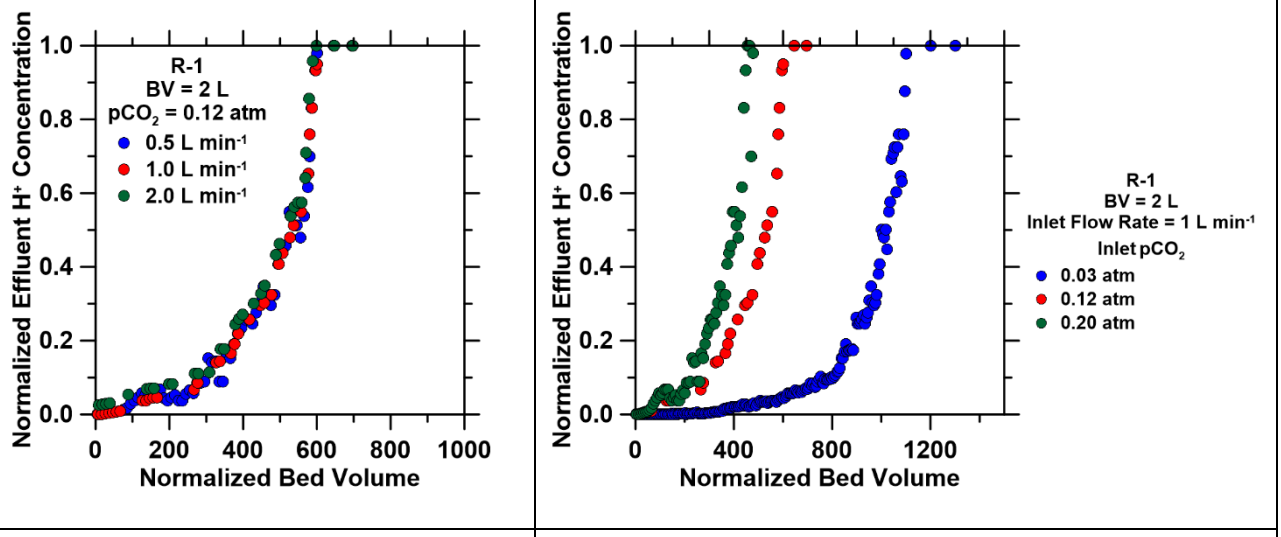

(a) **(b)**

Figure 27. Breakthrough curves for the H^+ exchange reactions for **(a)** inlet pCO_2 = 0.12 atm at varying inlet flow rates and **(b)** inlet pCO_2 = 0.03 – 0.12 atm at fixed flow rate 1 L min^{-1} as a function of normalized bed volume.

H^+ titration capacities (quantified when the outlet H^+ concentration was equivalent to 95% of the inlet H^+ concentration) of the ion exchange resin were unaffected by changes to inlet flow rates (e.g., no change in breakthrough curve shown in Figure 27a at different flow rates), resulting in 0.65 mmol H^+ per g ion exchange solid and in range of H^+ uptake capacities measured at the bench scale (e.g., 0.60 – 0.90 mmol H^+ per g ion exchange solid[96]). Furthermore, H^+ uptake capacities were quantified at varying inlet pCO_2 (Figure 27b) to similarly confirm previous bench-scale performance at higher inlet flow rates and scale.

In accordance with Figure 27b, H^+ titration capacities increase with higher initial CO_2 concentrations: 0.10 mmol H^+ per g, 0.65 mmol H^+ per g, and 0.91 mmol H^+ per g resin for pCO_2

= 0.03 atm, 0.12 atm and 0.20 atm, respectively. H^+ titration capacities increase with higher initial CO_2 concentrations, ranging from 0.10 to 0.91 mmol H^+ per g ion exchange resin. The driving force for ion exchange is the concentration difference between the solute on the sorbent and the solute in solution[96,99,135], resulting in shorter breakthrough times (e.g., rapid filling of binding sites with H^+ in solution) and larger capacities for larger inlet CO_2 concentrations. Increased pCO_2 levels in the inlet stream result in increased H^+ concentrations as described in equation 2, resulting in increased titration capacities. Significantly, measured titration capacities across varying inlet CO_2 concentrations are consistent with those previously measured at the bench-scale[96], indicating successful scale-up and performance of the ion exchange resin.

6.2.1. Fixed-bed ion exchange experiments for CO_2 mineralization

To determine the feasibility of ion exchange solids for regenerative use in a continuous process, experiments were performed over a 24-hour period to treat 300 L of produced water via the precipitation of $CaCO_3$ solids. Deionized water was equilibrated with CO_2, 0.12 atm (pH 4.36), and subsequently fed to the fixed-bed reactor with an inlet flow rate of 1 L min^{-1}. The reactor operates until the effluent pH reaches pH 9.5 to achieve alkaline conditions needed for $CaCO_3$ precipitation. The carbonate-rich effluent is then contacted with the Utica produced water streams for $CaCO_3$ precipitation. The pH swing process is shown across 9 cycles in Figure 28a. An initial pH of 4.36 increases to a maximum of pH 11.8 after in contact with the ion exchange resin. Following breakthrough based on the effluent pH, cycling of the ion exchange solid was performed via regeneration of the ion exchange resin using pH 9, 10, 11, and 12 (e.g., effluent pH following

$CaCO_3$ precipitation[96,97]), shown in Figures 28b for 9 cycles (amount required to utilize the desired volume of produced water).

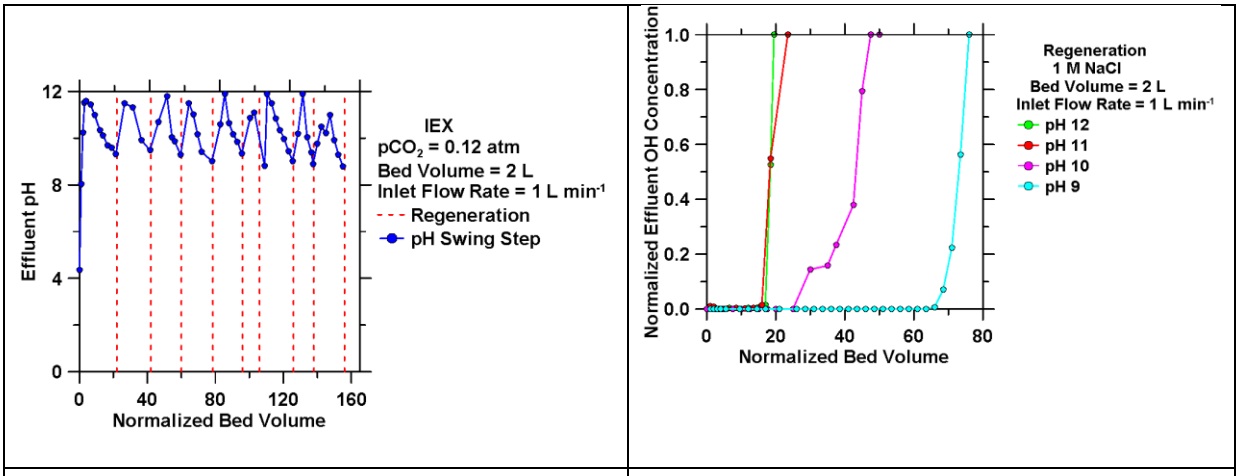

(a) **(b)**

Figure 28. (a) effluent pH as a function of normalized bed volume for cycling of the ion exchange solid at 1.0 $Lmin^{-1}$and an inlet pCO_2 = 0.12 atm and **(b)** normalized effluent hydroxide concentration as a function of normalized bed volume at inlet pH 9, 10, 11 and 12 using background 0.5 M NaCl.

The breakthrough time and regeneration of the ion exchange resin was consistent across multiple cycles at the same flow rates and initial CO_2 feed. This is expected, the residence time between the carbonate rich feed solution and the ion exchange resin was consistent across multiple cycles. The proton removal performance of the resin did not diminish over time as a maximum pH > 10 was achieved within each cycle following regeneration. As previously discussed in Lee and Lee

2016, resin capacities as a function of pH can change[136] (e.g., regeneration pH larger than the pKa of the ion exchange functional group to deprotonate ion exchange sites). Regenerating at different pH confirms the relationship between high alkaline pH and regeneration time, as the pH following mineralization can vary due to the concentration of ions in solution. The normalized bed volume required for regeneration increases with decreasing hydroxide concentrations (decreases in regeneration pH) as seen in Figure 28b. More alkaline solutions result in faster regeneration times due to the larger concentration gradient in hydroxide ions that remove protons from the ion exchange resin. These results are significant as larger regeneration time requirements would result in increased energy intensities associated with pumping energies.

6.2.2. CO_2 mineralization using produced water streams

To quantify the volume requirement (e.g., volume of carbonate-rich stream to produced water stream) needed to maximize $CaCO_3$ precipitation (and CO_2 sequestration) in the process, thermodynamic simulations were performed using varying volume ratios and CO_2 concentrations for Utica and Niobrara produced water samples, shown in Figure 29**.**

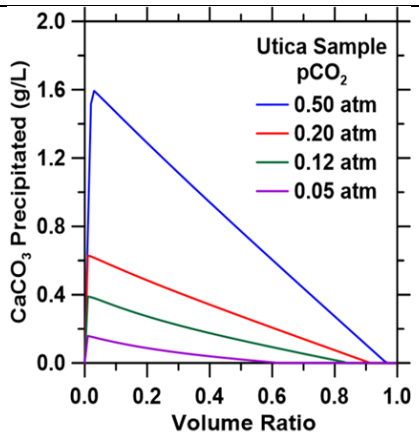

(a)

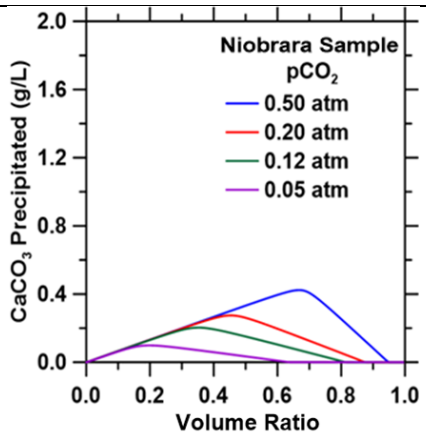

(b)

Figure 29. Calcium carbonate precipitation as a function of volume ratio (ratio of produced water to total water utilized) for **(a)** Utica and **(b)** Niobrara produced water streams.

As shown in Figure 29, there are significant differences in maximum precipitated $CaCO_3$ yields between the two produced water streams. This is a result of the larger differences between initial Ca concentrations in these two sources (Table 5). Calcium carbonate yields increase with larger CO_2 concentrations for both produced water streams, ranging from 0.18 – 1.6 g $CaCO_3$ per L of total solution for Utica produced water and 0.16 – 0.40 g $CaCO_3$ per L of total solution for the Niobrara sample. As previously discussed, $CaCO_3$ yield changes with changing volume ratios and is maximized when the [Ca]:[CO_2] ratios in solution are 1:1[96,97]. Different volume ratios of produced water have different concentrations of calcium, changing how much $CaCO_3$ can be precipitated from the system. Lower volumes of produced water used would require the system to generate more ion exchange effluent to reach the same volume target of 1 L, increasing the energy intensity of the system. To study the viability of ion exchange resin using higher volumes of

solution, pilot plant studies using the alkaline effluent generated from the ion exchange reactor were conducted to treat Utica produced water, shown in Figure 30.

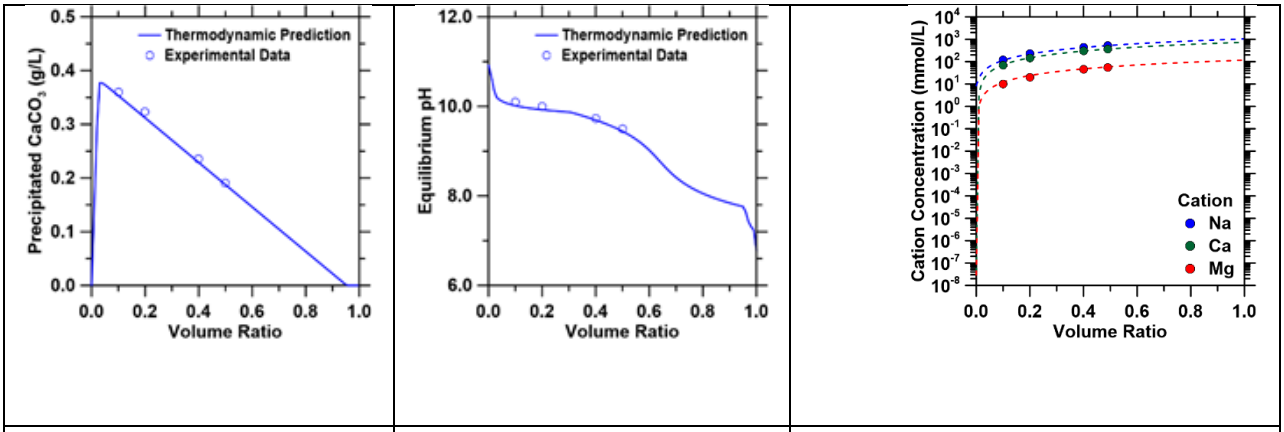

(a) **(b)** **(c)**

Figure 30. (a) Thermodynamic simulations and experimental data displaying precipitated $CaCO_3$ yields as a function of volume ratio (produced water to the total volume of solution) at pCO_2 = 0.12 atm using the Utica produced water composition described above. **(b)** Thermodynamic simulations and experimental data displaying pH as a function of volume ratio (produced water to the total volume of solution) at pCO_2 = 0.12 atm using the Utica produced water composition and **(c)** cation concentration of Na, Ca, and Mg as a function of volume ratio following mineralization.

Predicted and experimental yields for $CaCO_3$ precipitation as a function of volume ratio are shown in Figure 30a. Precipitated $CaCO_3$ yields are maximized at smaller volume ratios (e.g., larger volumes of carbonate-rich solution) at 0.36 grams of $CaCO_3$ per liter of solution and decreases to 0.21 g $CaCO_3$ per L of solution at a 0.5 volume ratio. The experimental mass of precipitated $CaCO_3$, pH and cation concentrations agree with the thermodynamic simulation data, additionally showing these predictions can be applied to different compositions of brines. Furthermore,

validation of pH and cation concentrations (Figure 30b-c) following mineralization is important as these concentrations will affect the process parameters for the treatment of the mineralization effluent to cycle the process (e.g., nanofiltration and reverse osmosis steps for the generation of a Na-rich regeneration stream and a fresh water stream). A regeneration stream at a higher pH will result in faster regeneration times compared to lower pH streams (Figure 28b). Additional separation of residual Ca and Mg ions will affect the energy intensities of the membrane filtration steps (e.g., larger concentrations at higher volume ratios will increase osmotic pressures and in turn operating pressure requirements). The concentration of ions in solution will have an impact on the energy requirement of the nanofiltration step. These energy requirements have previously been quantified for effluent streams containing 50 – 300 mmol/L Na, similar to those measured in this pilot plant, where energy for membrane filtration of this stream results in up to 0.50 MWh/t of CO_2 sequestered to the process[97].

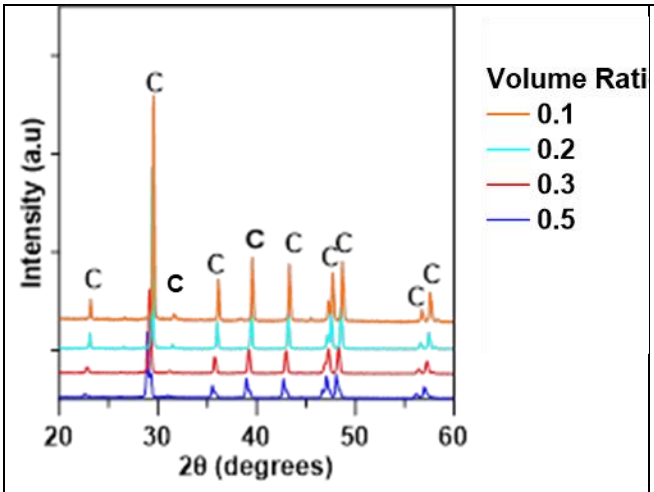

(a)

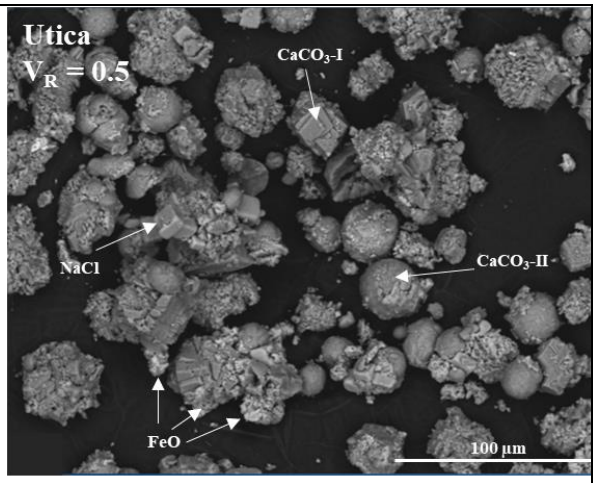

(b)

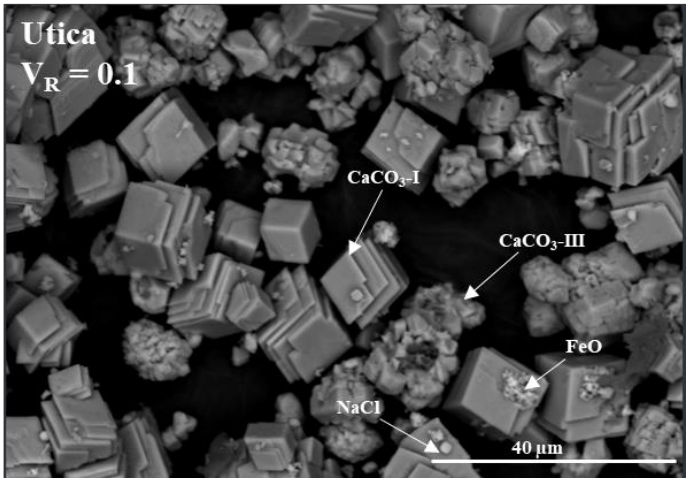

(c)

Figure 31. (a) X-ray diffraction patterns for precipitated $CaCO_3$ solid at volume ratios of 0.1, 0.2, 0.3, and 0.5 Utica produced water to ion exchange solution and SEM images of precipitated solids at volume ratios of **(b)** 0.5 and **(c)** 0.1, with phases identified by EDS. $CaCO_3$ present in variable morphologies for both volume ratios. Rhombohedral shape of $CaCO_3$-I and III suggests they are calcite, spherical shape of $CaCO_3$-II suggest this phase may be vaterite or amorphous calcium carbonate.

Precipitated $CaCO_3$ solids were analyzed for mineralogy and morphologies as shown in Figure 31. X-ray diffraction patterns (Figure 31a) for four solid samples collected from volume ratios 0.1 to 0.5 show calcite (labeled "C") as the primary phase in for each volume ratio. Significant diffraction peak shifts are observed as volume ratio is increased (e.g., increases in volume of produced water used for mineralization). This is likely a result of divalent cation incorporation into the $CaCO_3$ structure (e.g., potential Mg, Sr, Ba, Fe incorporation into calcite structures[137–141]). As shown in Figure 31 b-c, significant changes in calcite morphology are observed with decreasing volume ratios. At a small volume ratio, the conventional rhombohedral structure for calcite is observed

with small amounts of spherical solids (identified as FeO via EDS; Figure 31c).[142] With increasing volume ratios (increasing produced water content), the morphology of $CaCO_3$ crystals changes, with both rhombohedral and spherical morphologies present. The presence of spheroidal $CaCO_3$ suggests that under these conditions at least some of the precipitated $CaCO_3$ may be vaterite or amorphous calcium carbonate.[137,140,143] Previous studies have shown Sr and Ba cation incorporation in calcite through amorphous calcium carbonate or vaterite as a precursor for the formation of crystalline calcium carbonate.[143–145]

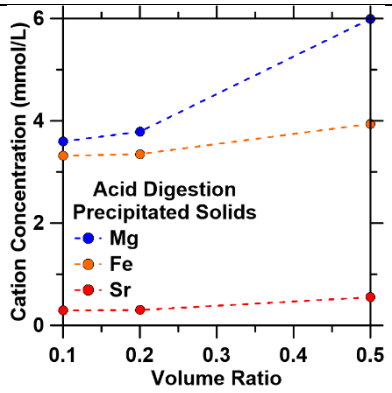

Figure 32. Cation concentrations from acid digestion of precipitated solids at varying volume ratios.

Acid digestion of the precipitated solids at volume ratios 0.1, 0.2 and 0.5 were performed to confirm possible cation incorporation (Figure 32). Shown in Figure 32, as volume ratio increases (increasing produced water content; increasing initial Mg, Sr, and Fe concentrations) the concentrations of Mg, Sr, and Fe dissolved from the solids increase. Increase in Mg and Sr concentrations may indicate cation incorporation in $CaCO_3$ structure from amorphous calcium carbonate precursors at larger volume ratios (e.g., larger initial Mg concentrations can stabilize amorphous calcium carbonate and incorporate Sr into its structure[140,143,144]), whereas increase in

Fe concentrations may be a result of dissolved FeO from the surface of the solids. Produced water discharge streams from Utica and Niobrara Formations can also contain Ra activities ranging approximately 200 – 3600 Bq kg^{-1},[146] which can be incorporated and co-precipitated with sulfate[147] and carbonate minerals.[148] Additional studies are needed to confirm Ra incorporation into precipitated $CaCO_3$ from this ion exchange process.

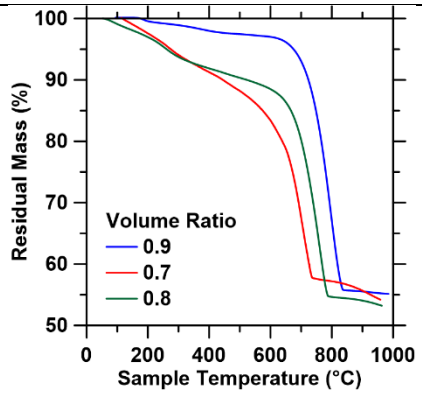

Figure 33. Thermogravimetric analysis of precipitated calcium carbonate solids at varying volume ratios.

Furthermore, thermogravimetric analysis was performed (Figure 33) and confirmed >97% $CaCO_3$ for the precipitate solids, in-which purity was maximized at a 98.9% utilizing a 0.1 volume ratio. These results indicate that volume ratios will be an operational control that can avoid contaminant inclusion in the solid products, incorporated through the formation of amorphous calcium carbonate, when utilizing real-world produced water for industrial use of precipitated $CaCO_3$ (e.g., >70% calcite for permitted addition to Portland cements as a filler[149]). The volume ratio required will be dependent on the composition of brine (Figure 29), where high saline brines will likely require smaller volume ratios to limit contaminant incorporation in the precipitated $CaCO_3$.

The energy requirements of the pilot plant were quantified for different volume ratios of produced water and ion exchange effluent. Intensities were calculated for the pilot operating at a flow rate of 1 L min^{-1} with one hour of mixing. The energy intensities are shown in Figure 34 as a function of volume ratio, normalized by mass of CO_2 sequestered in solid form, calculated using equations 14 – 16.

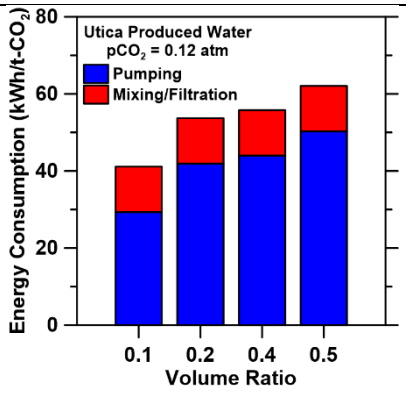

Figure 34. Energy intensity of the ion exchange pilot plant for CO_2 mineralization as a function of volume ratios.

As shown in Figure 34, energy consumption for the pilot plant increases from 40 – 62 kWh per ton CO_2 sequestered as volume ratio increases because of decreased $CaCO_3$ yields resulting in larger volume requirements. Pumping energy requirements contribute to >70% of the energy intensities, ranging from 29.3 – 50.3 kWh per ton CO_2 sequestered whereas filtration and mixing contributes 9.1 – 11.8 kWh per ton CO_2 sequestered. Previous process simulations estimated an energy intensity range of 40 - 95 kWh/t-CO_2 for ion exchange pumping and solid separation steps for various produced water compositions and volume ratios[97], placing these energy intensities in the range of previous predictions and validating previous process simulations. In combination with thermodynamic simulations to predict yields, process simulations can be performed to predict the

energy intensities of the ion exchange steps. Utilizing volume ratios that maximize precipitated $CaCO_3$ (and CO_2 sequestration) is essential to minimizing energy requirements from the alkalization and precipitation steps of the process These energy intensities and measured yields are used to develop a life cycle assessment for the ion exchange process. Further process simulation validation may be needed to validate the energy intensities from the membrane filtration treatment steps.

6.2.3. Life cycle assessment of the ion exchange pilot plant

A life cycle assessment method was performed to quantify net carbon emissions of the ion exchange technology for CO_2 mineralization for various scenarios detailed in Table 6 to produce 1 kg precipitated $CaCO_3$. Table 12 provides the life cycle assessment inputs and databases used to quantify net CO_2 emissions (CO_2e) for the precipitation of $CaCO_3$ via ion exchange processes. The global warming potential for various scenarios and the different steps of the ion exchange process is shown in Figure 35. Mass of CO_2 sequestered and energy intensities from the ion exchange pilot plant were used to as inputs for the various scenarios. To extend the analysis for the entire process, previously quantified nanofiltration and reverse osmosis energy intensities[97] were used and make-up deionized water is added back into the system for complete cycling of the process to produce 1 kg precipitated $CaCO_3$, detailed in Section 2.5.5.

Table 12. Input parameters for lifecycle assessment for the production of 1 kg precipitated calcium carbonate

Item	S1	S2	S3	S4	S5	S6	S7	S8	S9
Input									
CO_2 Removed (kg)	0.44	0.44	0.44	0.44	0.44	0.44	0.44	0.44	0.44
Make-up water (kg)	590	233	161	327	233	233	233	233	233
Total Electricity (kWh)	2.10	0.83	0.57	1.16	0.83	0.83	0.83	0.83	0.83

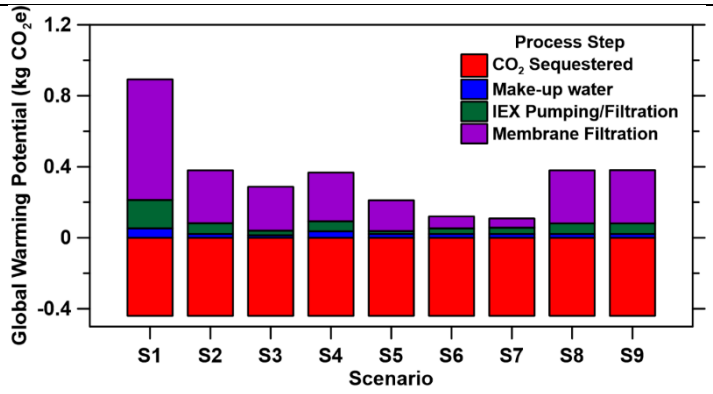

(a)

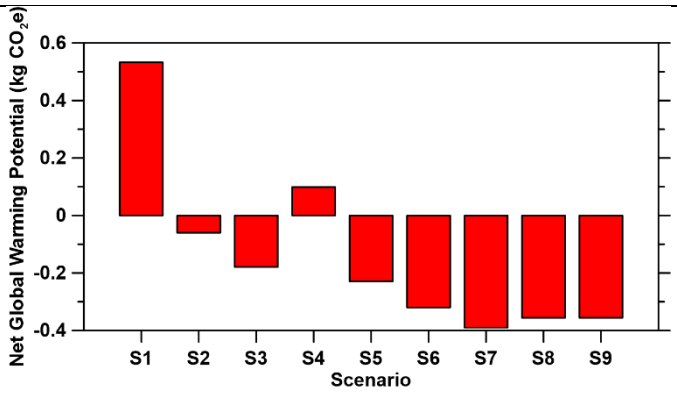

(b)

Figure 35. (a) Global warming potential and **(b)** net global warming potentials to produce 1 kg precipitated calcium carbonate for various scenarios.

Scenarios 1 – 3 detail the global warming potential for the utilization of Utica produced water at pCO_2 = 0.03 atm, 0.12 atm and 0.20 atm, respectively, using the average United States electricity intensity[3]. Increasing inlet concentrations of CO_2 results in water requirement reductions and energy pumping requirements to produce 1 kg precipitated $CaCO_3$. As shown in Figure 10b, Scenario 1 has in the highest net global warming potential at 0.533 kg CO_2e per kg precipitated $CaCO_3$ compared to scenarios 2 and 3 (-0.06 kg and -0.179 kg per kg precipitated $CaCO_3$) due to the larger energy requirements from membrane filtration (1.8 kWh/kg precipitated $CaCO_3$ compared to 0.6 kWh/kg precipitated $CaCO_3$) with ion exchange processing only contributing 0.09 kg CO_2e to total emissions in this scenario. Scenario 4, which utilizes a less saline Niobrara produced water at pCO_2 = 0.12 atm, results in a net positive global warming potential at 0.10 kg CO_2e per kg precipitated $CaCO_3$ because of inherently smaller initial calcium concentrations that result in smaller $CaCO_3$ yields compared to using more concentrated produced water. Despite positive net emissions in scenarios 1 and 4, these emissions are comparable to traditional processes

that produce precipitated $CaCO_3$ (e.g., 0.35 – 1.04 kg CO_2e per kg precipitated $CaCO_3$ produced[69,151]).

A sensitivity analysis was performed to account for the different locations produced water can be sourced and different sources of electricity that can power the process (Table 12; electricity from natural gas, coal, renewables; average electricity grid comparing Eastern and Western United States). Scenarios 5 – 7 show the global warming potentials utilizing Utica produced water and the United States emissions average electricity for using coal, natural gas and renewable sources (e.g., wind turbines)[3,152], respectively, using pCO_2 = 0.12 atm (representative of flue gas). Net global warming potentials are negative for each scenario, minimized by using renewable energy at -0.39 kg CO_2e per kg precipitated $CaCO_3$. Small changes in net emissions are observed when utilizing the average electricity grid from western and eastern United States[2,152] resulting in -0.356 kg CO_2e per kg precipitated $CaCO_3$ produced. Significantly, these results show the impact initial brine compositions and CO_2 concentrations have on the net emissions of the process. Net emissions are significantly reduced using more concentrated streams of brine and CO_2. The overall process would require optimization for less saline brines and CO_2 streams to maximize yields and minimize energy intensities.

Chapter 7 Summary and conclusion

Initial discoveries show that the ion exchange process can be used to induce alkalinity through the system to a degree where precipitation is favored. The results from these studies indicate that ion exchange processes can be used as an alternative to the addition of stoichiometric inorganic bases (e.g., sodium hydroxide) to induce alkalinity for the consequent precipitation of $CaCO_3$. Batch equilibrium isotherms showed larger H^+ uptake capacities for IEX resins compared to zeolites. For all materials in all conditions, H^+ uptake increased with a decrease in divalent cation concentrations in solution. Inhibition of H^+ exchange is likely the result of the larger field strength of divalent cations. Results identified that an inlet stream for the IEX process must be absent of divalent cations in solution. Capacities for zeolites were smaller than those for IEX resins; H^+ uptake may be hindered by the porous structure of zeolites as ion exchange rates are limited by intraparticle diffusion. IEX materials were shown to be regenerable using simulated produced water feeds following mineralization, with varying reaction times required based on regeneration feed pH based on pilot plant experimental data (e.g., higher regeneration pH results in fast regeneration time).

CO_2 mineralization experiments using synthetic produced water compositions followed thermodynamic predictions with regards to phase formations and concentrations of cations in solutions. Experimental calcite yields were 2.3 g/L for cation exchange resins with the formation of goethite (an iron-hydroxide phase, FeOOH) as the primary contaminant phase (99% calcite, 1% goethite). Yields calculated via simulations were 2.6 g/L for the resin, indicating that the experimental process was able to achieve thermodynamic maximum production of calcite. Calcite was the dominant phase for volume ratios 0.2 – 0.6, with goethite as the primary contaminant

phase. These results indicate high purity of calcite formation and volume ratios required to achieve these purities.

Our results indicate that ion exchange processes can be used as an alternative to the addition of stoichiometric inorganic bases (e.g., sodium hydroxide) to induce alkalinity for the consequent precipitation of $CaCO_3$. Various produced water compositions were identified to study the effect of composition on $CaCO_3$ mineralization using 5 – 50 vol% CO_2 concentrations (similar-to that of flue gas concentrations). Mass of precipitated $CaCO_3$ were maximized when [Ca]:[CO_2] ratios were equivalent to 1, and significantly decreased at ratios larger than 1 (where CO_2 was the limiting reagent) and less than 1 (where Ca was the limiting reagent). The mass of precipitated $CaCO_3$ increased with increases in CO_2 concentrations (0.16 – 1.55 g/L), reducing overall volume requirements of the process. Reductions in yields were associated with the formation of contamination phases (e.g., phase contamination from siderite precipitation) consequentially resulted in an increase in energy requirement and costs for the ion exchange process. Nanofiltration and reverse osmosis steps were the largest energy contributors of the ion exchange process (0.07 – 0.80 MWh/t-CO_2 processed). However, the ratio of net CO_2 removal to gross CO_2 removal for the ion exchange process range from 0.05 to 0.90, representing a net CO_2 reduction from process simulations of the ion exchange process. Energy requirements and estimated cost for CO_2 mineralization were significantly lower than the studied base case, ranging from $25 – 168 per t CO_2 mineralized. The high calcium carbonate yields, purities (up to 99.8% $CaCO_3$), and low energy requirements obtained from the simulations performed show successful operation at standard temperature and pressure conditions support their potential for industrial implementation.

Additionally, pilot plant results show the proposed ion exchange process can induce the pH swing required for favorable $CaCO_3$ precipitation without the addition of consumable inorganic base and

can be optimized to treat hypersaline (Na-Ca-Cl-rich) brines, often with considerable amounts of Mg.[60] The Ca and Mg ions found in these brines can be carbonated whereas the Na ions are used for regeneration of spent ion exchange solids. Pilot scale H^+ titration capacities were constant at varying flow rates and at various regeneration conditions. For all cycles, during the regeneration of resin, stronger alkaline solutions (e.g., larger inlet OH^- concentrations) cause faster regeneration times to occur, due to the larger concentration gradient and acidic solutions exhaust the resin faster due to the higher proton concentration in solution. Precipitated solids were measured to be >97% calcite with Mg, Sr, and Fe incorporation, dependent on the volume ratio used. As a result, the ideal produced water for this system would contain a high initial pH, high initial Ca and Mg content, and a low Fe content if possible. For high saline brines, a higher dilution of produced water using ion exchange fluid is required to precipitate a high purity solid for industrial use. The energy intensities associated with operating the pilot at a range of volume ratios was similar, between 40 – 62 kWh/t-CO_2 utilized for pCO_2 = 0.12 atm. The life cycle assessment demonstrates this process to be carbon-negative for partial pressures of CO_2 larger than 0.03 atm and for more concentrated produced water streams (-0.06 to -0.039 kg CO_2e per kg precipitated $CaCO_3$). These studies establish a methodology for the scale up of ion exchange process for CO_2 removal: a suitable ion exchange solid must be identified based on ion exchange capacities and ion exchange rate parameters and a suitable brine must be selected for CO_2 mineralization, in which thermodynamic simulations can be used to accurately predict CO_2 capture yields and $CaCO_3$ morphologies from the process. Future work can focus on the downstream process optimization of mineralization effluents to minimize nanofiltration and reverse osmosis energy intensities, considering these are the most energy intensive steps of the process. With future improvements to

this process (e.g., identifying higher capacity and regenerable ion exchange solids), this ion exchange system can be used as an effective method for CO_2 capture.

References

1. US EPA O. Inventory of U.S. Greenhouse Gas Emissions and Sinks. Published February 8, 2017. Accessed May 24, 2023. https://www.epa.gov/ghgemissions/inventory-us-greenhouse-gas-emissions-and-sinks

2. Global CO2 emissions from energy combustion and industrial processes, 1900-2022 – Charts – Data & Statistics. IEA. Accessed May 24, 2023. https://www.iea.org/data-and-statistics/charts/global-co2-emissions-from-energy-combustion-and-industrial-processes-1900-2022

3. CO2 Emissions in 2022 – Analysis. IEA. Accessed May 24, 2023. https://www.iea.org/reports/co2-emissions-in-2022

4. US EPA O. Sources of Greenhouse Gas Emissions. Published December 29, 2015. Accessed May 24, 2023. https://www.epa.gov/ghgemissions/sources-greenhouse-gas-emissions

5. Veil J. *U.S. Produced Water Volumes and Management Practices in 2017*.; 2020. https://www.gwpc.org/wp-content/uploads/2020/02/pw_report_2017___final.pdf

6. Zemlick K, Kalhor E, Thomson BM, Chermak JM, Sullivan Graham EJ, Tidwell VC. Mapping the energy footprint of produced water management in New Mexico. *Environ Res Lett*. 2018;13(2):024008. doi:10.1088/1748-9326/aa9e54

7. El Hadri N, Quang DV, Goetheer ELV, Abu Zahra MRM. Aqueous amine solution characterization for post-combustion CO2 capture process. *Appl Energy*. 2017;185:1433-1449. doi:10.1016/j.apenergy.2016.03.043

8. Kar S, Goeppert A, Prakash GKS. Integrated CO2 Capture and Conversion to Formate and Methanol: Connecting Two Threads. *Acc Chem Res*. 2019;52(10):2892-2903. doi:10.1021/acs.accounts.9b00324

9. Kim S, Shi H, Lee JY. CO2 absorption mechanism in amine solvents and enhancement of CO2 capture capability in blended amine solvent. *Int J Greenh Gas Control*. 2016;45:181-188. doi:10.1016/j.ijggc.2015.12.024

10. Mores PL, Godoy E, Mussati SF, Scenna NJ. A NGCC power plant with a CO2 post-combustion capture option. Optimal economics for different generation/capture goals. *Chem Eng Res Des*. 2014;92(7):1329-1353. doi:10.1016/j.cherd.2013.11.013

11. Bui M, Gunawan I, Verheyen V, Feron P, Meuleman E, Adeloju S. Dynamic modelling and optimisation of flexible operation in post-combustion CO2 capture plants—A review. *Comput Chem Eng*. 2014;61:245-265. doi:10.1016/j.compchemeng.2013.11.015

12. Cohen SM, Rochelle GT, Webber ME. Optimizing post-combustion CO2 capture in response to volatile electricity prices. *Int J Greenh Gas Control*. 2012;8:180-195. doi:10.1016/j.ijggc.2012.02.011

13. C. Drage T, E. Snape C, A. Stevens L, et al. Materials challenges for the development of solid sorbents for post- combustion carbon capture. *J Mater Chem*. 2012;22(7):2815-2823. doi:10.1039/C2JM12592G

14. Armstrong K, Styring P. Assessing the Potential of Utilization and Storage Strategies for Post-Combustion CO2 Emissions Reduction. *Front Energy Res*. 2015;3. doi:10.3389/fenrg.2015.00008

15. Zhang W, Liu H, Sun Y, Cakstins J, Sun C, Snape CE. Parametric study on the regeneration heat requirement of an amine-based solid adsorbent process for post-combustion carbon capture. *Appl Energy*. 2016;168:394-405. doi:10.1016/j.apenergy.2016.01.049

16. Manzolini G, Sanchez Fernandez E, Rezvani S, Macchi E, Goetheer ELV, Vlugt TJH. Economic assessment of novel amine based CO2 capture technologies integrated in power plants based on European Benchmarking Task Force methodology. *Appl Energy*. 2015;138:546-558. doi:10.1016/j.apenergy.2014.04.066

17. Dutcher B, Fan M, Russell AG. Amine-Based CO2 Capture Technology Development from the Beginning of 2013—A Review. *ACS Appl Mater Interfaces*. 2015;7(4):2137-2148. doi:10.1021/am507465f

18. A Technical, Economic, and Environmental Assessment of Amine-Based CO2 Capture Technology for Power Plant Greenhouse Gas Control | Environmental Science & Technology. Accessed March 27, 2020. https://pubs.acs.org/doi/10.1021/es0158861

19. Liu S, Gao H, He C, Liang Z. Experimental evaluation of highly efficient primary and secondary amines with lower energy by a novel method for post-combustion CO2 capture. *Appl Energy*. 2019;233-234:443-452. doi:10.1016/j.apenergy.2018.10.031

20. Oh SY, Yun S, Kim JK. Process integration and design for maximizing energy efficiency of a coal-fired power plant integrated with amine-based CO2 capture process. *Appl Energy*. 2018;216:311-322. doi:10.1016/j.apenergy.2018.02.100

21. Baseline Studies Overview. netl.doe.gov. Accessed November 4, 2020. https://netl.doe.gov/node/7512

22. Choi S, Drese JH, Eisenberger PM, Jones CW. Application of Amine-Tethered Solid Sorbents for Direct CO2 Capture from the Ambient Air. *Environ Sci Technol*. 2011;45(6):2420-2427. doi:10.1021/es102797w

23. Chaikittisilp W, Kim HJ, Jones CW. Mesoporous Alumina-Supported Amines as Potential Steam-Stable Adsorbents for Capturing CO2 from Simulated Flue Gas and Ambient Air. *Energy Fuels*. 2011;25(11):5528-5537. doi:10.1021/ef201224v

24. Choi S, Gray ML, Jones CW. Amine-Tethered Solid Adsorbents Coupling High Adsorption Capacity and Regenerability for CO2 Capture From Ambient Air. *ChemSusChem*. 2011;4(5):628-635. doi:10.1002/cssc.201000355

25. Seifritz W. CO 2 disposal by means of silicates. *Nature*. 1990;345(6275):486-486. doi:10.1038/345486b0

26. Azdarpour A, Asadullah M, Junin R, Manan M, Hamidi H, Daud ARM. Carbon Dioxide Mineral Carbonation Through pH-swing Process: A Review. *Energy Procedia*. 2014;61:2783-2786. doi:10.1016/j.egypro.2014.12.311

27. Cerozi B da S, Fitzsimmons K. The effect of pH on phosphorus availability and speciation in an aquaponics nutrient solution. *Bioresour Technol*. 2016;219:778-781. doi:10.1016/j.biortech.2016.08.079

28. King DW, Farlow R. Role of carbonate speciation on the oxidation of Fe(II) by H2O2. *Mar Chem*. 2000;70(1):201-209. doi:10.1016/S0304-4203(00)00026-8

29. Dastgheib SA, Knutson C, Yang Y. Produced Water from CO2-EOR in the Illinois Basin. *Energy Procedia*. 2014;63:6878-6886. doi:10.1016/j.egypro.2014.11.722

30. Roach RW, Carr RS, Howard CL, Cain BW. AN ASSESSMENT OF PRODUCED WATER IMPACTS IN THE GALVESTON BAY SYSTEM. :38.

31. Scanlon BR, Reedy RC, Xu P, et al. Can we beneficially reuse produced water from oil and gas extraction in the U.S.? *Sci Total Environ*. 2020;717:137085. doi:10.1016/j.scitotenv.2020.137085

32. Guerra K, Dahm K, Dundorf S. *Oil and Gas Produced Water Management and Beneficial Use in the Western United States*.; 2011.

33. Madalyn Blondes, Engle M, Kharaka Y, et al. ..*S. Geological Survey National Produced Waters Geochemical Database (Ver. 2.3, January 2018): U.S. Geological Survey Data Release*. https://doi.org/10.5066/F7J964W8

34. Chang R, Kim S, Lee S, Choi S, Kim M, Park Y. Calcium Carbonate Precipitation for CO2 Storage and Utilization: A Review of the Carbonate Crystallization and Polymorphism. *Front Energy Res*. 2017;5. doi:10.3389/fenrg.2017.00017

35. Said A, Mattila HP, Järvinen M, Zevenhoven R. Production of precipitated calcium carbonate (PCC) from steelmaking slag for fixation of CO2. *Appl Energy*. 2013;112:765-771. doi:10.1016/j.apenergy.2012.12.042

36. Teir S, Eloneva S, Fogelholm CJ, Zevenhoven R. Dissolution of steelmaking slags in acetic acid for precipitated calcium carbonate production. *Energy*. 2007;32(4):528-539. doi:10.1016/j.energy.2006.06.023

37. Humbert PS, Castro-Gomes J. CO2 activated steel slag-based materials: A review. *J Clean Prod*. 2019;208:448-457. doi:10.1016/j.jclepro.2018.10.058

38. Blast Furnace Slag - Material Description - User Guidelines for Waste and Byproduct Materials in Pavement Construction - FHWA-RD-97-148. Accessed August 4, 2020. https://www.fhwa.dot.gov/publications/research/infrastructure/structures/97148/bfs1.cfm#:~:text=It%20is%20estimated%20that%20approximately,annually%20in%20the%20United%20States.&text=Almost%20all%20of%20the%20blast,of%20this%20slag%20is%20ACBFS

39. Klein AR, Baldwin DS, Singh B, Silvester E. Salinity-induced acidification in a wetland sediment through the displacement of clay-bound iron(II). In: ; 2010. doi:10.1071/EN10057

40. Avena MJ, De Pauli CP. Proton Adsorption and Electrokinetics of an Argentinean Montmorillonite. *J Colloid Interface Sci*. 1998;202(1):195-204. doi:10.1006/jcis.1998.5402

41. Robin V, Tertre E, Beaufort D, Regnault O, Sardini P, Descostes M. Ion exchange reactions of major inorganic cations (H+, Na+, Ca2+, Mg2+ and K+) on beidellite: Experimental results and new thermodynamic database. Toward a better prediction of contaminant mobility in natural environments. *Appl Geochem*. 2015;59:74-84. doi:10.1016/j.apgeochem.2015.03.016

42. *Environmental Impacts of Petroleum Production: Initial Results from the Osage-Skiatook Petroleum Environmental Research Sites, Osage County, Oklahoma*.; 2003. doi:10.3133/wri034260

43. Kulik DA, Wagner T, Dmytrieva SV, et al. GEM-Selektor geochemical modeling package: revised algorithm and GEMS3K numerical kernel for coupled simulation codes. *Comput Geosci*. Published online August 24, 2012. doi:10.1007/s10596-012-9310-6

44. Wagner T, Kulik DA, Hingerl FF, Dmytrieva SV. GEM-SELEKTOR GEOCHEMICAL MODELING PACKAGE: TSolMod LIBRARY AND DATA INTERFACE FOR MULTICOMPONENT PHASE MODELS. *Can Mineral*. 2012;50(5):1173-1195. doi:10.3749/canmin.50.5.1173

45. Seggiani M, Vitolo S, D'Antone S. Recovery of nickel from Orimulsion fly ash by iminodiacetic acid chelating resin. *Hydrometallurgy*. 2006;81(1):9-14. doi:10.1016/j.hydromet.2005.09.005

46. Bhaduri GA, Alamiry MAH, Šiller L. Nickel Nanoparticles for Enhancing Carbon Capture. Journal of Nanomaterials. doi:https://doi.org/10.1155/2015/581785

47. Chowdhury ZZ, Zain SM, Rashid AK, Rafique RF, Khalid K. Breakthrough Curve Analysis for Column Dynamics Sorption of Mn(II) Ions from Wastewater by Using Mangostana garcinia Peel-Based Granular-Activated Carbon. Journal of Chemistry. doi:https://doi.org/10.1155/2013/959761

48. Principles of Adsorption and Adsorption Processes | Wiley. Wiley.com. Accessed August 12, 2020. https://www.wiley.com/en-us/Principles+of+Adsorption+and+Adsorption+Processes-p-9780471866060

49. Hummel W, Berner U, Curti E, Pearson F, Thoenen T. Nagra/PSI Chemical Thermodynamic Data Base 01/01. Published online 2002. doi:10.1524/ract.2002.90.9-11_2002.805

50. Thoenen T, Hummel W, Berner U, Curti E. *The PSI/Nagra Chemical Thermodynamic Database 12/07*. Paul Scherrer Institut; 2007.

51. Lothenbach B, Kulik DA, Matschei T, et al. Cemdata18: A chemical thermodynamic database for hydrated Portland cements and alkali-activated materials. *Cem Concr Res*. 2019;115:472-506. doi:10.1016/j.cemconres.2018.04.018

52. Johnson JW, Oelkers EH, Helgeson HC. SUPCRT92: A software package for calculating the standard molal thermodynamic properties of minerals, gases, aqueous species, and reactions from 1 to 5000 bar and 0 to 1000°C. *Comput Geosci*. 1992;18(7):899-947. doi:10.1016/0098-3004(92)90029-Q

53. Robie R, Hemingway B. *Thermodynamic Properties of Minerals and Related Substances at 298.15 K and 1 Bar (105 Pascals) Pressure and at Higher Temperatures*.; 1995.

54. Galvez-Martos JL, Elhoweris A, Morrison J, Al-horr Y. Conceptual design of a CO2 capture and utilisation process based on calcium and magnesium rich brines. *J CO2 Util*. 2018;27:161-169. doi:10.1016/j.jcou.2018.07.011

55. Di Lorenzo F, Burgos-Cara A, Ruiz-Agudo E, Putnis CV, Prieto M. Effect of ferrous iron on the nucleation and growth of $CaCO_3$ in slightly basic aqueous solutions. *CrystEngComm*. 2017;19(3):447-460. doi:10.1039/C6CE02290A

56. Helgeson HC, Kirkham DH, Flowers GC. Theoretical prediction of the thermodynamic behavior of aqueous electrolytes by high pressures and temperatures; IV, Calculation of activity coefficients, osmotic coefficients, and apparent molal and standard and relative partial molal properties to 600 degrees C and 5kb. *Am J Sci*. 1981;281(10):1249-1516. doi:10.2475/ajs.281.10.1249

57. Oil and Gas Waters Project | U.S. Geological Survey. Accessed December 20, 2021. https://www.usgs.gov/centers/geology%2C-energy-%26amp%3Bamp%3B-minerals-science-center/science/oil-and-gas-waters-project

58. Chen CC, Song Y. Generalized electrolyte-NRTL model for mixed-solvent electrolyte systems. *AIChE J*. 2004;50(8):1928-1941. doi:10.1002/aic.10151

59. Bustillos S, Alturki A, Prentice D, et al. Implementation of Ion Exchange Processes for Carbon Dioxide Mineralization Using Industrial Waste Streams. *Front Energy Res*. 2020;8. doi:10.3389/fenrg.2020.610392

60. Al-Zoubi H, Omar W. Rejection of salt mixtures from high saline by nanofiltration membranes. *Korean J Chem Eng*. 2009;26(3):799-805. doi:10.1007/s11814-009-0133-7

61. Hilal N, Al-Zoubi H, Mohammad AW, Darwish NA. Nanofiltration of highly concentrated salt solutions up to seawater salinity. *Desalination*. 2005;184(1):315-326. doi:10.1016/j.desal.2005.02.062

62. Ahmed M, Shayya WH, Hoey D, Al-Handaly J. Brine disposal from reverse osmosis desalination plants in Oman and the United Arab Emirates. *Desalination*. 2001;133(2):135-147. doi:10.1016/S0011-9164(01)80004-7

63. Dashtpour R, Al-Zubaidy SN. Energy Efficient Reverse Osmosis Desalination Process. *Int J Environ Sci Dev*. 2012;3(4):7.

64. Blondes MS, Shelton JL, Engle MA, et al. Utica Shale Play Oil and Gas Brines: Geochemistry and Factors Influencing Wastewater Management. *Environ Sci Technol*. 2020;54(21):13917-13925. doi:10.1021/acs.est.0c02461

65. Hydraulic Power - an overview | ScienceDirect Topics. Accessed June 12, 2023. https://www.sciencedirect.com/topics/engineering/hydraulic-power

66. Mixing Power - an overview | ScienceDirect Topics. Accessed June 12, 2023. https://www.sciencedirect.com/topics/engineering/mixing-power

67. 14:00-17:00. ISO 14040:2006. ISO. Published August 12, 2014. Accessed June 12, 2023. https://www.iso.org/standard/37456.html

68. 14:00-17:00. ISO 14044:2006. ISO. Published August 12, 2014. Accessed June 12, 2023. https://www.iso.org/standard/38498.html

69. Mattila HP, Hudd H, Zevenhoven R. Cradle-to-gate life cycle assessment of precipitated calcium carbonate production from steel converter slag. *J Clean Prod*. 2014;84:611-618. doi:10.1016/j.jclepro.2014.05.064

70. Batuecas E, Liendo F, Tommasi T, Bensaid S, Deorsola FA, Fino D. Recycling CO2 from flue gas for CaCO3 nanoparticles production as cement filler: A Life Cycle Assessment. *J CO2 Util*. 2021;45:101446. doi:10.1016/j.jcou.2021.101446

71. Alrehaili O, Perreault F, Sinha S, Westerhoff P. Increasing net water recovery of reverse osmosis with membrane distillation using natural thermal differentials between brine and co-located water sources: Impacts at large reclamation facilities. *Water Res*. 2020;184:116134. doi:10.1016/j.watres.2020.116134

72. Boo C, Wang Y, Zucker I, Choo Y, Osuji CO, Elimelech M. High Performance Nanofiltration Membrane for Effective Removal of Perfluoroalkyl Substances at High Water Recovery. *Environ Sci Technol*. 2018;52(13):7279-7288. doi:10.1021/acs.est.8b01040

73. Harland CE. *Ion Exchange*.; 1994. doi:10.1039/9781847551184

74. Nasef M. In Separation and Purification. In: *Polymer Grafting and Crosslinking*. John Wiley & Sons, Ltd; 2008:233-272. doi:10.1002/9780470414811.ch10

75. Flanigen EM, Broach RW, Wilson ST. Introduction. In: *Zeolites in Industrial Separation and Catalysis*. John Wiley & Sons, Ltd; 2010:1-26. doi:10.1002/9783527629565.ch1

76. The concept of “capacity” in zeolite ion-exchange systems. - Abstract - Europe PMC. Accessed April 15, 2020. http://europepmc.org/article/med/15567382

77. Kirov G, Filizova L. Cationic hydration impact on zeolite formation and properties: A review and discussion. :18.

78. Munthali M, Elsheikh M, Johan E, Matsue N. Proton Adsorption Selectivity of Zeolites in Aqueous Media: Effect of Si/Al Ratio of Zeolites. *Molecules*. 2014;19(12):20468-20481. doi:10.3390/molecules191220468

79. Víctor-Ortega MD, Ochando-Pulido JM, Martínez-Ferez A. Impacts of main parameters on the regeneration process efficiency of several ion exchange resins after final purification of olive mill effluent. *Sep Purif Technol*. 2017;173:1-8. doi:10.1016/j.seppur.2016.08.037

80. Maul GA, Kim Y, Amini A, Zhang Q, Boyer TH. Efficiency and life cycle environmental impacts of ion-exchange regeneration using sodium, potassium, chloride, and bicarbonate salts. *Chem Eng J*. 2014;254:198-209. doi:10.1016/j.cej.2014.05.086

81. Leaković S, Mijatović I, Cerjan-Stefanović Š, Hodžić E. Nitrogen removal from fertilizer wastewater by ion exchange. *Water Res*. 2000;34(1):185-190. doi:10.1016/S0043-1354(99)00122-0

82. Kunin R, Vassiliou B. Regeneration of Carboxylic Cation Exchange Resins with Carbon Dioxide. *Ind Eng Chem Prod Res Dev*. 1963;2(1):1-3. doi:10.1021/i360005a001

83. Guo H, Ren Y, Sun X, et al. Removal of Pb2+ from aqueous solutions by a high-efficiency resin. *Appl Surf Sci*. 2013;283:660-667. doi:10.1016/j.apsusc.2013.06.161

84. Druckenmiller ML, Maroto-Valer MM. Carbon sequestration using brine of adjusted pH to form mineral carbonates. *Fuel Process Technol*. 2005;86(14):1599-1614. doi:10.1016/j.fuproc.2005.01.007

85. Dinu MV, Dragan ES. Heavy metals adsorption on some iminodiacetate chelating resins as a function of the adsorption parameters. *React Funct Polym*. 2008;68(9):1346-1354. doi:10.1016/j.reactfunctpolym.2008.06.011

86. Breck D. *Zeolite Molecular Sieves: Structure, Chemistry and Use.* ohn Wiley & Sons Inc.; 1974.

87. Florin NH, Blamey J, Fennell PS. Synthetic CaO-based sorbent for CO2 capture from large-point sources. *Energy Fuels*. 2010;24(8):4598-4604.

88. Chowdhury ZZ, Hamid SBA, Zain SM. Evaluating Design Parameters for Breakthrough Curve Analysis and Kinetics of Fixed Bed Columns for Cu(II) Cations Using Lignocellulosic Wastes. *BioResources*. 2014;10(1):732-749. doi:10.15376/biores.10.1.732-749

89. Bhaumik M, Setshedi K, Maity A, Onyango MS. Chromium(VI) removal from water using fixed bed column of polypyrrole/Fe3O4 nanocomposite. *Sep Purif Technol*. 2013;110:11-19. doi:10.1016/j.seppur.2013.02.037

90. Aksu Z, Gönen F. Biosorption of phenol by immobilized activated sludge in a continuous packed bed: prediction of breakthrough curves. *Process Biochem*. 2004;39(5):599-613. doi:10.1016/S0032-9592(03)00132-8

91. El-Kamash AM. Evaluation of zeolite A for the sorptive removal of Cs+ and Sr2+ ions from aqueous solutions using batch and fixed bed column operations. *J Hazard Mater*. 2008;151(2):432-445. doi:10.1016/j.jhazmat.2007.06.009

92. Nishiyama R, Munemoto T, Fukushi K. Formation condition of monohydrocalcite from CaCl2–MgCl2–Na2CO3 solutions. *Geochim Cosmochim Acta*. 2013;100:217-231. doi:10.1016/j.gca.2012.09.002

93. Blue CR, Giuffre A, Mergelsberg S, Han N, De Yoreo JJ, Dove PM. Chemical and physical controls on the transformation of amorphous calcium carbonate into crystalline CaCO3 polymorphs. *Geochim Cosmochim Acta*. 2017;196:179-196. doi:10.1016/j.gca.2016.09.004

94. Rodriguez-Blanco JD, Shaw S, Bots P, Roncal-Herrero T, Benning LG. The role of Mg in the crystallization of monohydrocalcite. *Geochim Cosmochim Acta*. 2014;127:204-220. doi:10.1016/j.gca.2013.11.034

95. Kralj D, Kontrec J, Brečević L, Falini G, Nöthig-Laslo V. Effect of Inorganic Anions on the Morphology and Structure of Magnesium Calcite. *Chem – Eur J*. 2004;10(7):1647-1656. doi:10.1002/chem.200305313

96. Bustillos S, Alturki A, Prentice D, et al. Implementation of Ion Exchange Processes for Carbon Dioxide Mineralization Using Industrial Waste Streams. *Front Energy Res*. 2020;8. Accessed April 17, 2023. https://www.frontiersin.org/articles/10.3389/fenrg.2020.610392

97. Bustillos S, Prentice D, La Plante EC, Wang B, Sant G, Simonetti D. Process Simulations Reveal the Carbon Dioxide Removal Potential of a Process That Mineralizes Industrial Waste Streams via an Ion Exchange-Based Regenerable pH Swing. *ACS Sustain Chem Eng*. 2022;10(19):6255-6264. doi:10.1021/acssuschemeng.2c00458

98. The hydration of carbon dioxide | Journal of Chemical Education. Accessed May 24, 2023. https://pubs.acs.org/doi/10.1021/ed037p14

99. Robin V, Tertre E, Beaufort D, Regnault O, Sardini P, Descostes M. Ion exchange reactions of major inorganic cations (H+, Na+, Ca2+, Mg2+ and K+) on beidellite: Experimental results and new thermodynamic database. Toward a better prediction of contaminant mobility in natural environments. *Appl Geochem*. 2015;59:74-84. doi:10.1016/j.apgeochem.2015.03.016

100. Avena MJ, De Pauli CP. Proton Adsorption and Electrokinetics of an Argentinean Montmorillonite. *J Colloid Interface Sci*. 1998;202(1):195-204. doi:10.1006/jcis.1998.5402

101. Omerspahic M, Al-Jabri H, Siddiqui SA, Saadaoui I. Characteristics of Desalination Brine and Its Impacts on Marine Chemistry and Health, With Emphasis on the Persian/Arabian Gulf: A Review. *Front Mar Sci*. 2022;9. Accessed October 4, 2023. https://www.frontiersin.org/articles/10.3389/fmars.2022.845113

102. Blondes MS, Gans KD, Engle MA, et al. U.S. Geological Survey National Produced Waters Geochemical Database (ver. 2.3, January 2018). Published online 2018. doi:10.5066/F7J964W8

103. Favergeon L, Morandini J, Pijolat M, Soustelle M. A General Approach for Kinetic Modeling of Solid-Gas Reactions at Reactor Scale: Application to Kaolinite Dehydroxylation. *Oil Gas Sci Technol – Rev D'IFP Energ Nouv*. 2013;68(6):1039-1048. doi:10.2516/ogst/2012018

104. Sadegh-Vaziri R, Babler MU. Numerical investigation of the outward growth of ZnS in the removal of H 2 S in a packed bed of ZnO. *Chem Eng Sci*. 2017;158:328-339. doi:10.1016/j.ces.2016.10.038

105. Kantorovich II, Bar-Ziv E. Processes in highly porous chars under kinetically controlled conditions: I. Evolution of the porous structure. *Combust Flame*. 1994;97(1):61-78. doi:10.1016/0010-2180(94)90116-3

106. Nauman EB. Residence Time Theory. *Ind Eng Chem Res*. 2008;47(10):3752-3766. doi:10.1021/ie071635a

107. Borba CE, Guirardello R, Silva EA, Veit MT, Tavares CRG. Removal of nickel(II) ions from aqueous solution by biosorption in a fixed bed column: Experimental and theoretical breakthrough curves. *Biochem Eng J*. 2006;30(2):184-191. doi:10.1016/j.bej.2006.04.001

108. Chatterjee S, Mondal S, De S. Design and scaling up of fixed bed adsorption columns for lead removal by treated laterite. *J Clean Prod*. 2018;177:760-774. doi:10.1016/j.jclepro.2017.12.249

109. Barros MASD, Silva EA, Arroyo PA, et al. Removal of Cr(III) in the fixed bed column and batch reactors using as adsorbent zeolite NaX. *Chem Eng Sci*. 2004;59(24):5959-5966. doi:10.1016/j.ces.2004.07.040

110. Aksu Z, Gönen F. Biosorption of phenol by immobilized activated sludge in a continuous packed bed: prediction of breakthrough curves. *Process Biochem*. 2004;39(5):599-613. doi:10.1016/S0032-9592(03)00132-8

111. Ostroski IC, Borba CE, Silva EA, Arroyo PA, Guirardello R, Barros MASD. Mass Transfer Mechanism of Ion Exchange in Fixed Bed Columns. *J Chem Eng Data*. 2011;56(3):375-382. doi:10.1021/je100568n

112. Bhaumik M, Setshedi K, Maity A, Onyango MS. Chromium(VI) removal from water using fixed bed column of polypyrrole/Fe3O4 nanocomposite. *Sep Purif Technol*. 2013;110:11-19. doi:10.1016/j.seppur.2013.02.037

113. Puerta-Falla G, Balonis M, Falzone G, Bauchy M, Neithalath N, Sant G. Monovalent Ion Exchange Kinetics of Hydrated Calcium-Alumino Layered Double Hydroxides. *Ind Eng Chem Res*. 2017;56(1):63-74. doi:10.1021/acs.iecr.6b03474

114. Gouran-Orimi R, Mirzayi B, Nematollahzadeh A, Tardast A. Competitive adsorption of nitrate in fixed-bed column packed with bio-inspired polydopamine coated zeolite. *J Environ Chem Eng*. 2018;6(2):2232-2240. doi:10.1016/j.jece.2018.01.049

115. Dyer A, Gettins RB. The mobility of cations in synthetic zeolites with the faujasite framework — III: Self-diffusion of cations into X and Y zeolites from non-aqueous solutions. *J Inorg Nucl Chem*. 1970;32(7):2401-2410. doi:10.1016/0022-1902(70)80523-1

116. Townsend RP. Chapter 10 Ion Exchange in Zeolites. In: van Bekkum H, Flanigen EM, Jansen JC, eds. *Studies in Surface Science and Catalysis*. Vol 58. Introduction to Zeolite Science and Practice. Elsevier; 1991:359-390. doi:10.1016/S0167-2991(08)63608-3

117. Azzam S, Simonetti DA. Linear Driving Force Approximations as Predictive Models for Reactive Sorption. *Energy Technol*. 2020;8(8):1900718. doi:10.1002/ente.201900718

118. US EPA O. Sources of Greenhouse Gas Emissions. Published December 29, 2015. Accessed December 14, 2021. https://www.epa.gov/ghgemissions/sources-greenhouse-gas-emissions

119. International Desalination Association and Global Water Intelligence Release New Data in 30th Worldwide Desalting Inventory. Idadesal. Published October 9, 2017. Accessed December 14, 2021. https://idadesal.org/international-desalination-association-and-global-water-intelligence-release-new-data-in-30th-worldwide-desalting-inventory/

120. Millero FJ, Feistel R, Wright DG, McDougall TJ. The composition of Standard Seawater and the definition of the Reference-Composition Salinity Scale. *Deep Sea Res Part Oceanogr Res Pap*. 2008;55(1):50-72. doi:10.1016/j.dsr.2007.10.001

121. Bang JH, Chae SC, Lee SW, et al. Sequential carbonate mineralization of desalination brine for CO2 emission reduction. *J CO2 Util*. 2019;33:427-433. doi:10.1016/j.jcou.2019.07.020

122. Cornejo PK, Santana MVE, Hokanson DR, Mihelcic JR, Zhang Q. Carbon footprint of water reuse and desalination: a review of greenhouse gas emissions and estimation tools. *J Water Reuse Desalination*. 2014;4(4):238-252. doi:10.2166/wrd.2014.058

123. Seifritz W. CO2 disposal by means of silicates. *Nature*. 1990;345(6275):486-486. doi:10.1038/345486b0

124. Kern DM. The hydration of carbon dioxide. *J Chem Educ*. 1960;37(1):14. doi:10.1021/ed037p14

125. La Plante EC, Simonetti DA, Wang J, et al. Saline Water-Based Mineralization Pathway for Gigatonne-Scale CO_2 Management. *ACS Sustain Chem Eng*. 2021;9(3):1073-1089. doi:10.1021/acssuschemeng.0c08561

126. Thiel GP, Kumar A, Gómez-González A, John H. Lienhard V. Utilization of Desalination Brine for Sodium Hydroxide Production: Technologies, Engineering Principles, Recovery Limits, and Future Directions. ACS Publications. doi:10.1021/acssuschemeng.7b02276

127. Prices and factors affecting prices - U.S. Energy Information Administration (EIA). Accessed March 14, 2022. https://www.eia.gov/energyexplained/electricity/prices-and-factors-affecting-prices.php

128. Bartels C, Franks R, Rybar S, Schierach M, Wilf M. The effect of feed ionic strength on salt passage through reverse osmosis membranes. *Desalination*. 2005;184(1-3):185-195. doi:10.1016/j.desal.2005.04.032

129. Davenport DM, Deshmukh A, Werber JR, Elimelech M. High-Pressure Reverse Osmosis for Energy-Efficient Hypersaline Brine Desalination: Current Status, Design Considerations, and Research Needs. *Environ Sci Technol Lett*. 2018;5(8):467-475. doi:10.1021/acs.estlett.8b00274

130. Eloneva S, Said A, Fogelholm CJ, Zevenhoven R. Feasibility Study of a Method Utilizing Carbon Dioxide and Steelmaking Slags to Produce Precipitated Calcium Carbonate (PCC). Published online 2010:11.

131. Mattila HP, Hudd H, Zevenhoven R. Cradle-to-gate life cycle assessment of precipitated calcium carbonate production from steel converter slag. *J Clean Prod*. 2014;84:611-618. doi:10.1016/j.jclepro.2014.05.064

132. Eloneva S, Teir S, Salminen J, Fogelholm CJ, Zevenhoven R. Steel Converter Slag as a Raw Material for Precipitation of Pure Calcium Carbonate. *Ind Eng Chem Res*. 2008;47(18):7104-7111. doi:10.1021/ie8004034

133. Riedinger AB, Hickman CE. Considerations of energy consumption in desalination by reverse osmosis. *Desalination*. 1982;40(3):259-270. doi:10.1016/S0011-9164(00)88694-4

134. Reverse osmosis desalination_ A state-of-the-art review | Elsevier Enhanced Reader. doi:10.1016/j.desal.2019.02.008

135. Kang SY, Lee JU, Moon SH, Kim KW. Competitive adsorption characteristics of Co2+, Ni2+, and Cr3+ by IRN-77 cation exchange resin in synthesized wastewater. *Chemosphere*. 2004;56(2):141-147. doi:10.1016/j.chemosphere.2004.02.004

136. Lee SK, Lee UH. Adsorption and desorption property of iminodiacetate resin (Lewatit® TP207) for indium recovery. *J Ind Eng Chem*. 2016;40:23-25. doi:10.1016/j.jiec.2016.05.016

137. Mucci A, Morse JW. The incorporation of Mg2+ and Sr2+ into calcite overgrowths: influences of growth rate and solution composition. *Geochim Cosmochim Acta*. 1983;47(2):217-233. doi:10.1016/0016-7037(83)90135-7

138. Dromgoole EL, Walter LM. Iron and manganese incorporation into calcite: Effects of growth kinetics, temperature and solution chemistry. *Chem Geol*. 1990;81(4):311-336. doi:10.1016/0009-2541(90)90053-A

139. Enhanced Crystallographic Incorporation of Strontium(II) Ions into Calcite via Preferential Adsorption at Obtuse Growth Steps | Crystal Growth & Design. Accessed June 12, 2023. https://pubs.acs.org/doi/10.1021/acs.cgd.7b01614

140. Xto JM, Du H, Borca CN, Amstad E, van Bokhoven JA, Huthwelker T. Tuning the Incorporation of Magnesium into Calcite during Its Crystallization from Additive-Free Aqueous Solution. *Cryst Growth Des*. 2019;19(8):4385-4394. doi:10.1021/acs.cgd.9b00179

141. (PDF) Incorporation of Incompatible Strontium and Barium Ions into Calcite (CaCO3) through Amorphous Calcium Carbonate. Accessed June 28, 2023. https://www.researchgate.net/publication/340000866_Incorporation_of_Incompatible_Strontium_and_Barium_Ions_into_Calcite_CaCO3_through_Amorphous_Calcium_Carbonate

142. Xiao-Fei Q, Yao QZ, Zhou GT. Synthesis of siderite microspheres and their transformation to magnetite microspheres. *Eur J Mineral*. 2011;23:757-770. doi:10.1127/0935-1221/2011/0023-2134

143. Littlewood JL, Shaw S, Peacock CL, Bots P, Trivedi D, Burke IT. Mechanism of Enhanced Strontium Uptake into Calcite via an Amorphous Calcium Carbonate Crystallization Pathway. *Cryst Growth Des*. 2017;17(3):1214-1223. doi:10.1021/acs.cgd.6b01599

144. Saito A, Kagi H, Marugata S, et al. Incorporation of Incompatible Strontium and Barium Ions into Calcite (CaCO3) through Amorphous Calcium Carbonate. *Minerals*. 2020;10(3):270. doi:10.3390/min10030270

145. Breevi L, Kralj D. On Calcium Carbonates: from Fundamental Research to Application. *Croat Chem Acta*. Published online 2007.

146. McDevitt B, McLaughlin M, Cravotta CA, et al. Emerging investigator series: radium accumulation in carbonate river sediments at oil and gas produced water discharges: implications for beneficial use as disposal management. *Environ Sci Process Impacts*. 2019;21(2):324-338. doi:10.1039/C8EM00336J

147. Lestini L, Beaucaire C, Vercouter T, Ballini M, Descostes M. Role of Trace Elements in the 226-Radium Incorporation in Sulfate Minerals (Gypsum and Celestite). *ACS Earth Space Chem*. 2019;3(2):295-304. doi:10.1021/acsearthspacechem.8b00150

148. Agency IAE. *The Environmental Behaviour of Radium: Revised Edition*. International Atomic Energy Agency; 2014:1-267. Accessed June 29, 2023. https://www.iaea.org/publications/10478/the-environmental-behaviour-of-radium-revised-edition

149. Matschei T, Lothenbach B, Glasser FP. The role of calcium carbonate in cement hydration. *Cem Concr Res*. 2007;37(4):551-558. doi:10.1016/j.cemconres.2006.10.013

150. Energy Analysis. netl.doe.gov. Accessed June 14, 2022. https://netl.doe.gov/energy-analysis/details

151. Stork M, Meindertsma W, Overgaag M, Neelis M. *A Competitive and Efficient Lime Industry*.; 2014.

152. U.S. energy facts explained - consumption and production - U.S. Energy Information Administration (EIA). Accessed June 14, 2023. https://www.eia.gov/energyexplained/us-energy-facts/